Asymmetric propagation of surface spin waves in Co/Pt multilayers

Rutten, Luuk

Award date:
2017

Asymmetric propagation of surface spin waves in Co/Pt multilayers

L. Rutten

Master thesis

May, 2017

Supervisors
dr. D.S. Han
ir. J. Lucassen
prof. dr. ir. H.J.M. Swagten

Eindhoven University of Technology
Department of Applied Physics
Physics of Nanostructures

Abstract

The ever decreasing size of information technology devices following Moore's law is gradually reaching its physical limits. Therefore, there is a demand for new ways of storing and processing data. The incorporation of ultrathin layers of magnetic material opens up new paths for further improvement of for example data storage devices, like in magnetic racetrack memory, or logic devices based on spin waves. These layers can become so thin that their magnetic behavior is predominantly determined by interactions occurring at the layer interface. A particularly interesting phenomenon is the interfacial Dzyaloshinskii-Moriya interaction (i-DMI), which is of great technological importance due to its ability to stabilize chiral magnetic textures like the skyrmion. The skyrmion is a promising candidate for the next-generation data carrier due to its high stability, energy efficient manipulation and extremely small size.

In this thesis, a new setup has been developed to investigate interface interactions like i-DMI by studying their effect on propagating spin waves. The setup is first carefully tested in ferromagnetic resonance (FMR) experiments, in which Pt/Co/Pt trilayers are investigated. By varying the thickness of the Co layer, a large interface anisotropy and spin pumping contribution to magnetic damping was found. This indicates strong spin-orbit coupling at the Co/Pt interface, which is required for large i-DMI.

The setup is then used to excite surface spin waves with a non-zero wave number k using only electrical components. The spin waves propagate in opposite directions in nano-structured magnetic strips. In particular, we are interested in a difference of the resonance field of counter-propagating surface waves, which is a measure for the i-DMI in that stack. However, additional asymmetries related to damping and magnetic anisotropy at the Co interfaces complicate the picture significantly, which is often (partially) ignored in literature, their sign in particular. Nonetheless, an asymmetry in both amplitude and resonance field was found. However, no conclusive results about i-DMI could be drawn due to the limited amount of measurements that could be used in our analysis. Improving the quality of the magnetic strips, further optimization of the nano-structuring method and generally performing more systematic measurements for various wave numbers can provide more conclusive results about the magnitude and sign of i-DMI in the investigated stacks.

Contents

Chapter 1

Introduction

Enormous advancements in technology research have made the devices we use in everyday life much more sophisticated and also much smaller. Whereas the first electronic computers took up whole rooms, we can now reach the same computational power in the point of a needle. The millions of components that make up these computers have shrunk to miniature length scales for which new physics is required to understand and predict their behavior. The typical size of these components is now in the nanometer range (10^{-9} m), or about a thousand times smaller than the thickness of a human hair. For comparison, the typical size of an atom in a crystal is roughly 0.2 nm, which means that these structures are just a few to tens of atoms in size.

To further improve device functionality, new research is devoted to integrating nano-sized magnetic strips, dots and wires in these systems. Instead of using just the charge of electrons to pass and manipulate information, magnetic materials can also exploit the intrinsic magnetic moment of electrons, called the electron 'spin'. This research field of spintronics concerns itself with finding new ways to integrate spin-related physics to improve the efficiency, speed, size and stability of electronic devices. Especially by tayloring magnetic interactions at interfaces of ultra-thin films, devices can be fine-tuned for optimal performance.

During this thesis, a setup is developed which can investigate these interfacial interactions, where we will focus on the so-called interfacial Dyzoloshinskii-Moriya interaction (i-DMI). By studying its influence on periodic magnetic oscillations called spin waves, the magnitude of this interaction can be extracted. In the remainder of this chapter, the key physical concepts and methods related to the investigation of i-DMI and spin waves are introduced and an outline of this thesis is given.

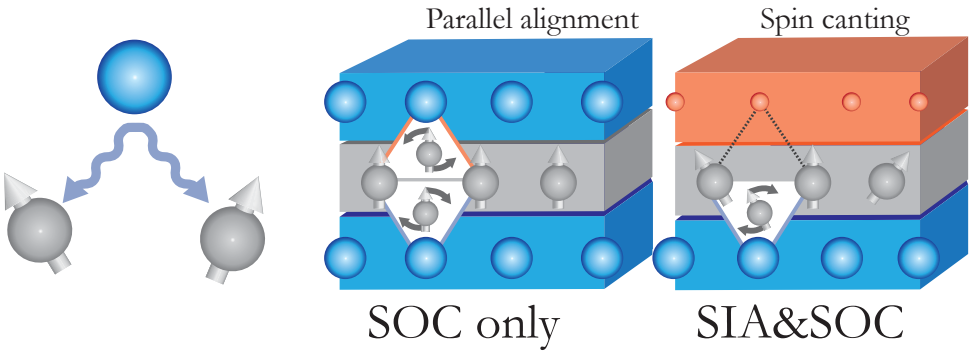

Figure 1.1: (a) Two spins, indirectly coupled by a third atom causes clockwise spin canting due to DMI. (b) The effect of interface DMI at high spin orbit coupling (SOC) interfaces depends on the orientation of the interface. In symmetric stacks i-DMI cancels (left), whereas stack inversion asymmetry (SIA) causes a net canting of neighboring spin states (right). Blue and red colors represent high and low spin orbit coupling materials, respectively.

1.1 The Dzylonshinskii-Moriya Interaction

The Dzyalonshinskii-Moriya Interaction (DMI) has regained a lot of attention in the field of spintronics since its theoretical discovery in the 1960's[1, 2]. The DMI is unique in its ability to stabilize canted magnetic configurations[3–5]. As shown in figure 1.1a, two neighboring spins are indirectly coupled by a third atom. Whitout going into detail, this coupling site is often a heavy atom like platinum or tantalum in which there is a strong interaction between electron orbital momentum and its spin, called spin-orbit coupling. The direction (chirality) of the canting is determined by the sign of the DMI, the relative position of the two spins and the direction of symmetry breaking, determined by the position of the coupling site. Experimentally, the exotic phenomenon has first been investigated in B20 structure magnetic materials[6, 7], where the lack of inversion symmetry allows for such a chiral preference.

Recently, another class of the DMI, namely interfacial DMI (i-DMI), has been also found in systems where a heavy metal (HM) with large spin orbit coupling (SOC) is in contact with a ferromagnetic (FM) film. The exact underlying physical mechanisms of the interfacial DMI are still not fully understood, so its effect is often described on a phenomenological basis. The basic concept is depicted in figure 1.1b. At each interface, the spins (in grey) couple to each other via the heavy metal atoms (in blue). This coupling cants neighboring spin states depending of the orientation of the HM/FM interface and the type of material. In the figure, counterclockwise canting occurs for

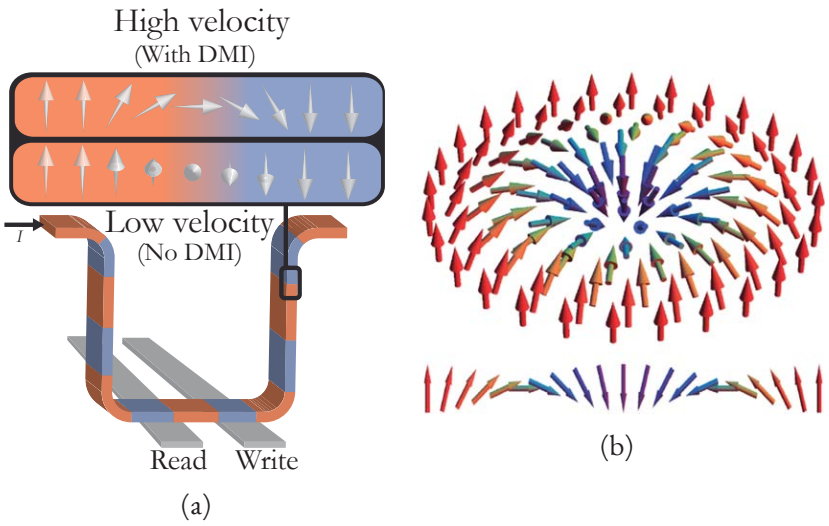

Figure 1.2: (a) Racetrack memory, where up and downwards oriented magnetic domains (red and blue respectively) are moved by an electric current I. As shown at the top, the type of domain transition affects the domain velocity. (b) A 3D and side view of the magnetic structure of a skyrmion. Figure obtained from Kézsmárki *et al.* [8].

the top interface, and clockwise canting for the bottom interface. Since there is no inversion asymmetry in the left stack, the i-DMI (and thus the canting) cancels out. For example, by using a different material for the top interface the symmetry can be broken, as depicted in the right stack. By introducing this so-called stack inversion asymmetry (SIA), a net i-DMI is generated and canting of neighboring spins occurs.

Various new magnetic memory and logic applications benefiting from i-DMI are currently being researched[9]. One of the most promising applications for data storage is the magnetic racetrack memory (figure 1.2a)[10]. It consists of three dimensional nano-structured strips of magnetic material containing a whole string of binary data. The orientation of the magnetization on one small piece on the strip, a magnetic domain, represents one bit. A major advantage of this type of memory is the use of the third dimension to store data, greatly increasing data storage density. Bits can be moved to a read/write head much more efficiently by sending current pulses through the strip, rather than physically moving the bits like in Hard-Disk Drives. For fast reading and writing, fast domain displacement is required. The highest velocities were achieved using ultra-thin multilayer stacks, which benefit from having strong spin-orbit coupling at the magnetic interfaces. For example, the presence of i-DMI stabilizes an up-down domain transition that is different from the transition without i-DMI. This is depicted at the top of figure 1.2a. It turns out that this i-DMI induced transition responds much stronger to the applied current pulses, greatly increasing domain velocities[11, 12].

Not only can i-DMI improve read and writing time, but it can also provide a new way to store data altogether. Perhaps one of the most remarkable aspects of i-DMI is its role in stabilizing a skyrmion state, shown in figure 1.2b. As depicted at the bottom of the figure, the magnetization in a skyrmion is making a full revolution with a fixed (clockwise) chirality, which can be energetically favorable in multilayer stacks with high i-DMI. The vortex-like topological soliton is one of the most promising candidates for the next-generation information carrier, as it is topologically stable, extremely small, and operational with ultralow electrical current[13]. However, much progress can still be made in developing materials and interfaces which can stabilize these skyrmions at room temperature and field-free conditions for implementation into commercial devices.

Few methods have been developed to determine the strength and sign of the i-DMI constant D. For example, domain wall based experiments like asymmetric bubble expansion have been proposed as a simple tool to measure i-DMI, but the interpretation of the results is often ambiguous[14]. In 2015, Cho *et al.* [15] showed that the DMI constant can be accurately determined by measuring the frequency of spin waves propagating in opposite directions with Brillioun light scattering (BLS). The well-defined orientation of neighboring spins in a spin wave allows for a clearer interpretation of the influence of i-DMI on the observed asymmetric propagation. Additionally, the high accuracy of the experimental tools to study spin waves turn out to be exceptionally useful for investigating i-DMI. In the following section, the basic properties of spin waves will be introduced and the experimental methods used in this thesis for the investigation of spin waves will be discussed.

1.2 Spin waves

Magnonics is an emerging field of research where we investigate the behavior of spin waves (also called magnons) in nanosized structures as a way to replace or extend conventional electronics devices. As shown in figure 1.3, spin waves are spatially oscillating excitations of the magnetization in magnetic materials. Like sound waves, spin waves have a well defined amplitude, wavelength, phase velocity, group velocity, and attenuation length. They can also interfere with other spin waves and reflect from surfaces and interfaces. This provides a versatile physical toolbox to optimize their behavior in spin wave based devices.

As early as the 1980's, spin waves have proven to be technologically useful for telecommunication systems and radar technology[16]. More recently, they have been proposed as the new generation data carriers for computation devices. The advantages of using spin waves are abundant. Examples include the low amount of Joule heating, the wide frequency range to choose from (GHz to THz), their small wavelenghts, the ability to include non-linear spin wave effects and contactless wiring (with electromagnetic

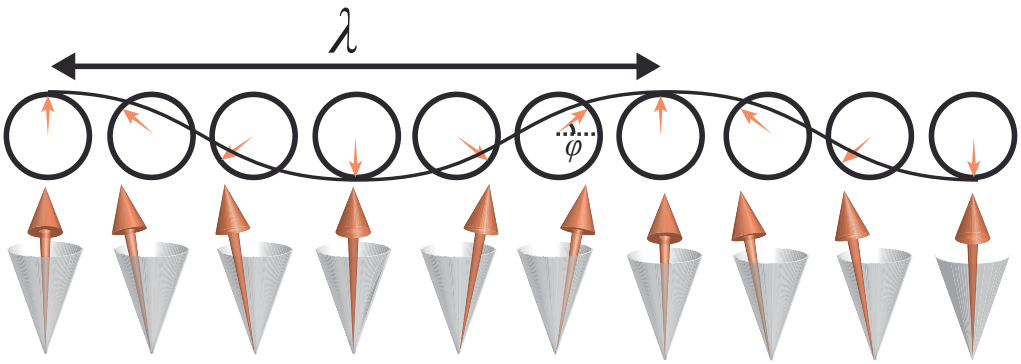

Figure 1.3: A spin wave with wavelength λ. The top circles represent the top view of the spin wave, so the deviation of the magnetization from equilibrium. At the center, the phase φ of the spin wave is given.

waves) between magnetic elements[17].

Spin waves have also proven to be an extremely versatile tool to study fundamental magnetic properties, for which various experimental techniques have been developed. In this thesis, we mainly distinguish between experiments involving uniform spin waves and experiments where propagating spin waves are investigated. For uniform spin waves, there is no spatial phase variation and the magnetization oscillates as a collective, equivalent to $\lambda \to \infty$ in figure 1.3. Uniform precession is most often investigated in ferromagnetic resonance (FMR) experiments to for example measure magnetization relaxation mechanisms in thin films. Propagating spin waves, like the one shown in figure 1.3, do have a spatial variation in phase, have non-zero group velocities and finite wavelengths. The properties of propagating spin waves are exploited in propagating spin wave spectroscopy (PSWS) experiments to extract, for example, the effect of currents on spin dynamics[18] or the i-DMI constant. Both FMR and PSWS are used in this thesis to study interface effects in ultrathin Co/Pt multilayers, where the latter method will focus on i-DMI. Both methods will be briefly introduced in the following sections.

Ferromagnetic resonance

In ferromagnetic resonance (FMR) experiments a magnetic sample is placed in an externally applied magnetic field $\boldsymbol{H}_{\text{ext}}$. As shown in figure 1.4a, the magnetization of the sample is collectively pulled out of equilibrium by a radio-frequency magnetic field $\boldsymbol{H}_{\text{rf}}$ (e.g. gigahertz microwave radiation). The applied magnetic field exerts a torque on the magnetization, causing a precessional motion of the magnetization. Additionally, internal fields resulting from a wide range of magnetic interactions also contribute to the precession torque, causing a net torque equivalent to that of an effective field

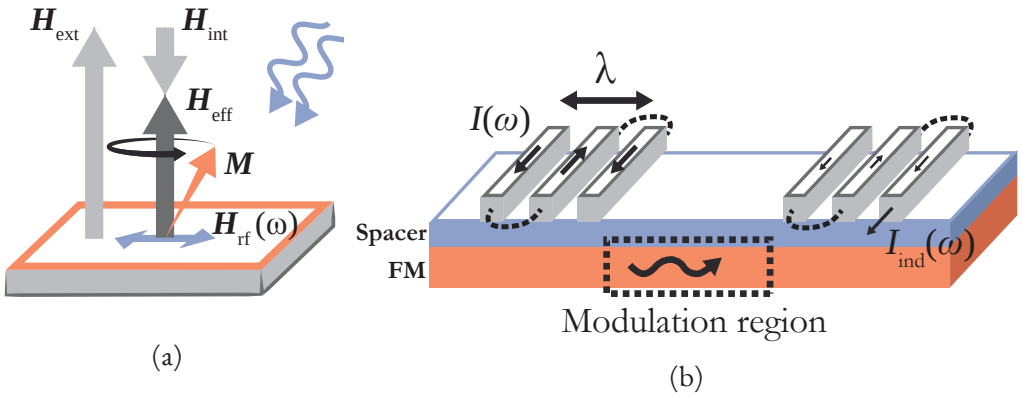

Figure 1.4: (a) A high frequency field (blue arrows) bring the magnetization into precessional motion around an effective field H_{eff}, which is a sum of the externally applied field H_{ext} and intrinsic fields H_{int} in the sample. (b) By sending a current $I(\omega)$ through an antenna structure, propagating spin waves with wavelength λ are excited in a ferromagnetic (FM) strip. An inductive current I_{ind} is generated in the detection antenna. In the region between the antennas, the spin wave can be modulated by external means.

$\boldsymbol{H}_{\text{eff}} = \boldsymbol{H}_{\text{ext}} + \boldsymbol{H}_{\text{int}}$. By measuring the precession frequency for a given $\boldsymbol{H}_{\text{ext}}$, the intrinsic magnetic field can be extracted.

Examples of intrinsic properties that can be measured using FMR include the rate of magnetic energy dissipation, characterized by the damping parameter α, or the tendency of the magnetization to align with a specific crystal axis, given by the anisotropy constant K. In recent years, many other promising applications of FMR have been developed due to its ability to generate pure spin currents in ferromagnetic metal/normal metal devices in a process known as spin pumping[19]. Spin currents transfer no net charge and can be utilized in a wide range of spintronics applications, enabling for example low-power and high-bandwidth information transfer[20]. Spin pumping also allowed for accurate measurements of fundamentally and technologically interesting magnetic properties. Examples include the spin hall angle, which is a measure for the efficiency between charge and spin current conversion, and the spin diffusion length, which is the mean distance that a spin can diffuse before flipping[21].

Propagating spin wave spectroscopy

As described in the previous section, the vast amount of information contained in the FMR mode makes it an extremely valuable tool in magnetic research. However, in these experiments the excited spin waves carry no momentum ($k \equiv 2\pi/\lambda = 0$). To investigate information transport in magnetic systems, various techniques have been devel-

oped that study $k \neq 0$ spin waves. Optical studies often involve Brillioun light scattering, while all-electrical means of exciting and detecting spin waves is often referred to as propagating spin wave spectrocopy (PSWS).

In 1973, Schilz [22] first used this all-electrical approach to confirm theoretical predictions of propagating spin-wave behaviour in low-loss epitaxial yttrium iron garnett (YIG) films. A meander shaped spin-wave transducer and receiver are placed on two different positions on the YIG film. The basic concept is demonstrated in figure 1.4b. By sending a high frequency current trough the transducer, it excites spin waves with its Oersted field. The wavelength is determined by the meander periodicity. The spin waves then propagate outward, inductively generating a signal at the detection antenna. Later, Bailleul *et al.* [23] extended the use of this method to metallic magnetic strips, using two coplanar antennas for excitation and detection. An insulating layer is used to prevent shunting currents between the antennas.

In 2015, Cho *et al.* [15] showed that a certain type of spin wave can be used to extract the i-DMI constant. Using Brillioun light scattering (BLS), magnetostatic surface spin waves were excited and detected. Interestingly, spin waves with a wave number $+k$ propagated at different frequencies than spin waves with wave number $-k$. Calculations showed that the frequency difference $(\omega_{+k} - \omega_{-k})$ is proportional to the DMI constant D[24]. Using BLS, the i-DMI constants have been determined for a variety of stacks, such as Pt/CoFeB[25] and Pt/Co/AlOx[26], with magnetic layer thicknesses down to 0.6 nm. However, BLS has the disadvantage that laser light can be absorbed when additional layers are deposited on top of the magnetic layer, which decreases the measurement accuracy.

Later in 2015, Lee *et al.* [27] also succeeded to measure the i-DMI-constant with electrical components only, using the principle described in figure 1.4b. This method is not as strongly affected by thick capping layers, since the signals are generated inductively. Using the all-electrical approach, i-DMI constants have been determined for Permalloy stacks[28] and Pt/Co/MetalOxide stacks[29]. However, additional asymmetries in, for example, the spin wave amplitudes have been ignored in the analysis. These asymmetries can significantly contribute to the measured signals[30] and hold valuable information about the magnetic interfaces. In this thesis, the analysis takes into account the various processes involved in asymmetric propagation and attempts to distinguish between the dominant mechanisms.

1.3 This thesis

The goal of this thesis is to develop a setup to investigate asymmetric propagation of spin waves. We focus on the influence of i-DMI at Pt/Co interfaces. Although these interfaces have been investigated before in literature, the analysis often neglected the contribution of asymmetric spin wave amplitudes and damping. This thesis will dis-

cuss the influence of both asymmetries in our analysis. During the development of this novel setup, FMR experiments have been performed to extensively test the setup and to investigate the physical processes at Co/Pt interfaces. Since the FMR measurements are a significant part of this thesis and the theory and methods behind these experiments do not sufficiently overlap with the asymmetrical spin wave propagation experiments, they will each be treated in a separate part in this thesis. However, the FMR results do complement the PSWS experiments in the sense that they provide a better understanding of the observed spin wave behavior.

In **chapter 2**, a brief and general introduction will be given to micromagnetic theory to provide a better understanding of the physical mechanisms contributing to magnetization dynamics. We then address the FMR and PSWS experiments separately in two parts.

PART 1 In part 1 Co/Pt interfaces will be investigated using an FMR setup developed during this thesis. First, in **chapter 3** the theory behind FMR is explained. The equations required for obtaining magnetic properties from the magnetic susceptibility χ of a sample will also be introduced. In **chapter 4**, the developed FMR setup used to measure χ will be described and tested. As a verification of the magnetic parameters obtained by FMR, anomalous hall magnetometry will be utilized, which is also introduced in this chapter. In **chapter 5**, we will present a systematic study of interface induced anisotropy and damping effects for Co/Pt multilayers. Part 1 will be concluded by providing additional remarks on the setup and the measurements, and propose several improvements on the developed setup.

PART 2 In part 2, the FMR setup is slightly altered to investigate the asymmetric propagation of spin waves due to i-DMI. First, in **chapter 6** the theory behind nonreciprocal spin wave behavior will be discussed, where we will focus on the effect of i-DMI. Additionally, an analytical model is introduced which can be used to calculate the theoretical magnetic response of the samples used in our experiments. In **chapter 7**, the PSWS setup will be described and the experimental tools required for the fabrication of the nano-structured samples in these experiments are discussed. In **chapter 8** we will verify that the correct spin waves are excited and the results regarding asymmetric spin wave propagation will be presented. In **chapter 9**, this thesis will be concluded and several proposals will be made for future research with the developed setup.

Chapter 2

Fundamentals of micromagnetics

Magnetic systems often involve a vast amount of quantum mechanical, electrical and magnetic interactions between electrons, atoms and their environment. Understanding the behavior from a quantum mechanical point of view becomes a nearly impossible venture, even for micrometer sized systems. Instead, we describe systems in the nano- to micrometer regime with a local magnetization vector $\boldsymbol{M}(\boldsymbol{r}, t)$. This magnetization vector interacts with a local effective field $\boldsymbol{H}_{\text{eff}}(\boldsymbol{r}, t)$, which in its turn often also depends on $\boldsymbol{M}(\boldsymbol{r}, t)$. This already simplifies the highly complex system of interactions to a number of coupled equations of motion. These equations can then be solved to for example describe the behavior of spin waves in ferromagnetic resonance or propagating spin wave spectroscopy experiments.

In this chapter we will describe how $\boldsymbol{H}_{\text{eff}}$ can be obtained from the free energy W of a magnetic film. We will then show how to derive the time evolution $\boldsymbol{M}(t)$ from the effective field. To get a better understanding of the processes driving the magnetization dynamics, the focus of this chapter will lie on providing a physical interpretation of the equations involved.

2.1 Free energy of a thin magnetic film

For ferromagnetic films we can distinguish between various energy contributions that together determine the behavior of the magnetization vector $\boldsymbol{M}(t)$. The total energy can be expressed as a sum of the volume integrals of individual energy densities E_i,

$$W = \int_V \sum_i E_i dV \tag{2.1}$$

The underlying physical mechanisms can roughly be divided into four categories, as shown in figure 2.1. Spins can either align to an external field, to a specific axis (or axes),

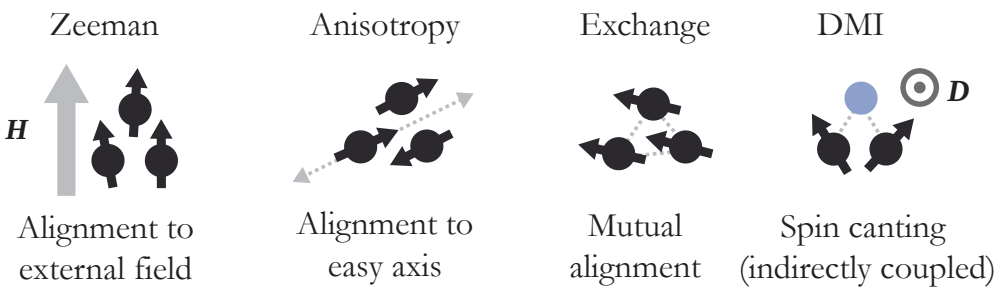

Figure 2.1: Various contributions to the magnetic free energy are shown and their effect on the local magnetization. The DMI-vector $\boldsymbol{D}$ is shown for the case where the two spin sites and the coupling site are lying in the plane of the paper.

align mutually or even prefer a canted spin state. We will shortly discuss the most important underlying physical mechanisms of the energy densities for films where the thickness t of the film is much smaller than its lateral dimensions L, so $t \ll L$.

1. **Zeeman energy**
   An applied magnetic field $\boldsymbol{H}$ exerts a torque on a dipole moment. The energy associated with this torque is called the Zeeman energy. It is lowest in an aligned state and highest in antiparallel configuration. It can be calculated by taking the inner product
   $$E_{\text{Zeeman}} = -\mu_0 \boldsymbol{H} \cdot \boldsymbol{M}. \tag{2.2}$$

2. **Magnetic anisotropy**
   For *isotropic* magnetic samples, the energy functional is invariant under rotation of the system. However, this is not often the case, especially for thin ferromagnetic samples. When there are axes along which a magnetic structure prefers to be magnetized (also called the 'easy axes'), we speak of magnetic anisotropy. Many physical mechanisms exist that cause this anisotropy. The crystal structure, strain, physical shape and spin-orbit coupling at interfaces all contribute. The most important contributions to magnetic anisotropy for this thesis are listed below.

   Shape anisotropy Any magnetic object generates magnetic charges at its surface, which depend on the orientation of the magnetization. For anisotropic shapes, like for thin films, these free charges generate a so-called demagnetization field $\boldsymbol{H}_{\text{demag}} = \overline{\overline{\mathcal{N}}}\boldsymbol{M}$ pulling the magnetization to a certain easy axis or easy plane. The tensor $\overline{\overline{\mathcal{N}}}$ is called the demagnetization tensor, which can often only be calculated numerically. Fortunately, for the case of thin films lying in the xy-plane,

the only nonzero component of the demagnetizing tensor is $\mathcal{N}_{zz} = 1$[31]. The energy is then expressed as

$$E_{\text{Demag}} = \frac{1}{2}\boldsymbol{M} \cdot \mu_0 \boldsymbol{H}_{\text{Demag}} = \frac{1}{2}\boldsymbol{M} \cdot \overline{\overline{\mathcal{N}}}\mu_0 \boldsymbol{M} = \frac{1}{2}\mu_0 M_z^2, \tag{2.3}$$

which is minimized if $M_z = 0$. In other words, shape anisotropy for thin films favors a magnetization in the plane of the sample.

Crystalline anisotropy For some (poly-)crystalline systems an additional anisotropy term is present. Orbital moments of electrons in a crystal are anisotropic by nature due to bonding of orbitals with neighboring atoms and therefore depend on the crystal structure of the lattice. In the presence of spin-orbit coupling, the orbital moments couple to the magnetization, which gives rise to so-called crystalline anistropy. Depending on the symmetry of the lattice, multiple easy and hard axes can be present. For the case of one easy axis, uniaxial anistropy, we can derive an expression for the energy density

$$E_{\text{cryst}} = K_U \sin^2(\phi), \tag{2.4}$$

where K_U is the anisotropy constant and ϕ is the angle between the easy axis and $\boldsymbol{M}$. The energy is minimized when $\phi = 0$, meaning that the magnetization is aligned with the easy axis.

Interface anisotropy While the crystal structure can induce a magnetic anistropy in the bulk of the sample, the interfaces of magnetic films can also significantly contribute to the magnetic anisotropy. Especially when films are just a few or tens of atoms thick, these interface effects can be a dominant contribution to the free energy. For example, at ferromagnetic metal/heavy metal interfaces, the out of plane d-orbital moment of FM atoms is signicantly enhanced[32]. For spin-orbit coupling materials like Pt or Pd, the orbital momentum couples to the total magnetic moment, resulting in a strong magnetic anisotropy parallel to the normal of the ferromagnetic film. The magnitude of the anisotropy energy E_K is often given in terms of the surface anisotropy constant K_S, with units J/m^2, divided by the thickness of the magnetic layer t_{FM}. For a ferromagnetic layer with two non-identical interfaces this means

$$E_{\text{K}} = \frac{K_S}{t_{\text{FM}}} m_z^2 = \frac{K_{\text{s,top}} + K_{\text{s,bot}}}{t_{\text{FM}}} m_z^2. \tag{2.5}$$

Here, $m_z = M_z/M_S$ is the normalized z-component of the magnetization. The equation can be transformed to the form of equation 2.4 by noting that the easy

axis is along the z-axis, such that $\sin(\phi) = m_z$. Note that K_S is defined as the *total* surface anisotropy, consisting of both the surface anisotropy constant of the top and bottom interface, $K_{\text{s,top}}$ and $K_{\text{s,bot}}$ respectively.

3. **Exchange interaction**
   Like shown in figure 2.1, the exchange interaction prefers mutual alignment between spins. The interaction originates from the fact that the Coulomb energy between aligned spin states is lower than for canted spin states. The energy related to this interaction does not change under the inversion of two spins and is thus often referred to as a symmetric exchange interaction. The energy density equals

$$E_{\text{ex}} = A(\boldsymbol{\nabla m})^2, \tag{2.6}$$

   where A is called the exchange constant, units J/m, and represents the strength of this interaction. The vector $\boldsymbol{m} = \boldsymbol{M}/M_S$ is again the normalized magnetization. The exchange energy is minimized when the gradient of the magnetization equals zero, meaning that the magnetization is parallel throughout the film.

4. **Dzyalonshinskii-Moriya Interaction**
   The final interaction that will be discussed is the Dzyalonshinskii-Moriya interaction (DMI)[33, 34]. As shown in figure 2.1, the DMI prefers canted spin states. It is often described as an asymmetric exchange interaction between two spins $\boldsymbol{S}_i$, mediated by a third site having strong spin-orbit coupling. Due to symmetry considerations the direction of the DMI-vector $\boldsymbol{D}$, units J/m^2, is limited to the directions perpendicular to both the line connecting the two spins and the direction of symmetry breaking[35]. Therefore, in figure 2.1, it is oriented parallel to the normal of the plane of the paper. The interaction is most intuitively described with an Hamiltonian for two spins,

$$\mathcal{H}_{\text{DMI}} = \boldsymbol{D} \cdot [\boldsymbol{S}_1 \times \boldsymbol{S}_2]. \tag{2.7}$$

   Interesting is that the energy does not only depend on the amount of canting of the magnetization, but also the direction (chirality) of the canting. If the energy is *increased* for a clockwise canting of spins, then the energy is *decreased* for counterclockwise canting and vice versa. In equation 2.7, this can be clearly seen by noting that the hamiltonian is antisymmetric under the exchange of the two spins $1 \leftrightarrow 2$.

   In the continuum limit, the DMI is calculated using so-called Lifshitz invariants. They consist of an antisymmetric form of the product between the components of the magnetization M_i and its derivatives $\frac{\partial M_j}{\partial k}$, where i, j and k represent any combination of the xyz-coordinates[36]. In vector notation, the energy density

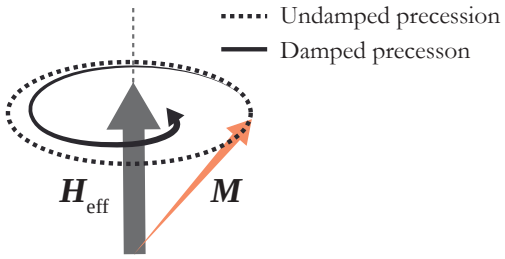

Figure 2.2: The magnetization vector of a magnetic material will precess around its effective magnetic field $\boldsymbol{H}_{\text{eff}}$. In a real magnetic system, damping is also present. This will eventually align $\boldsymbol{M}$ to $\boldsymbol{H}_{\text{eff}}$

for the DMI can then be expressed as[37]

$$E_{\text{DMI}} = \frac{\boldsymbol{D}}{M_S^2} \cdot (\boldsymbol{M}(\boldsymbol{\nabla} \cdot \boldsymbol{M}) - (\boldsymbol{M} \cdot \boldsymbol{\nabla})\boldsymbol{M}) \,. \tag{2.8}$$

The vector $\boldsymbol{D}$ has a net non-zero magnitude only if inversion symmetry is broken in the magnetic system. This can occur in the bulk for certain crystal structures, but also near high SOC interfaces of thin magnetic films. If such a film has a different top and bottom interface, the symmetry in the direction of the normal of the film is broken, resulting in a net interface DMI vector in the plane of the sample. If we take the normal of the sample to be the z-axis, the only remaining antisymmetric terms of the Liftshitz invariant are

$$E_{\text{i-DMI}} = \frac{D_S}{t_{\text{FM}}} \left(\left[m_z \frac{\partial m_x}{\partial x} - m_x \frac{\partial m_z}{\partial x} \right] + \left[m_z \frac{\partial m_y}{\partial y} - m_y \frac{\partial m_z}{\partial y} \right] \right) . \tag{2.9}$$

Since the interaction originates from the interface, its contributions decreases with increasing magnetic layer thickness. Therefore, we have substituted the magnitude of D by a surface constant D_S, units J/m, divided by the thickness of the ferromagnetic layer t_{FM}. This version of the energy density will be used in part 2 of this thesis, where we will calculate the influence of i-DMI on propagating spin waves.

2.2 Magnetization dynamics

In the previous section we have derived the various contributions to the free energy of a magnetic film. By minimizing the energy functional (equation 2.1), it is possible to find an equilibrium condition for $\boldsymbol{M}$. However, it is often more interesting to know

how the magnetization arrives at this state. The following section will introduce the micromagnetic equations of motion, from which the time evolution of the magnetization can be calculated. An excellent intuitive derivation can also be found in chapter 1 of Hillebrands and Ounadjela [38].

The first step in obtaining the time evolution of the magnetization is to determine the forces acting on it, given by the effective field $\boldsymbol{H}_{\text{eff}}$. It is obtained from the free energy functional by taking its derivative to the normalized magnetization vector $\boldsymbol{m}$,

$$\mu_0 \boldsymbol{H}_{\text{eff}} = -\frac{1}{M_s}\frac{\partial W}{\partial \boldsymbol{m}}. \tag{2.10}$$

This can be inserted in the so-called Landau-Lifshitz-Gilbert (LLG) equation, which is given by

$$\frac{\partial \boldsymbol{M}}{\partial t} = -\gamma \left(\boldsymbol{M} \times \boldsymbol{H}_{\text{eff}} - \alpha \boldsymbol{M} \times \frac{\partial \boldsymbol{M}}{\partial t} \right). \tag{2.11}$$

Here, γ is the gyromagnetic ratio and α the phenomenological damping parameter. In the LLG-equation we can distinguish between two processes, both depicted in figure 2.2. The process given by the first term on the right hand side of the equation describes the precessional motion of $\boldsymbol{M}$ around $\boldsymbol{H}_{\text{eff}}$. This process is the magnetic analog of the precessing motion of a spinning top subject to a gravitational force. The second term describes a damping force pulling the magnetization parallel to $\boldsymbol{H}_{\text{eff}}$. This effective force arises from various energy loss channels, which are described in more detail in the next section. Both processes lead to a damped precessional motion as depicted by the solid line in figure 2.2.

The gyromagnetic ratio γ relates the magnetic moment of the system to its angular momentum. It is often expressed in terms of a dimensionless quantity called the g-factor, such that $\gamma = \frac{g\mu_B}{\hbar}$, where μ_B is the Bohr magneton and $\hbar$ the reduced Planck constant. The g-factor contains both the spin magnetic moment μ_S and the orbital magnetic moment μ_L. For purely orbital magnetic moment, $g = 1$, while for purely spin magnetic moment $g = 2$. For solid state systems, the orbital angular momentum is often quenched, resulting in a g-factor close to 2. However, spin-orbit coupling or symmetry breaking near the interfaces can decrease this quenching, increasing the g-factor.

Magnetic Damping

The damping term in the LLG equation accounts for all physical processes that cause energy dissipation in the magnetic system. It is often described as a separate term in the LLG equation. However, for future derivations it will be useful to rewrite the damping contribution in terms of a time-dependent effective field[38], giving

$$\boldsymbol{H}_{\text{eff}} = \boldsymbol{H} - \alpha \frac{1}{\gamma \mu_0 M_s}\frac{\partial \boldsymbol{M}}{\partial t}. \tag{2.12}$$

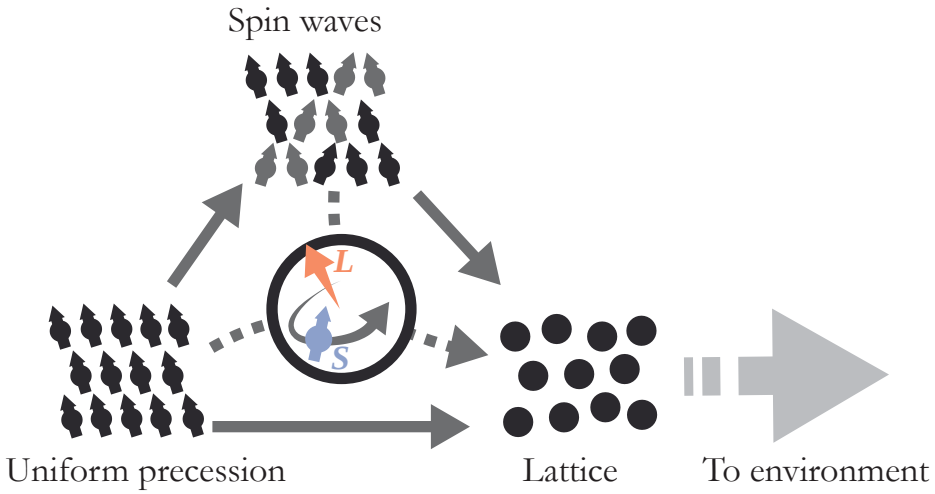

Figure 2.3: Damping can occur via various channels. Both direct damping and indirect damping via spin wave excitation contribute. The coupling between the angular momentum $\boldsymbol{L}$ and spins $\boldsymbol{S}$ is essential for describing the magnitude of the damping mechanisms.

By inserting this effective field into the LLG equation without damping, we directly obtain the original expression (equation 2.11). A similar substitution for the effective field will be used in later chapters to include damping in the equations describing spin wave behavior in FMR and PSWS experiments.

Various physical origins can be distinguished for magnetic damping. The two most dominant loss channels are depicted in figure 2.3. Energy is either lost directly to the lattice or transferred to the magnetic system due to scattering with other spin waves (also called magnons) which then lose it to the lattice. Both direct and indirect damping are enhanced by spin-orbit coupling. We will discuss several of the main contributors to damping in thin ferromagnetic films.

Itinerant electrons A large contribution to intrinsic damping is due to scattering of magnons with itinerant electrons[39]. A magnon can be annihilated by transferring its momentum to the electron and simultaneously flipping the electron spin to conserve the total spin angular momentum. The electron then loses its energy to the lattice, for example by scattering with phonons. Moreover, magnon annihilation due to scattering without spin-flip is also possible due to strong spin-orbit interaction. The spin angular momentum of magnons is then directly transfered to orbital moment of the electron. This spin-orbit coupling assisted scattering is believed to be the main contribution to

intrinsic damping in metallic ferromagnets[40].

Two-magnon scattering Extrinsic contributions can also significantly increase the effective damping in a ferromagnetic thin film. For example in ferromagnetic resonance experiments, where the collective precession of the magnetization vector is studied, two-magnon scattering can cause a large additional relaxation of the magnetic system[41]. It is caused by structural defects in the magnetic film, causing local changes in the effective field. The inhomogeneities can excite spin waves with finite wavelength ($k \neq 0$) degenerate with the collective precessional mode. However, this degeneracy is lifted when the equilibrium magnetization is directed out of the plane, significantly reducing two-magnon scattering.

Spin pumping Other forms of extrinsic contributions to magnetic damping occur in layered systems. Especially in ultra-thin magnetic films these interface related phenomena can become larger than dissipation in the bulk. For example, spin pumping occurs when a ferromagnetic layer is in contact with a non-magnetic layer. An oscillating (precessing) magnetic moment causes spin injection in the non-magnetic layer. Without going into too much detail, this flow of spins (a spin current) leaving the ferromagnetic layer causes a net loss in magnetic free energy, which can be quantified as an additional contribution to the damping,

$$\alpha_{\text{pump}} = \frac{\hbar\gamma g^{\uparrow\downarrow}}{2\pi M_S}\frac{1}{t_{\text{FM}}}, \tag{2.13}$$

where t_{FM} is the thickness of the ferromagnetic layer. The spin mixing conductance $g^{\uparrow\downarrow}$ is related to spin scattering at the interface and is a measure for how transparant an interface is to such a spin current[42].

The equations given in this chapter form a mathematical foundation for calculating magnetization dynamics in thin films. In the remainder of this thesis we will use them to derive the behavior of spin waves in thin films. In particular, the effect of interface related phenonema like interface anisotropy, i-DMI and spin pumping will be addressed.

Part I

An FMR study on spin-orbit coupling at Co/Pt interfaces

In part 1 of this thesis we investigate the influence of the Co/Pt interface on the magnetic properties of thin Co films. These interfaces are interesting from a technological point of view since their tunablity combined with high-spin orbit coupling provide an easy and versatile toolbox to customize magnetic properties. We distinguish between bulk and interfacial effects by varying the thickness of the Co layer. Magnetic properties are studied using a ferromagnetic resonance setup developed during this thesis. While understanding these interfacial mechanisms is interesting from a fundamental point of view, it also helps us to understand the non-reciprocal spin wave behavior studied in part 2 of this thesis.

First, the relevant equations for this study will be discussed. Secondly, the experimental setup will be described and its performance will be tested. Finally, we will discuss the FMR results considering magnetic anisotropy and damping effects arising from the Co/Pt interface, followed by a discussion on the limitations of the setup and propose several improvements.

Chapter 3

Theory of ferromagnetic resonance

In ferromagnetic resonance (FMR) experiments, a small high frequency magnetic field $\boldsymbol{H}_{\text{rf}}$ is applied to a magnetic sample. As shown in figure 3.1, the magnetization will start to precess around its effective field $\boldsymbol{H}_{\text{eff}}$. If the frequency of the perturbing field is equal to the precession frequency around the effective field, the magnetization is brought into resonance. The precessional response is quantified by the susceptibility χ, which peaks if the resonance condition is met. An FMR setup is able to measure χ such that the strength of the internal fields arising from, for example, magnetic anisotropy can be extracted.

Using the LLG-equations from the previous chapter, we first derive an expression for the suscepbility χ. We will fist consider the simple case where only Zeeman energy is contributing to the magnetization dynamics. We subsequently add additional energy terms, such that the resulting equations can be used in FMR experiments to extract magnetic properties like the anistoropy and damping. A more detailed derivation can be found in section 3.7 of Stancil and Prabhakar [31].

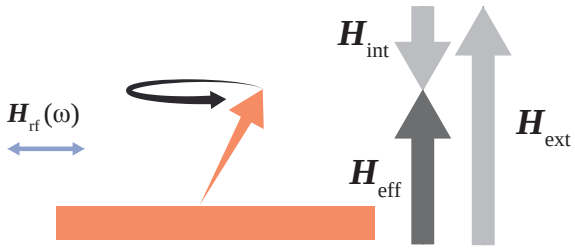

Figure 3.1: A high frequency magnetic field $\boldsymbol{H}_{\text{rf}}$ acts on the magnetization with a frequency ω. The magnetization starts to precess around an effective field $\boldsymbol{H}_{\text{eff}}$ consisting of internal and externally applied fields, $\boldsymbol{H}_{\text{int}}$ and $\boldsymbol{H}_{\text{ext}}$ respectively.

3.1 Polder susceptibility tensor

For small harmonic perturbations, we can analytically solve the LLG-equation (2.11) to find the time evolution of the magnetization $\boldsymbol{M}(t)$. We first split the magnetic field and magnetization into a constant and small harmonic time varying component, such that

$$\boldsymbol{M}(t) = \boldsymbol{M}_0 + \boldsymbol{m}(t); \qquad \boldsymbol{H}_{\text{eff}}(t) = \boldsymbol{H}_0 + \boldsymbol{h}(t) \tag{3.1}$$

We assume that $|\boldsymbol{m}(t)| \ll |\boldsymbol{M}_0|$ and $|\boldsymbol{h}(t)| \ll |\boldsymbol{H}_0|$. These equations can be inserted in the LLG-equation with only the precessional term. We will add damping later, as described in section 2.12. This results in

$$\frac{\partial \boldsymbol{M}}{\partial t} = \gamma\mu_0 \left(\boldsymbol{M}_0 \times \boldsymbol{H}_0 + \boldsymbol{M}_0 \times \boldsymbol{h} + \boldsymbol{m} \times \boldsymbol{H}_0 + \boldsymbol{m} \times \boldsymbol{h}\right) \tag{3.2}$$

Since in equilibrium, $\boldsymbol{M}_0$ and $\boldsymbol{H}_0$ are parallel to each other, the first term vanishes. The perturbations are assumed to be small, so we also neglect the last (second-order) term.

We take the applied field along the y-axis of our film, so $\boldsymbol{H}_0 = H_0\hat{\mathbf{y}}$ and $\boldsymbol{M}_0 = M_S\hat{\mathbf{y}}$. Since we know that our time dependence is harmonic, we can simply take the derivative of $\exp(-i\omega t)$ for the left hand side of the equation, resulting in

$$-i\omega\boldsymbol{m} = -\gamma\mu_0(\hat{\mathbf{y}} \times (-M_S\boldsymbol{h} + H_0\boldsymbol{m})\,. \tag{3.3}$$

The equation can be put into matrix form in the form of $\boldsymbol{h} = \overline{\overline{\chi}}^{-1}\boldsymbol{h}$, where $\overline{\overline{\chi}}$ is the so-called Polder susceptibility tensor. Inverting the equation gives the solution for the Polder tensor

$$\overline{\overline{\chi}} = \begin{pmatrix} \chi & -i\kappa \\ i\kappa & \chi \end{pmatrix}, \tag{3.4}$$

where its components are given by

$$\chi = \frac{H_0 M_S}{H_0^2 - (\frac{\omega}{\gamma\mu_0})^2} \quad \text{and} \quad \kappa = \frac{M_S\frac{\omega}{(\gamma\mu_0)}}{H_0^2 - (\frac{\omega}{\gamma\mu_0})^2}. \tag{3.5}$$

From the denominators we can see that the magnetic response blows up once the frequency ω approaches $\gamma\mu_0 H_0$, indicating that the system is brought into resonance. To correct for this seemingly unphysical behavior, we need to introduce a damping term. As mentioned in section 2.2, this can be done by making the substitution $H_0 \to H_0 + i\alpha\omega/(\gamma\mu_0)$. Alternatively, we can obtain the same equation by performing the same derivation steps as above for the LLG-equation with damping.

Influence of anisotropy

In the previous section we have derived the precessional response in the simple case where the only term contributing to the free energy is the Zeeman energy. However, as described in section 2.1, both shape- and interface anisotropy contribute significantly to the energy of a thin magnetic film. Therefore, we include an out-of-plane anisotropy field H_K due to interface anisotropy. Also, due to the out of plane component m_z of the magnetization during precession, we should include a demagnetizing field (section 2.1), giving

$$\boldsymbol{h}_\mathrm{d} + \boldsymbol{h}_\mathrm{K} = -\mathcal{N}\boldsymbol{m} + \frac{H_\mathrm{K}}{M_S} m_z \hat{\boldsymbol{z}} = -\begin{pmatrix} 0 & 0 \\ 0 & 1 - \frac{H_K}{M_S} \end{pmatrix} \boldsymbol{m}. \tag{3.6}$$

Here we have considered a geometry where the sample lies in the xy-plane with an applied field and equilibrium magnetization in the y-direction. Both fields in equation 3.6 can be added to the effective field in equation 3.1. Following the same derivation as before and including damping, we obtain

$$\chi_{xx} = \frac{M_S(H_z - i\alpha\frac{\omega}{\gamma\mu_0})}{H_x H_z - (\frac{\omega}{\gamma\mu_0})^2 - i\frac{\Delta H}{2}(H_x + H_z)}, \tag{3.7}$$

where

$$H_z = H + M_S - H_K \qquad \text{and} \qquad H_x = H \tag{3.8}$$

are the effective fields felt by an out-of plane and an in-plane perturbation, respectively, where H is the external magnetic field. For convenience, the subscript 'ext' will be dropped for the remainder of part 1. The magnetic response peaks when the applied frequency ω (second term in the denominator) matches the precession frequency corresponding to the product of these effective fields. The parameter ΔH corresponds to the width of the peak, and is defined as $\Delta H \equiv 2\alpha\frac{2\pi f}{\gamma\mu_0}$ (for a formal proof, see for example section 3.8 in Stancil and Prabhakar [31]). Note that for simplicity we have only considered the first component of the susceptibility tensor, χ_{xx}. This is only valid for experiments where there is only an in-plane perturbation field (so $h_z = 0$). If this is not the case, other components should be taken into account as well.

In figure 3.2, the real and imaginary part of χ_{xx} are plotted as a function of the applied field for typical magnetic parameter values of Co. The graphs form an anti-symmetric and symmetric Lorentzian curve, respectively. The applied frequency equals $f = \omega/2\pi = 10$ GHz, giving a resonance field $H_\mathrm{res} = 56$ mT. As shown in the figure, the full width at half maximum of the imaginary part equals $\Delta H = 7$ mT. Both H_res and ΔH are a function of the unknown magnetic parameters. This shows one of the major advantages of FMR: from a single set of measurements of χ, we can extract information about H_K, M_S and α.

Now that we know there is a relation between the intrinsic magnetic parameters and the lineshape of χ, we can exploit this in FMR measurements. In the following section

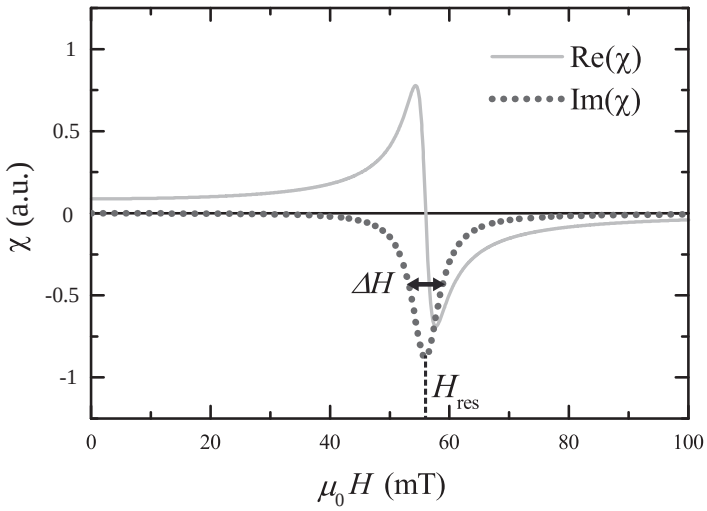

Figure 3.2: The imaginary and real part of the susceptibility have a Lorentzian line shape. The width of the peak ΔH correlates with the damping parameter α and the resonance field H_{res} with the intrinsic magnetic parameters γ, H_K and M_S.

we will show how to properly extract all these parameters and distinguish between the bulk and the interface contributions.

3.2 Extracting bulk and interface effects

As mentioned in the previous section, from the resonance field and linewidth extracted from χ, the magnetic parameters can be derived. In the setup developed in the thesis, two different methods can be used to measure χ. We can either

1. fix the perturbation frequency f, and sweep the applied magnetic field H to extract H_{res} (similar to figure 3.2), or

2. apply a static external field H, and sweep the applied frequency f to extract f_{res}.

The former is called field-swept FMR and the latter frequency-swept FMR. Both methods measure χ and determine the resonance field or frequency and corresponding linewidths by fitting it to equation 3.7. However, there are subtle differences between the methods to extract magnetic properties. For example, in frequency swept FMR we can only measure a linewidth Δf, which has a different relation to α than ΔH. These differences will be discussed in more detail in the following sections. Both methods will be compared in section 4.1 to verify consistency between the measurements of the developed setup.

Extracting Anisotropy

First, we derive a relation between the resonance field H_{res} and the magnetic anisotropy. We first expand equation 3.7 and set the denominator of the imaginary part to 0 to find the peak position. Assuming that $\Delta H^2 \ll H_{\text{res}}^2$, we find

$$f^2 = \left(\frac{\gamma \mu_0}{2\pi}\right)^2 H_{\text{res}}(H_{\text{res}} + M_{\text{eff}}), \tag{3.9}$$

where $M_{\text{eff}} = M_S - H_K$. This is known as the Kittel equation for in-plane geometries with an out-of-plane anisotropy component H_K. From field sweep measurements H_{res} can be determined for various f, such that the results can be fitted to the Kittel equation with γ and M_{eff} as fitting parameters. The inclusion of γ as a fitting parameter is required, since for thin films the g-factor is often enhanced due to spin-orbit coupling (see section 2.2). Note that in this configuration there is no way to distinguish between the influence of M_S and H_K since the fitting parameters would be mutually dependent. For frequency swept FMR, the same relation holds with the only difference that the resonance frequency f_{res} is used instead of f and the constant applied field H instead of H_{res}.

To obtain the surface anisotropy constant K_S, we determine the effective anisotropy constant $K_{\text{eff}} \equiv -\frac{1}{2}\mu_0 M_{\text{eff}} M_s$ for various Co thicknesses t_{Co}. The sign is chosen such that negative K_{eff} corresponds to in-plane anisotropy and positive values to perpendicular (out-of-plane) anisotropy. We get for the effective anisotropy constant

$$K_{\text{eff}} = -\frac{1}{2}\mu_0 (M_S - H_K) M_S = -\frac{1}{2}\mu_0 M_S^2 + K_V + \frac{K_S}{t_{\text{Co}}}. \tag{3.10}$$

The first equality follows from the definition of M_{eff} and the last equality is obtained by splitting the anisotropy constant corresponding to H_K into a volume contribution K_V (as often found in polycrystalline Co layers[43]) and a surface contribution K_S. Note that from this definition follows that K_S is the total surface anisotropy, including contributions from both the top and the bottom interface. The first term on the right hand side represents the demagnetization energy of the film.

An example of how to extract K_S and K_V from equation 3.10 is shown in figure 3.3. According to the equation, the product $K_{\text{eff}} \cdot t_{\text{Co}}$ as a function of t_{Co} gives a straight line. The offset of the line corresponds to the surface anisotropy constant K_S, which in the figure is taken to be 1 mJ/m^2. The slope of the graph represents the sum of the demagnetization energy and the volume anisotropy K_V. Taking a saturation magnetization $M_S = 1.4 \cdot 10^6$ A/m (see appendix A) results in a demagnetization energy of $1.23 \cdot 10^6$ J/m^3. Subtracting this contribution from the slope gives K_V. For thin layers, interface anisotropy dominates and the film is out-of-plane magnetized, so $K_{\text{eff}} > 0$. Above a certain thickness, depending on the strength of K_S and K_V, the magnetization favors an in-plane magnetization. This transition from out-of-plane to in-plane

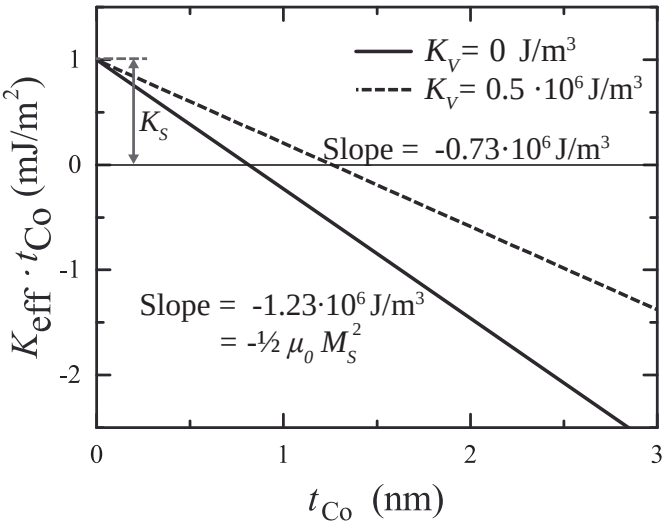

Figure 3.3: A plot of $K_{\text{eff}} \cdot t_{\text{Co}}$ versus t_{Co} for a film with and without volume anisotropy K_V. The offset of the graph gives the surface anisotropy constant K_S, here 1 mJ/m^2. The slope gives the sum of the demagnetization energy ($M_S = 1.4 \cdot 10^6$ for Co) and K_V.

magnetization occurs later if K_S is higher (larger offset) or K_V is higher (smaller slope).

Extracting damping

To extract the damping parameter α, the linewidth of equation 3.7 is determined for various applied frequencies f. Starting with the field-swept FMR linewidth ΔH, we can use its definition to obtain the relation

$$\Delta H(f) = \Delta H_0 + \frac{4\pi}{\mu_0 \gamma} \alpha f. \tag{3.11}$$

A constant offset ΔH_0 is included to account for extrinsic contributions to the FMR linewidth. It is commonly referred to as the inhomogeneous broadening term. It accounts for the fact that the sample is not perfectly uniform, and thus locally different resonance frequencies can occur, for example due to a different value for the anisotropy field H_{K}. Two-magnon scattering also depends on H and f, and can also contribute to ΔH_0.

For frequency swept FMR, it is often useful to convert the signal linewidth Δf into an equivalent field sweep linewidth ΔH. For small linewidths, we can use the

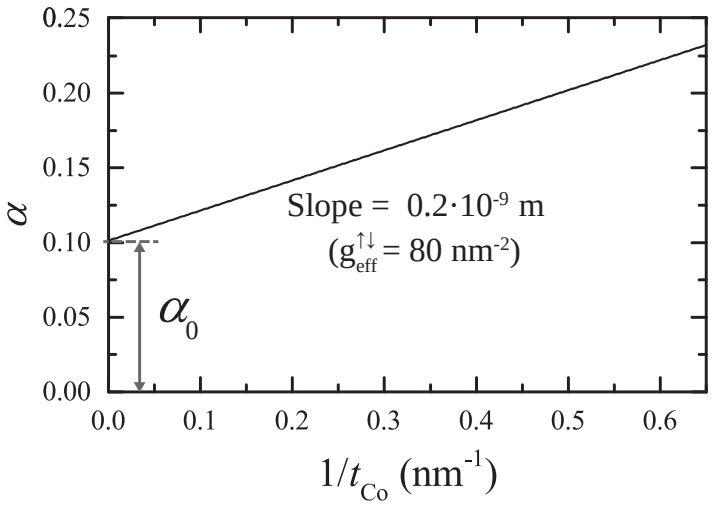

Figure 3.4: A plot of α versus the inverse cobalt thickness t_{Co}^{-1}. The offset of the graph corresponding to $t_{\text{Co}} \to \infty$ gives the bulk damping constant, here taken to be $\alpha_0 = 0.1$. Using magnetic parameters for bulk Co, $M_S = 1.4 \cdot 10^6$ A/m and $\gamma = 1.76 \cdot 10^{11}$ rad/sT, the effective spin mixing conductance $g_{\text{eff}}^{\uparrow\downarrow}$ can be determined from the slope.

relation[44]

$$\Delta H = \Delta f \frac{\partial H_{\text{res}}}{\partial f}\bigg|_{f=f_{\text{res}}} = \Delta f \frac{\sqrt{H(H+M_{\text{eff}})}}{\gamma\mu_0(2H+M_{\text{eff}})} = \frac{\Delta f f}{(\gamma\mu_0)^2(2H+M_{\text{eff}})}, \quad (3.12)$$

where we have again assumed that $\Delta H \ll H$.

To obtain the influence of spin pumping (section 2.2), we determine the magnitude of the effective spin mixing conductance $g_{\text{eff}}^{\uparrow\downarrow}$ of the interface. This can be obtained by measuring damping as a function of the Co thickness. From equation 2.13 we have

$$\alpha(t_{\text{Co}}) = \alpha_0 + \frac{\hbar\gamma}{2\pi M_S t_{\text{Co}}} g_{\text{eff}}^{\uparrow\downarrow} \quad (3.13)$$

The term α_0 corresponds to the bulk damping of Co. An example of how to extract the spin mixing conduntance and α_0 from this equation is shown in 3.4. The damping is plotted as a function of the inverse of the Co thickness, t_{Co}^{-1}. From equation 3.13 follows that the offset of this graph, corresponding to the case $t_{\text{Co}} \to \infty$, equals α_0. The slope of the graph is divided by a factor $\gamma\hbar/(2\pi M_s)$ to obtain the spin mixing conductance $g_{\text{eff}}^{\uparrow\downarrow}$.

Summarizing, the equations presented in this chapter allow us to extract the magnetic parameters γ, M_{eff} and α from χ. By varying the thickness of the ferromagnetic layer,

interface properties can be derived. In the following chapter we will present the setup developed during this thesis to extract χ experimentally and provide a way to verify the results of this new setup with other available experimental tools.

Chapter 4

Experimental tools

In this chapter the experimental tools are described that are used to extract the magnetic parameters arising from Co/Pt interfaces. First, an FMR setup including its measurement methods is described, which has been developed during the course of this thesis. This setup, based on a vector-network analyzer (VNA), has been used for pioneering experiments for the research department Physics of Nanostructures. Subsequently, an already existing anomalous hall magnetometry setup is described which is used to verify the results of the newly developed VNA-FMR setup. This chapter will be concluded with a detailed description of the investigated samples.

4.1 VNA-FMR

Ferromagnetic resonance (FMR) is a widely used method to study magnetic films. Measurements are generally fast, relatively easy to perform and give information about a wide range of magnetic properties. Various techniques exist to bring the magnetic system into resonance. Traditionally, FMR experiments involved the use of a microwave cavity, in which electromagnetic radiation with a fixed frequency ω probes the magnetization. The microwave losses are then measured as a function of the applied magnetic field, which relates to the magnetic response $\chi(H)$. Maximum absorption will occur once the magnetic precession frequency, given by the Kittel equation 3.9, matches the applied microwave frequency. However, microwave cavities often only support a limited amount of frequencies, depending on the shape of the cavity.

An improved method of FMR in the frequency domain makes use of a Vector Network Analyzer (VNA). This tool can both act as a broadband power source and detector of microwave and rf signals up to tens (or sometimes hundreds) of GHz. A coplanar waveguide (CPW) is used to inductively excite and detect spin waves in the sample. The VNA-FMR method has the additional advantage that it can also sweep the frequency of the applied current with high accuracy and speed, while the applied field is kept con-

stant. This is especially useful for experiments where the magnetic structure should be preserved during the measurement. Comparison between VNA-FMR and other types of FMR can be found in Kalarickal *et al.* [44].

The setup

In this study we are interested in all-electrical means of studying spin waves. Therefore, we have chosen for a setup with VNA as depicted in figure 4.1. The main components of the setup consist of a VNA, coaxial transmission cables, a CPW, a water-cooled electromagnet, a Gauss meter and an external PC to control the setup. An Analog-to-Digital Converter was used to trigger measurements with the PC. Using the analog input/output ports of the VNA allowed for a higher amount of measurements per second than other communication protocols like GPIB. The software controlling the setup has been designed from scratch to allow for both frequency and field swept FMR, as described in section 3.2. While more conventional VNA-FMR setups use two ports to perform measurements, in our setup only one port is used. The port simultaneously acts as a source and a detector. Only using one port improves the speed of the measurements significantly, without a loss in accuracy[45].

A side view of the setup between the poles of the magnet is also depicted in figure 4.1. High frequency probe tips mounted on a probe tip holder were used to contact the coaxial cables to the CPW. A microscope was used during the landing of the probe tips to prevent damaging of the tips. The CPW is placed on a translation stage that can be moved in the xy-plane. This allowed us to replace samples without physically moving the probe tip holders. Doing so ensures that the high frequency coaxial cables are displaced as little as possible between measurements, improving the signal to noise ratio. Both the probe tip holder and the sample containing the CPW are kept in place by creating a vacuum underneath the holders and sample. The metal frame that holds the electromagnet and the stages are placed on pieces of rubber to absorb vibrations from the environment.

Coplanar waveguide

At the heart of the setup, the coplanar waveguide (CPW) converts the current waves generated by the VNA to a perturbation field $\boldsymbol{H}_{\text{rf}}$. As shown in figure 4.2a, the CPW consists of three conducting strips lying in the same plane. The center conductor is called the signal line and the outer two conductors are called the ground lines. Each line generates an Oersted field. The sample is placed top down onto the CPW, such that the magnetic layer is in close proximity to $\boldsymbol{H}_{\text{rf}}$. The equilibrium magnetization $\boldsymbol{M}$ of the sample should be perpendicular to $\boldsymbol{H}_{\text{rf}}$ to be able to induce precession. The magnetization will then respond to $\boldsymbol{H}_{\text{rf}}$ according to the susceptibility χ of the sample, given by equation 3.7.

However, the CPW does not only excite spin waves, but also acts as a detector. As

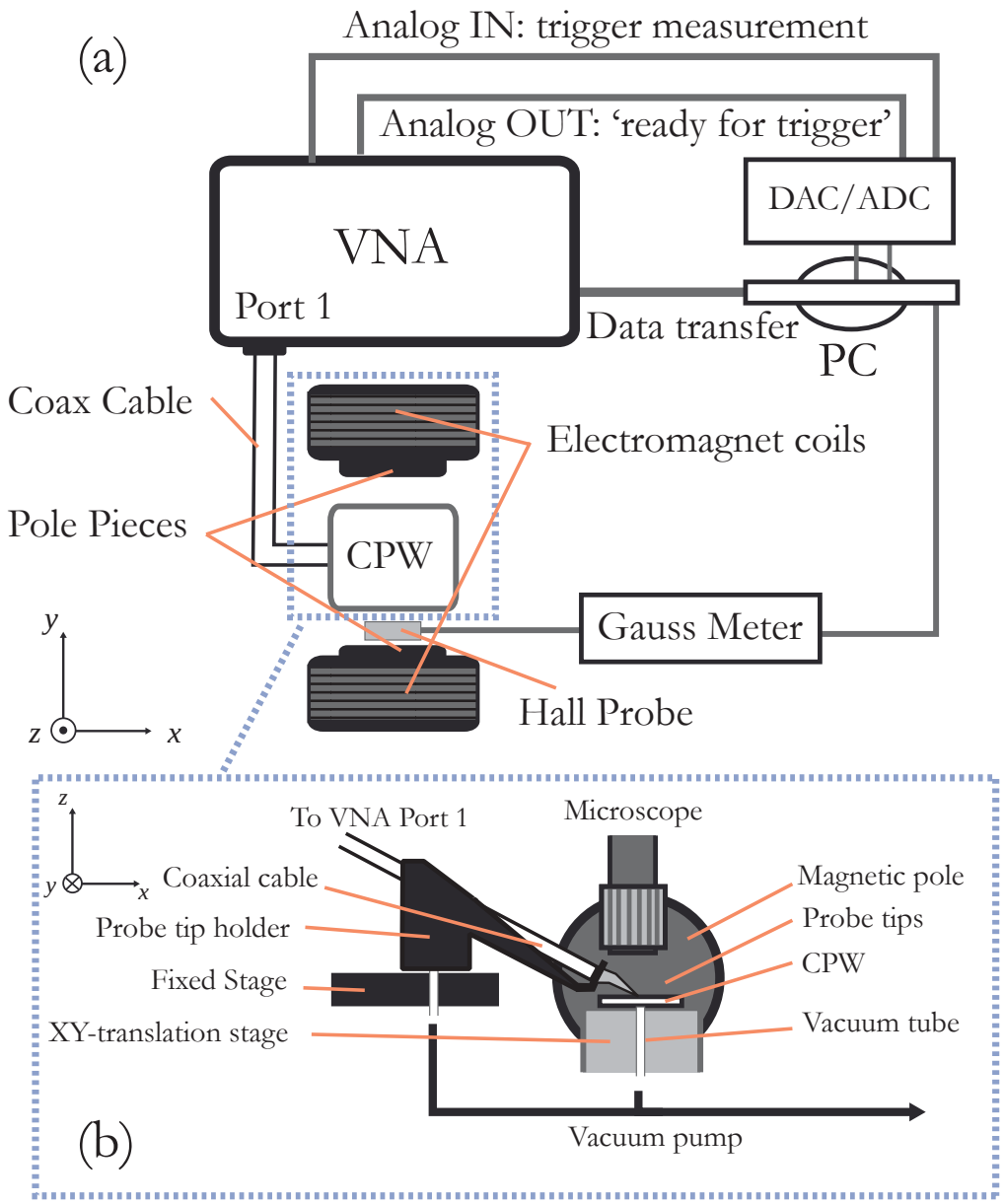

Figure 4.1: (a) Top view of the setup used for the VNA spin wave measurements. (b) Side view close-up of the setup between the poles of the magnet and the connection to the probe tip. A microscope is used to guide the landing of the probe tip.

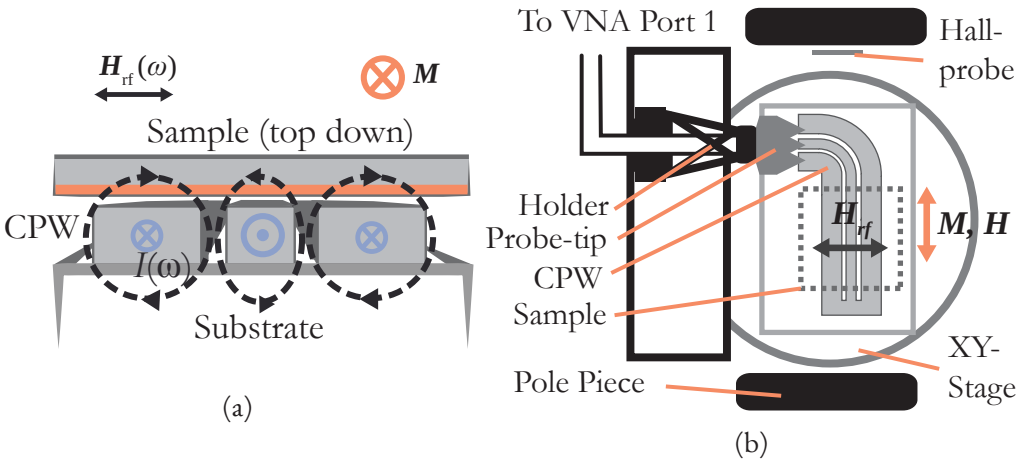

Figure 4.2: (a) A magnetic sample is placed top-down on the CPW (red line indicates the magnetic layer). An RF-current is applied to the CPW, generating the perturbation field $\boldsymbol{H}_{\text{rf}}$. (b) Top view of the CPW placed on the XY-translation stage. The pole pieces provide the magnetic field $\boldsymbol{H}$. The dotted line indicates the sample placement. The probe tip, mounted on its holder on a fixed stage (black rectangle), contacts the CPW from the side.

spin waves are excited, the precessing magnetization vector inductively generates an oppositely oriented current in the CPW. As we will discuss later in this chapter, a direct relation between the induced current and χ can be derived from which properties of the magnetic sample can be determined.

In figure 4.2b, a schematic depicton of the CPW used in this setup is shown. The CPW used in this thesis was fabricated using high-resolution electron beam lithography (more on this in part 2). Since the probe tips can only be contacted from the side, the CPW was designed to include a 90° bend such that the perturbation field is perpendicular to the field H, generated by the pole pieces at the top and bottom of the translation stage. For large rounded corners (radius $\sim$ 3 times the signal line width), the circuit behavior is nearly identical to a straight CPW[46] and therefore does not affect the performance negatively. The signal and ground lines are short-circuited at the end of the CPW, such that all power is reflected back to the VNA. A probe tip mounted on its holder is contacted to the signal and two ground lines for electrical contact to the VNA.

Vector Network Analyzer

In this research, a two-port vector network analyzer (Anritsu VectorStar MS4644B) is used to excite and detect spin waves inductively in the GHz (radio frequency, rf) regime. The VNA can measure both the phase and magnitude of a signal that is transmitted through and reflected from a device, generally called the device under test (DUT). Note

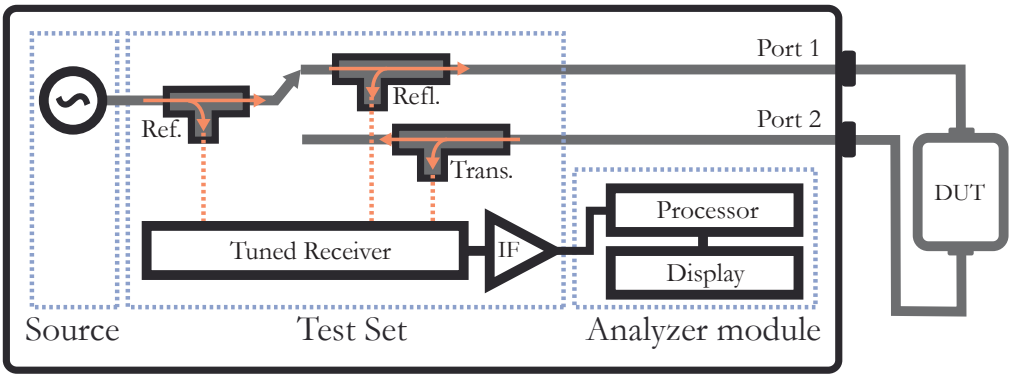

Figure 4.3: The rf-signal is generated in the source of the VNA. The test set taps some of the source signal as a reference, and couples the reflected and transmitted signals from the DUT to the receiver of the VNA. Here, the signal is also down converted to an IF. The analyzer module then processes the data and displays it on-screen.

that for the FMR setup described in the previous section, we disregard the second port of the VNA and only use the reflected signal at port 1 to extract data. However,for completeness we will discuss the full functionality of the VNA in this section, since in part 2 of this thesis both ports are used.

The VNA roughly consists of three main components, as depicted in figure 4.3. These are the source, the test set and the analyzer module. The source provides the radio frequency signal for the DUT. It can generate signals over a broad frequency range, in this case 10 MHz to 40 GHz. The test set module is also integrated in the VNA and has two main functions. Firstly, it taps a part of the source signal to use as a later reference signal. Secondly, it splits the signal incident at the input of the DUT and the reflected wave. Directional couplers or resistive bridges provide both functionalities. The test set module also downconverts the received rf signal to an intermediate frequency (IF), which can subsequently be processed and displayed on the VNA by the analyzer module. In the figure, port 1 is used as the source port, such that S_{11} and S_{21} are measured. A second measurement with port 2 as a source gives the remaining S-parameters.

In two-port experiments like in part 2 of this thesis, a connector is present on both ends of the DUT. It is possible to measure both the forward and the backward transmission and reflection. A convenient method for describing transmitted and reflected waves is the Scattering matrix, or S-matrix. It is defined in terms of incident and reflected voltage waves V^+ and V^- respectively, which are measured directly by the VNA. The various S-parameters and their relation to V^+ and v^- are shown in 4.4 for a two-port network. Note that S_{11} and S_{22} give information about the reflected signal on both ends of the DUT, and S_{21} and S_{12} about the forward and backward transmitted signal

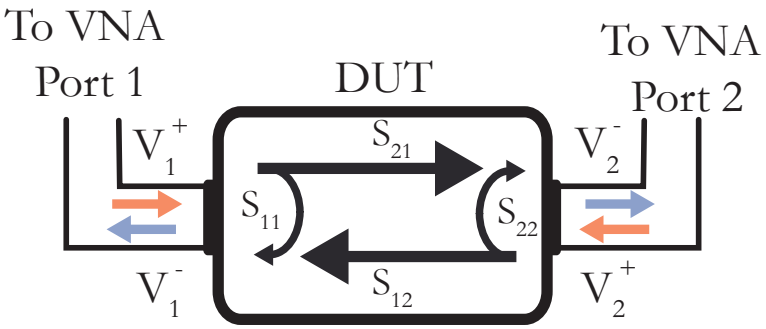

Figure 4.4: In a two-port network, the S-parameters of a Device Under Test (DUT) are defined based on the forward and backward traveling waves at each port. In the FMR measurements, port 2 is not connected and only S_{11} is used.

through the DUT. Mathematically, they are defined as

$$\begin{pmatrix} V_1^- \\ V_2^- \end{pmatrix} = \begin{pmatrix} S_{11} & S_{12} \\ S_{21} & S_{22} \end{pmatrix} \begin{pmatrix} V_1^+ \\ V_2^+ \end{pmatrix}, \tag{4.1}$$

where the second subscript of the matrix elements represent the port on which the signal enters the DUT, while the first subscript denotes the port of the signal leaving the DUT. In the case that only one port is used, like for the FMR experiments, the above equation reduces to

$$S_{11} = \frac{V_1^-}{V_1^+} \tag{4.2}$$

During a measurement, the S-parameters are often distorted by the presence of various error terms, like the finite directivity of the directional couplers or losses in the cables. Therefore, the setup should be carefully calibrated before starting a measurement. For the FMR experiments in this thesis, a Short-Open-Load (SOL) calibration method is used. A commercially available calibration substrate (GGB industries, model CS-5) is used for this. In the SOL method we first position the probe tip on patterned structures on the calibration kit. Then a frequency sweep is performed by the VNA. From the mismatch between the measured S-parameters on these structures and the expected behaviour (found in the calibration kit documentation), the VNA determines error coefficients that correct for the aforementioned error terms.

Relation between χ and the S-parameters

In FMR experiments we are interested in the magnetic response to an rf-field is given by the susceptibility χ. Since the VNA can only measure the S-parameters, we should

find a relationship between the S-parameters and χ. Various models exist that link the two parameters.

In 2008, Bilzer *et al.* [45] developed a model in which only one port of the VNA was used to extract χ instead of the more conventional two port measurements. Using only one port significantly increased measurement speed and calibration was significantly faster. By terminating the waveguide in an open-circuit, the signal containing information about the magnetic sample was reflected back to the excitation port.

The model first assumes that most of the reflected signal is originating from reflection at the open termination of the waveguide, such that

$$S_{11} \approx \exp(-2\gamma l_s), \tag{4.3}$$

in which l_s is the length of the waveguide, γ the propagation constant of the signal in the CPW. The factor 2 originates from the fact that the signal has to go both forward and back through the CPW. The propagation constant follows the relation

$$\gamma = i\frac{\omega}{c}\sqrt{\mu_r \epsilon_r}, \tag{4.4}$$

where ω is the angular frequency of the wave, c the speed of light and μ_r and ϵ_r the effective magnetic permeability and dielectric constant. The effective permeability is related to the susceptibility via the relation

$$\mu_r = 1 + x\chi, \tag{4.5}$$

where x is a filling factor, in the order 10^{-4}[45]. Combining equations 4.3-4.5 and taking a series expansion to first order in χ, we find an approximate susceptibility χ

$$\chi = \frac{c}{ixl_s\omega\sqrt{\varepsilon_r}}\left(1 - S_{11}\exp(i2l_S\omega\sqrt{\varepsilon_r}/c)\right) \propto S_{11}. \tag{4.6}$$

While the exact relationhip is rather complex, we are mainly interested in the fact that χ is, to first order, linearly proportional to S_{11}. The exact size of the prefactors and offset do not have to be considered directly, but can be bundled together as a scaling parameter. In the derivation, reflections at the input of the CPW have been neglected, which can cause additional distortions in the measurement, especially at lower frequencies. However, relative errors in the linewidth did not exceed 6% when compared to the results of a more elaborate two-port model[47].

Equation 4.6 will be used in this thesis to obtain χ from the measurement setup. In the following section we will provide a step-by-step procedure to extract the magnetic properties from χ, using the equations derived in the previous chapter.

FMR measurement procedure

To get a better understanding of the way an FMR measurement is performed, we will discuss the measurement procedure used to obtain the susceptibility χ of a thin magnetic film. We will also briefly describe the procedure used to obtain the gyromagnetic ratio γ, effective magnetization M_{eff} (and corresponding anisotropy constant K_{eff}), inhomogeneous broadening ΔH_0 and damping parameter α.

The goal of a single field-swept FMR measurement is to obtain a resonance field H_{res} and linewidth ΔH. From a set of measurements at different applied frequencies f, the aforementioned magnetic properties can be derived as described in section 3.2. However, the fitting procedure to obtain H_{res} and ΔH from a field sweep are not trivial. Also, for frequency swept FMR subtle differences exist to obtain the same magnetic properties, since now a resonance frequency f_{res} and linewidth Δf is found for various applied H. Therefore, both methods will be discussed in more detail in the remainder of this section. Since many different parameters are involved in the two methods and the details of the procedures are quite technical, a short summary of the fitting parameters obtained in each step of the fitting procedure is given in table 4.1 for clarity. Both methods are used later in this chapter to verify the setup by comparing the results of frequency and field swept FMR.

Measurement procedure for field swept FMR

After the magnetic sample has been placed on the coplanar waveguide, a field sweep can be performed. The PC controls the current source of the electromagnet, while reading out the Gauss meter at constant time intervals. Using the digital-analog converter, the PC simultaneously triggers the VNA to measure the S_{11} parameter. At the end of a sweep, the measured $S_{11}(H)$ are read out from the VNA and converted to a susceptibility $\chi(H)$ according to equation 4.6. The data can then be fitted to the analytical expression for the susceptibility. We rewrite equation 3.7 in terms of its fitting parameters, giving

$$\chi(H) = \frac{M_S(H + M_{\text{eff}})}{H(H + M_{\text{eff}}) - (H_{\text{eff}})^2 - i\frac{\Delta H}{2}(2H + M_{\text{eff}})}. \tag{4.7}$$

where $H_{\text{eff}} = \frac{2\pi f}{\gamma\mu_0}$. While ΔH can be directly used as a fitting parameter, a more elaborate method has to be used to obtain H_{res}. Note that we have dropped the imaginary term in the numerator, which is only valid if $\Delta H \ll H_{\text{res}}$. Subsequently, several offset and drift terms have to be included to account for background signals, giving

$$\chi_{\text{fit}}(H) = C_0 \left(A + d \cdot H + \chi(H) \exp(i\phi)\right), \tag{4.8}$$

The complex correction terms A and d are included to account for constant background signals and linear drift, caused by for example the probe tip contact. A phase correction

term ϕ is also added to account for the finite length of the CPW and C_0 is a scaling factor. From equations 4.7 and 4.8 we can now also see that it is impossible to obtain both M_S and H_K separately in these experiments, since the only factor M_S in the numerator of equation 4.7 cannot be fitted independently of C_0. However, it is possible to extract ΔH and H_{res} using the following method:

- First, γ is set to $1.76 \cdot 10^{11}$ rad/sT, corresponding to a g-factor $g = 2$, to calculate H_{eff}.
- The real and imaginary part of $\chi(H)$ are fitted simultaneously to equation 4.8 with a non-linear least squares method with M_{eff}, ΔH, complex correction factors C_0, A and d, and ϕ as fitting parameters (see step 1 in table 4.1).
- The resonance field H_{res} is determined with the Kittel equation 3.9 by filling in f and the obtained value for M_{eff} and using the same γ as in step 1 (see step 2 in table 4.1). Since this procedure of obtaining H_{res} is independent of which value for γ is used, we have no loss of generality in this procedure.

Repeating the above steps for various applied f, the real M_{eff} and γ can be determined by linearly fitting f^2/H_{res} versus H_{res}, conform to equation 3.9 (step 3 in table 4.1). To extract damping, ΔH is simply fitted to equation 3.11 for various f with ΔH_0 and α as fitting parameters, using the value for γ obtained from the fit to the Kittel equation (step 4 in table 4.1).

Measurement procedure for frequency swept FMR

For frequency-swept FMR, the measurement procedure is slightly different compared to field-swept FMR. The main difference arises from the fact that the components in the setup itself also exhibit frequency dependent behavior. Therefore, the measured signal does not purely originate from the magnetic response of the sample. An example is shown in figure 4.5 for an applied field $\mu_0 H = 150$ mT. While the resonance peak is visible, it is obscured by a large oscillating background signal. Therefore, an extra background measurement needs to be subtracted to negate the frequency dependent response of, for example, the coplanar waveguide and coaxial cables. This is done by applying a very large magnetic field ($\mu_0 H \approx 600$ mT), such that the resonance frequency of the magnetic film is larger than the measurement range of the VNA. The resulting signal contains all distortions in the setup to S_{11}, except for the resonance curve of χ. Therefore, after subtraction only the response of χ is remaining.

The data in a single measurement is then obtained as follows. First, the PC sets the applied magnetic field to the desired magnitude for the background measurement (600 mT in figure 4.5). Then, a single trigger is given to the VNA which then measures the background signal S_{11}^{BG} for a range of frequencies with intervals δf (typically several MHz). At the end of the sweep the data is read out by the PC. Then, the magnetic field is set to the desired measurement value (150 mT in figure 4.5) and the same sweep is

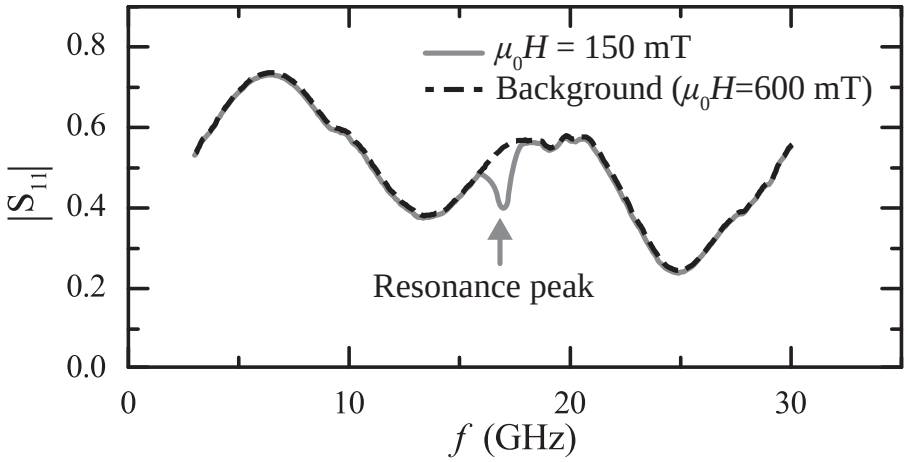

Figure 4.5: A frequency sweep measurement is distorted by frequency dependent background signals. To isolate the resonance peak, indicated by the arrow, a background measurement is subtracted. A large magnetic field $\mu_0 H = 600$ mT is applied, such that the resonance frequency of the film is outside of the measurement window. The resonance peak amplitude is exaggerated for clarity.

performed to measure the desired S_{11}. Then, the data is converted to a susceptibility χ using[45]

$$\chi(f) = \frac{\ln(S_{11}) - \ln\left(S_{11}^{\mathrm{BG}}\right)}{\ln\left(S_{11}^{\mathrm{BG}}\right)}. \tag{4.9}$$

This form of extracting χ is slightly more exact than equation 4.6. The original linear dependence can be obtained by taking a series expansion of $\ln(S_{11})$ around $S_{11} = 1$.

We can then fit the data to an analytical expression for $\chi(f)$. For frequency swept FMR, we use the linewidth Δf, giving a more simplified expression

$$\chi(f) = \frac{M_S f_{\mathrm{res}}^2 / H}{f_{\mathrm{res}}^2 - f^2 - i f \Delta f}, \tag{4.10}$$

with Δf and f_{res} as fitting parameters. We can obtain the original field-swept expression by filling in the Kittel equation 3.9 for the resonance frequency f_{res} and equation 3.12 for the linewidth. Like before, correction terms are added, such that

$$\chi_{\mathrm{fit}}(f) = C_0 \left(A + d \cdot f + \chi(f) \exp(i\phi)\right). \tag{4.11}$$

Contrary to field-swept FMR, we now fit f_{res} and Δf for various applied H (step 1 in table 4.1). Therefore, we can directly insert the fitting results into the Kittel equation and linearly fit f_{res}^2/H versus H to obtain M_{eff} and γ (step 2 in 4.1). To be able to extract damping, we first convert the linewidth Δf to an equivalent linewidth ΔH using

Table 4.1: Overview of the magnetic parameters and equations used in the fitting procedures for frequency and field swept FMR. In the second column the two magnetic parameters obtained from the fitting of χ are given. In subsequent columns, these parameters are used to eventually obtain M_{eff}, γ, α and ΔH_0. The parameter M^*_{eff} is the effective magnetization determined by setting $g = 2$.

		Field sweep		
Step #	1. Fit $\chi(H)$	2. Conversion	3. Fit Kittel eq.	4. Fit $\Delta H(f)$
Parameters	M^*_{eff}, ΔH	$M^*_{\text{eff}} \rightarrow H_{\text{res}}$	$H_{\text{res}} \rightarrow M_{\text{eff}}, \gamma$	$\Delta H, \gamma \rightarrow \alpha, \Delta H_0$
Eq. no.	4.8 ($g = 2$)	3.9 ($g = 2$)	3.9	3.11
		Frequency sweep		
Step #	1. Fit $\chi(f)$	2. Fit Kittel eq.	3. Conversion	4. Fit $\Delta H(f_{\text{res}})$
Parameters	f_{res}, Δf	$f_{\text{res}} \rightarrow M_{\text{eff}}, \gamma$	$\Delta f \rightarrow \Delta H$	$\Delta H, \gamma \rightarrow \alpha, \Delta H_0$
Eq. no.	4.11	3.9	3.9	3.11

equation 3.12 (step 3 in 4.1). Then we can again fit ΔH as a function of f_{res} to equation 3.11 to obtain α and ΔH_0 (step 4 in table 4.1).

The methods described above are used in the following section to verify the setup by comparing the results of frequency and field swept FMR.

Characterization of the setup

Various tests have been performed to investigate the validity of the used setup and equations. First, the magnetic field is determined at the sample position and compared to the magnetic field at the poles of the magnetic. A second hall probe, positioned at the center between the magnetic poles pieces, is used for this. The difference between the fields measured by the two hall probes are plotted in figure 4.6a. It shows a linearly proportionality between the applied field H and the discrepancy $H_{\text{pole}} - H_{\text{sample}}$. A linear fit shows that the discrepancy equals 2% of the applied field, meaning that 98% of the field lines at the pole reach the sample position. This is taken into account for the analysis in the results chapter.

Secondly, the magnetic response is measured without a sample placed on the CPW. As mentioned in the previous section, there should be no dependence of the background signal to the applied field. However, a magnetic background signal occurs with a relatively large amplitude of $\sim 10^{-3}$, which also depends on the applied frequency. The exact origin of this signal is unknown but is believed to originate from the coaxial cables physically responding to the magnetic field. Figure 4.6b shows that if the fitting range becomes in the range of hundreds of mT (for example for samples with very broad linewidths), there is a relatively strong non-linear background. Since the fitting

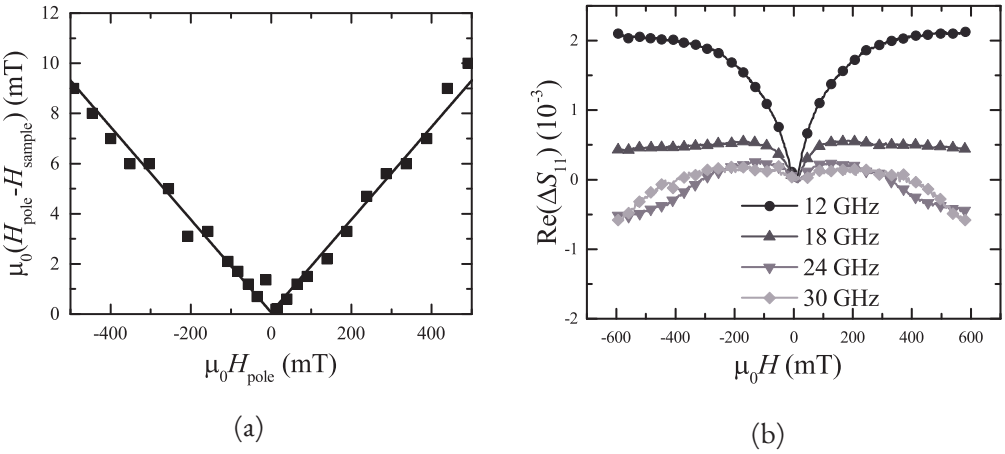

Figure 4.6: (a) The field at the sample position is compared to the field measured at the pole. The staight line indicates a linear fit. (b) The change in the real part of S_{11} as a function of the applied magnetic field H without magnetic sample.

procedure only takes into account a linear background, large linewidths can induce errors. However, as we will see in the results section the observed linewidths remain below 100 mT.

As a final test, the setup is tested for consistency between field swept and frequency swept FMR to investigate any systematic errors. A typical field-swept measurement for an applied frequency $f = 10$ GHz for a Ta/Co(10 nm)/Pt layer is shown in figure 4.7a. A frequency swept measurement at an applied field of 79 mT after background subtraction is shown in figure 4.7b. The fits, indicated by the solid lines, agree well with the measurement data. We see that, as expected, the signals are not exactly a symmetric and anti-symmetric Lorentzian function, but rather a linear combination of the two. For both measurements, the resonance field and linewidth were fitted with a relative standard deviation of less than 0.5% and 2% respectively.

Repeating the above measurements for various given applied frequencies (fields), we have determined the resonance field (frequency) using the procedure described in the previous section. In figure 4.8a the results are fitted to the Kittel equation for both field and frequency swept FMR to extract the parameters M_{eff} and γ. Results are in good agreement over the whole measurement range, so up to 400 mT and 25 GHz. The fitted linewidths ΔH are also plotted as a function of the resonance frequency in figure 4.8b (for the frequency sweep, the conversion $\Delta f \rightarrow \Delta H$ in equation 3.12 is used). For frequencies above 20 GHz, the frequency sweep performs worse in terms of fitting accuracy for the linewidth. This can be attributed to the fact that for high frequencies the setup is more susceptible to small changes in the setup, creating extra noise. Below 3 GHz we see additional deviations, which might be attributed to the fact

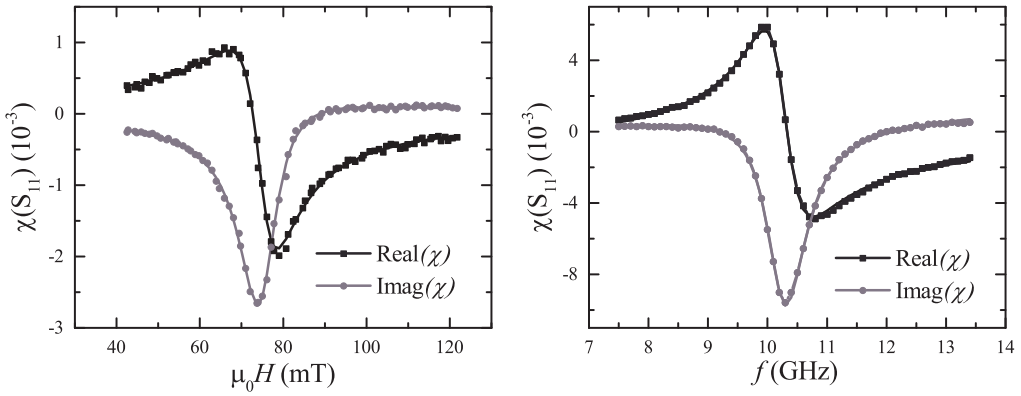

Figure 4.7: Typical measurement of the imaginary and real part of χ. This is done for (a) a field-sweep and (b) a frequency sweep. The fits to equations 4.8 and 4.11 are given by the solid lines. Graphs have been offseted to be centered around 0 for clarity.

Table 4.2: Magnetic properties obtained by FMR measurements of a Ta(4)/Co(10)/Pt(4) stack using the field-sweep and frequency-sweep approach.

Method	M_{eff} ($\times 10^6$ A/m)	g	α	$\mu_0 \Delta H$ (mT)
Field sweep	0.89 ± 0.01	2.40 ± 0.02	0.0167 ± 0.0003	1 ± 0.3
Freq. sweep	0.91 ± 0.01	2.38 ± 0.02	0.0170 ± 0.0003	0.2 ± 0.4

that our assumption that $\Delta H \ll H$ does not hold anymore.

The fitting results are compared in table 4.2. The obtained values correspond well with eachother within the given uncertainty interval. We find that the effective magnetization differs significantly from the saturation magnetization for bulk Co, $M_S = 1.4 \cdot 10^6$ A/m, implying a large anisotropy field in this stack. The g-factor is 10% higher than other typical values for Co/Pt multilayers, but have been reported earlier in polycrystalline Co layers[48]. The damping parameter also falls in the same order of magnitude as found in literature[48]. Further discussion on the magnitude of the magnetic parameters and the underlying physical mechanisms is subject of the results chapter of part 1. However, the main conclusion of these measurements is that they are consistent. Despite the aforementioned magnetic background signal, we are able to extract information about the magnetic layers due to the relatively small linewidth of the signals $\mu_0 \Delta H < 30$ mT.

Comparing the two methods, there are several advantages when using field-swept FMR. Firstly, there is no need for a background measurement in the field-sweep ap-

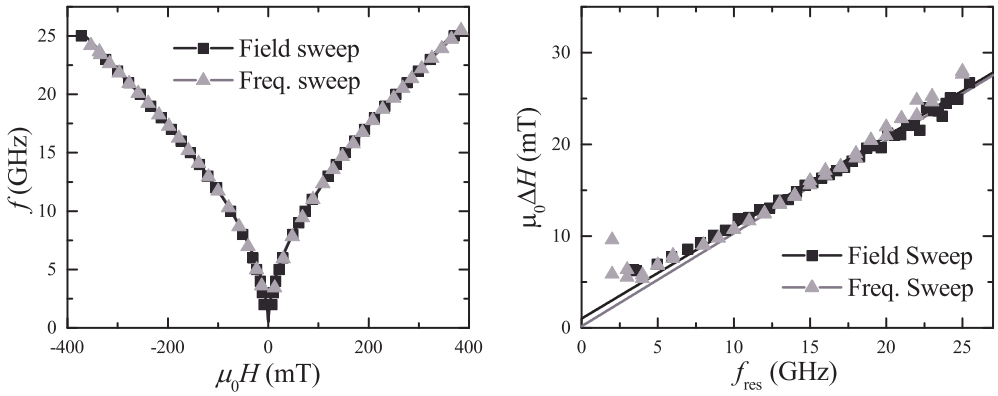

Figure 4.8: The Kittel equations (a) and the linewidths (b) for frequency sweep FMR and field sweep FMR. Solid lines indicate the fits.

proach (as discussed at the end of the previous section). Moreover, the field sweep approach has a better signal to noise ratio for frequencies $f > 20$ GHz. Therefore, for the FMR measurements in chapter 5, only the field sweep method has been used.

4.2 Anomalous hall effect magnetometry

To verify the results from the FMR measurements, we also use a second method to extract the interface anisotropy of the investigated samples. This method is based on the anomalous hall effect (AHE), which is a variation on the regular hall effect where a current in a magnetic field causes charge buildup transverse to the direction of the current. As shown in figure 4.9a, the anomalous hall effect differs in the sense that not an applied magnetic field, but the magnetization of the sample itself causes the charge buildup. The resulting voltage difference is proportional to the out of plane component of the magnetization, M_z. This allows us to measure M_z as a function of an applied field H of our samples. The loop can then be fitted to a Stoner-Wohlfarth model to extract the magnetic anisotropy of our samples[49].

In short, the Stoner-Wohlfarth model calculates the equilibrium magnetization of a magnetic particle with uniaxial anisotropy in an applied magnetic field. Consider a sample with an in-plane easy axis, as shown in figure 4.9b. By placing a sample under an angle φ in a magnetic field, the magnetization is pulled away from its easy axis. The strength of the magnetic response for increasing field strength is a measure for the anisotropy. The equilibrium direction of the magnetization can be calculated using the energy density of the system, which equals of a sum of the anisotropy energy and Zee-

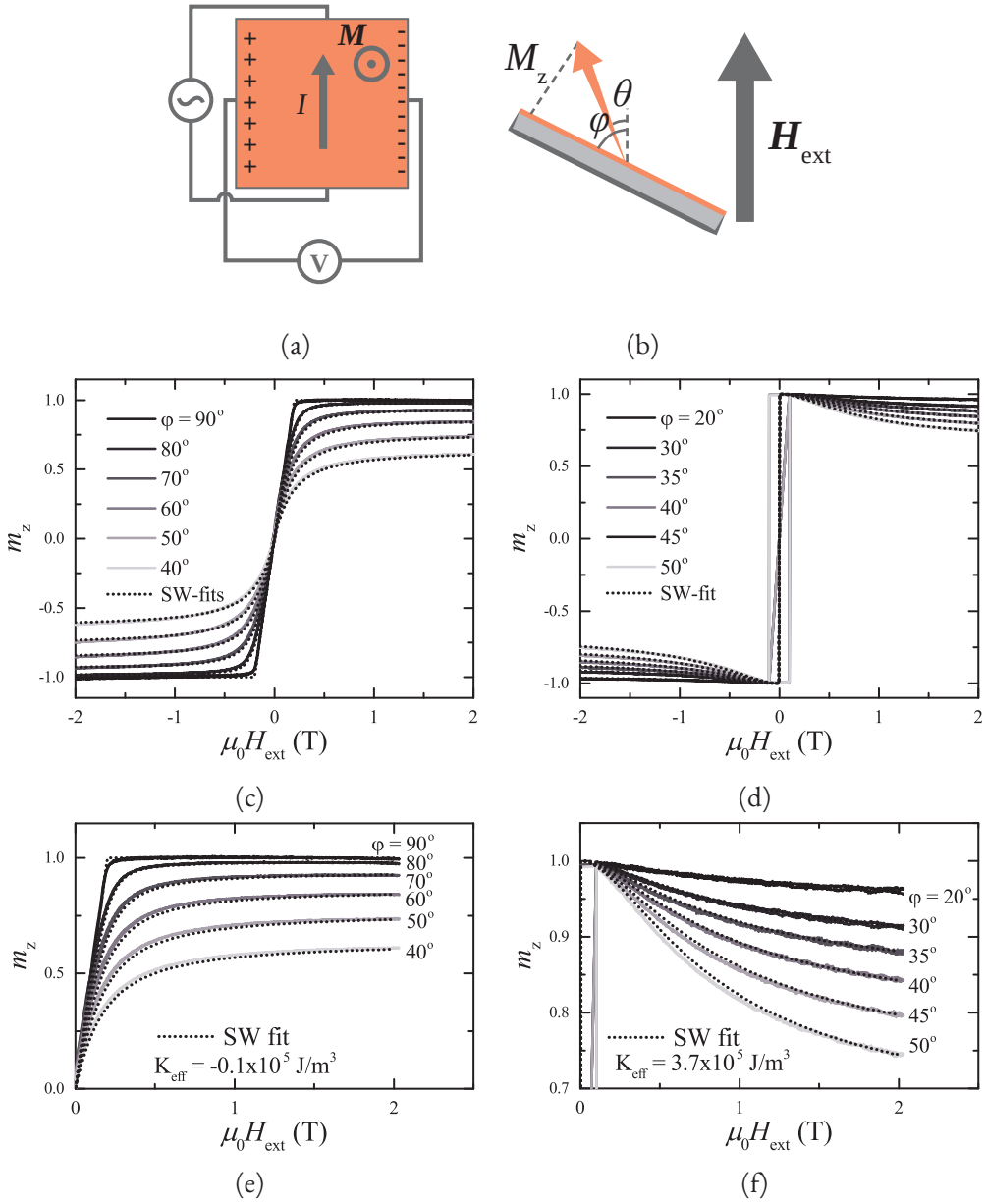

Figure 4.9: (a) Charge buildup in a magnetic material with out-of plane magnetization $\boldsymbol{M}$, transverse to a current I due to the anomalous hall effect. (b) The geometry of the Stoner-Wohlfarth model for a sample with in-plane anisotropy placed in a magnetic field H_{ext}. (c,d) Examples of hysteresis loop of the normalized $m_z \equiv M_z(H)/M_S$ for a sample with an in-plane (c) and an out-of-plane (d) easy axis for various angles φ. (e,f) Close-ups of the full loops. Dotted lines indicate fits to the Stoner-Wohlfarth model, and the resulting K_{eff} is given.

man energy

$$E = K_{\text{eff}} \sin^2(\varphi - \theta) + \mu_0 M_S H \cos(\theta), \tag{4.12}$$

where K_{eff} is again defined as $K_{\text{eff}} \equiv \frac{1}{2}\mu_0 M_{\text{eff}} M_S$, φ is the angle between the easy axis and the magnetic field and θ the angle between the magnetization and the applied field. Numerically minimizing the energy as a function of θ gives us the angle θ, and thus $M_z = M_S \sin(\varphi - \theta)$, for which the system is in equilibrium. Doing this for a whole range of magnetic fields results in a loop $M_z(H)$. This numerically obtained loop can be fitted to the data from the AHE with K_{eff} as fitting parameter.

In principle, K_{eff} can be obtained from a single $M_z(H)$ loop. However, to increase fitting accuracy various loops will be taken at different angles φ. The data obtained from these loops are simultaneously fitted to the Stoner-Wohlfarth model to obtain the fitting parameter K_{eff}. Two examples of a normalized $m_z(H)$ measurement of a Pt/Co/Pt sample, including fits to the Stoner-Wohlfarth model for different φ are shown in figures 4.9c and 4.9d. The easy axis of the samples are in the plane and out of the plane of the sample respectively. For the in-plane sample, $m_z = 0$ if no field is applied and the magnetization is pulled more out of plane for increasing fields. For out-of-plane measurements, the magnetization flips from -1 to $+1$ around $H = 0$. It is then gradually pulled towards an angle θ due to the increasing Zeeman energy.

A close-up of both loops and their corresponding fits is shown in figures 4.9e and 4.9f. The obtained anisotropies for both samples are also given in the figure. When the sample is positioned such that the sample is close to being parallel to H, the fit starts to deviate from the experimental data. This could be a result of additional energy terms or non-coherent rotation which have been neglected in the Stoner-Wohlfarth model. Therefore, only angles φ have been used such that H makes an angle of at least $40°$ with the plane of the film (meaning $\varphi > 40°$ for in-plane magnetized samples and $\varphi < 50°$ for out-of-plane magnetized samples).

4.3 Sample design

For this chapter, full sheet samples are created using magnetron sputter deposition. This is a form of physical vapor deposition in which ions of an argon plasma are used to eject atoms from a target material onto the substrate, forming a thin film of (magnetic) material. Typical deposition rates are 1 Å/s or less.

Various samples are made to investigate physical mechanisms at the Co/Pt interface. First, the properties of a Co film with thickness t_{Co}, sandwiched between two Pt layers is studied. A 4 nm Ta seed layer is used to stimulate growth of Pt with a 111 crystallographic texture, which is known to have high interface anisotropy in contact with Co[50, 51]. Therefore, the total stack is Ta(4)/Pt(4)/Co(t_{Co})/Pt(4). The layers are grown on thermally oxidized Si substrates, approximately 0.5×0.5 cm^2 in size. This will be referred to as the Pt/Co/Pt stack.

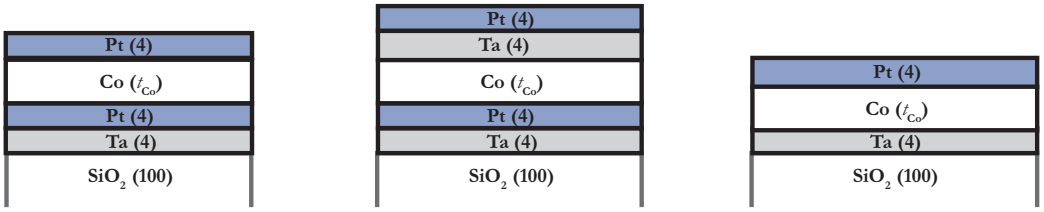

Figure 4.10: The stacks in this research, referred to as Pt/Co/Pt, Pt/Co/Ta and Ta/Co/Pt, respectively. The layer thicknesses in the parentheses are given in nm.

To distinguish between the quality of the bottom and top layer, one Co/Pt interface is replaced by a Co/Ta interface. The Co/Ta interface generally has a negligible contribution to the surface anisotropy. The two additional stacks studied are therefore Ta(4)/Co(t_{Co})/Pt(4) and Ta(4)/Pt(4)/Co(t_{Co})/Ta(4)/Pt(4). The top Pt layer in the latter stack is used to prevent oxidation of the Ta top layer. These stacks will be referred to as the Ta/Co/Pt and the Pt/Co/Ta stack.

Chapter 5

Results and discussion

Using field-swept FMR, the anisotropy, g-factor and damping have been determined for various Co/Pt sandwiches. As an extra verification of the FMR results, the anisotropy constants are also determined using the anomalous hall effect (AHE) setup described in section 4.2. From these quantities, the anisotropy and spin pumping contributions of the Co/Pt interface are calculated. The chapter will be concluded with a discussion on the assumptions made during the analysis and provide suggestions for improving the developed setup.

5.1 Surface anisotropy of Co/Pt sandwiches

Using the method described in section 3.2, the interface anisotropy K_S and volume anisotropy K_V of the fabricated stacks is investigated by measuring the anisotropy constant K_{eff} for various Co thicknesses. Since the anisotropy constant is defined as $K_{\text{eff}} \equiv -\frac{1}{2}\mu_0 M_{\text{eff}} M_S$, two separate quantities have to be measured. The effective magnetization M_{eff} follows from the FMR measurements, while M_S is determined independently in appendix A. The results for the three different Co/Pt stacks will be discussed separately below. A summary for each stack including fitting uncertainties can be found in table 5.1. The obtained gyromagnetic ratio (and thus g-factor) seemed to have no significant thickness dependence, so for each stack the average value is also given.

Pt/Co/Pt

First, the anisotropy of the Pt/Co/Pt stack is investigated. For various applied frequencies f the obtained resonance fields H_{res} are determined using the procedure as described in section 4. In figure 5.1a, the obtained data is shown for various Co thicknesses t_{Co}. The data is fitted to the Kittel equation, from which the effective magnetization M_{eff} and gyromagnetic ratio γ are determined. The average γ corresponded to

Table 5.1: Magnetic parameter values of various stacks obtained from the FMR measurements and the comparison to anomalous hall effect (AHE) measurements (given in square brackets). [1]Magnetic dead layer was determined with SQUID-VSM (Appendix A). [2]The g-factor is determined from fitting parameter γ (section 2.2). [3]For Pt/Co/Ta, no uncertainties could be extracted for the anisotropy since only two data points were used for fitting.

Stack	K_S (mJ/m^2) $[K_S^{\mathrm{AHE}}]$	K_V (MJ/m^3) $[K_V^{\mathrm{AHE}}]$	$t_{\mathrm{dead}}^{[1]}$ (nm)	g-factor[2]
Pt/Co/Pt	1.9 ± 0.1 $[2.1 \pm 0.1]$	0.29 ± 0.02 $[0.22 \pm 0.05]$	0.0 ± 0.05	2.19 ± 0.01
Pt/Co/Ta[3]	1.2 $[1.2 \pm 0.1]$	0.36 $[0.34 \pm 0.02]$	0.45 ± 0.05	2.18 ± 0.01
Ta/Co/Pt	1.8 ± 0.1 $[1.5 \pm 0.3]$	0.05 ± 0.02 $[0.8 \pm 0.05]$	0.0 ± 0.05	2.20 ± 0.01

a g-factor $g = 2.19$, which agrees well with literature. Typical reported values for g in fcc and hcp Co lie in the range 2.09-2.20[48, 52–54].

To extract the interface anisotropy constant K_S, the product $t_{\mathrm{Co}} \times K_{\mathrm{eff}}$ as a function of the thickness (eq. 3.10) is plotted in figure 5.1b. From the slope we find a volume anisotropy $K_V = 0.29 \cdot 10^6$ J/m^3 and from the offset $K_{S,\mathrm{tot}} = 1.9$ mJ/m^2. These values correspond well with the results from the AHE measurements, where we find a the volume contribution equal to $K_V^{\mathrm{AHE}} = 0.22 \cdot 10^6$ J/m^3 and surface anisotropy $K_{S,\mathrm{tot}}^{\mathrm{AHE}} = 2.1$ mJ/m^2.

Assuming equal contributions from the top and bottom interface, we find that for a single Co/Pt interface, $K_S = 0.9 \pm 0.1$ mJ/m^2. In literature, the anisotropy of Co/Pt interfaces strongly varies, depending on the type of substrate and buffer layer that is used[55]. Especially on oxidized SiO_2 the anisotropy is found to be strongly influenced by the quality of the substrate[43]. In systems where a Ta buffer was inserted under the Pt/Co interface, the surface anisotropy was increased up to a factor of two compared to when no buffer layer was used, resulting in similar values as found in our experiments[56, 57].

Regarding the bulk anisotropy K_V, there is little consensus in literature about its magnitude. Values as low as $0.02 \cdot 10^6$ J/m^3 have been reported for fcc Co and values as high as $0.5 \cdot 10^6$ J/m^3 for hcp Co[43]. This indicates that our stacks could be a mixture of a hcp and fcc Co texture. For optimal results in part 2 of this thesis an fcc texture is favored, since it is predicted to induce higher spin orbit coupling and DMI near Co/Pt interface[58]. However, the observations for the bulk anisotropy can be explained without the hcp phase as well. Some argue that for fcc textures the demagnetization energy is lowered[59]. Using a saturation magnetization $M_S = 1.24 \cdot 10^6$ A/m and no addi-

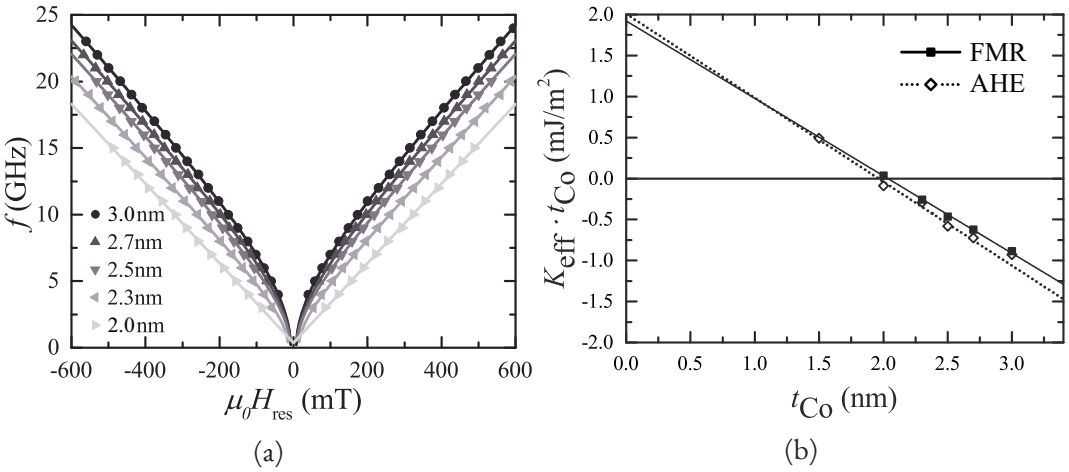

Figure 5.1: a) For various applied frequencies the positive and negative resonance fields are plotted for Pt/Co(t_{Co})/Pt. Graphs are shown for various t_{Co}. Solid lines represent fits to the Kittel equation. (b) The results for K_{eff} for each t_{Co} obtained from figure (a) are shown and compared to the results from the AHE measurements.

tional volume anisotropy results in a slope $-\frac{1}{2}\mu_0 M_S^2 = -0.94 \cdot 10^6$ J/m^3, identical to the line in figure 5.1b. However, magnetometry measurements show that for our samples M_S is in fact closer to bulk Co ($M_S = 1.4 \cdot 10^6$ A/m, appendix A), implying that there is a volume anisotropy present. Some also argue that even without the hcp phase, increased strain at the bottom interface can also induce extra out-of-plane anisotropy in the bulk for ultra-thin layers[43].

Pt/Co/Ta and Ta/Co/Pt

For Pt/Co/Ta, again the effective magnetization has been determined for various t_{Co}. Unfortunately, all samples grown with a thickness below $t_{\text{Co}} = 1.7$ nm have an out-of-plane easy-axis. Since the magnetic field in the FMR setup is not strong enough to pull the magnetization in-plane, only two samples could be measured with the FMR setup. This transition thickness from in-plane to out-of plane is surprisingly close to that of Pt/Co/Pt. This can explained by the fact that intermixing of Ta with Co induces a magnetic dead layer, such that the effective magnetic layer thickness is reduced. To investigate this, magnetometry measurements have been performed as described in Appendix A. Indeed, the presence of a large magnetic dead layer with thickness $t_{\text{dead}} = 0.45$ nm was found in Pt/Co/Ta. A corrected layer thickness $t^*_{\text{Co}} = t_{\text{Co}} - t_{\text{dead}}$ is therefore used to calculate the magnetic parameters.

The obtained experimental results are shown in figure 5.2a. We find from the offset

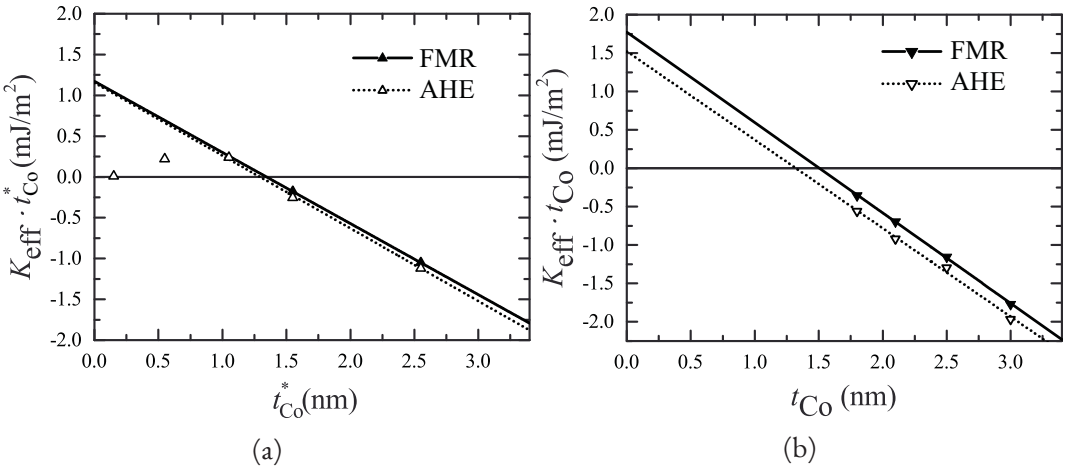

Figure 5.2: The product $K_{\text{eff}} \cdot t_{\text{Co}}$ is shown for (a) Pt/Co/Ta and (b) Ta/Co/Pt. Results are compared to fits from the AHE measurements.

of the graph that $K_S = 1.2$ mJ/m^2 and from the slope $K_V = 0.36 \cdot 10^6$ J/m^3. These values correspond well with the results of the AHE measurements, where $K_S^{\text{AHE}} = 1.2$ mJ/m^2 and $K_V^{\text{AHE}} = 0.34 \cdot 10^6$ J/m^3. Note that for effecitive thicknesses smaller than 1 nm, the anisotropy constant deviates from its expected $1/t$ behavior. This is a well-known observation in ultrathin films and have been argued to originate from increased surface roughness due to for example island-like growth of Co[60], interdiffusion or a decrease in the Curie temperature[61]. Therefore, these data points have been omitted from the linear fit for the AHE measurements.

For Ta/Co/Pt, no magnetic dead layer was found. A surface anisotropy of $K_S = 1.8$ mJ/m^2 was found and $K_V = 0.05 \cdot 10^6$ J/m^3. The large value for K_S indicates either an enhanced contribution from top Co/Pt interface compared to the other two stacks, or an extra contribution from the bottom Ta interface. The volume anisotropy is significantly quenched, which could mean that there is no strain at the bottom interface or, since an entirely different seed layer is used for Co, the growth texture might also have been altered altogether. The AHE measurements again give similar results of $K_S^{\text{AHE}} = 1.5$ mJ/m^2 and $K_V^{\text{AHE}} = 0.13 \cdot 10^6$ J/m^3.

In conclusion, when we combine the results from the Pt/Co/Pt and Pt/Co/Ta stack, and assume a negligible contribution from the top Ta interface, we can conclude that for the platinum interface $K_{S,\text{bot}} = 1.2$ and $K_{S,\text{top}} = 0.7$. However, care must be taken since the top Ta layer significantly influences the magnetic layer, as indicated by the large magnetic dead layer in these stacks. As for the Ta/Co/Pt stack, no unambiguous results can be drawn, since the growth texture could be entirely different for Ta/Co/Pt. Therefore, we cannot assume that the top Pt interface gives the same contribution as for a Pt/Co/Pt stack.

Table 5.2: Magnetic parameter values of various stacks. [1]For Pt/Co/Ta, no uncertainties could be extracted since only two data points were used for fitting.

Stack	α_0	$g_{\text{eff}}^{\uparrow\downarrow}$ (nm^{-2})
Pt/Co/Pt	0.005 ± 0.003	43 ± 4
Pt/Co/Ta[1]	0.007	21
Ta/Co/Pt	0.007 ± 0.006	40 ± 4

5.2 Spin pumping in Co/Pt sandwiches

Besides anisotropy, the damping parameter α also gives us important information about Co/Pt interfaces. The effective spin mixing conductance gives information on the transparency of the Co/Pt interface to spin currents. The same stacks as in the previous section have been investigated and results are summarized in table 5.2.

By plotting the linewidth of a field sweep measurement as a function of the applied frequency, we can extract α with equation 3.11. In figure 5.3a, the results are shown for Pt/Co/Pt for various t_{Co}. As expected, we observe a linear dependence of ΔH on f. The slope of the graphs seems to be increasing for smaller t_{Co}. For all t_{Co}, an offset linewidth $\mu_0 \Delta H_0$ in the range 10-17 mT is found. This is significantly larger than the $t_{\text{Co}} = 10$ nm thick stacks used to verify the setup in section 4.1. This can be explained using the fact that local variations in for example interface anisotropy have a larger effect for thinner films. We also observe that there is a larger spread around the fitted line for higher f. Like discussed in section 4.1, this originates from the fact that in this region both the non-linear background and noise are increased.

However, we are still able to relatively accurately fit the data and obtain α. By plotting the damping parameter as a function of the reciprocal Co thickness (figure 5.3b), we see a clear linear dependence, as is expected from equation 3.13. We find from the offset of the graph that $\alpha_0 = (0.005 \pm 0.003)$ and from the slope that $g_{\text{eff}}^{\uparrow\downarrow} = (43 \pm 4)\ \text{nm}^{-2}$. The value for α_0 is consistent with the damping for fcc(111) Co found in literature, although reported values for hcp(0001) Co also fall within the given uncertainty[59]. Assuming equal contributions from both interfaces for the spin mixing conductance, we find that per interface $g_{\text{eff}}^{\uparrow\downarrow} \approx (22 \pm 4)\ \text{nm}^{-2}$. In literature, reported values for single Pt/Co interfaces range from $g_{\text{eff}}^{\uparrow\downarrow} = 40\text{-}80\ \text{nm}^{-2}$[62, 63].

For Pt/Co/Ta, again only two data points could be used. We find that $\alpha_0 = 0.007$ and $g_{\text{eff}}^{\uparrow\downarrow} = 21\ \text{nm}^{-2}$. One might be skeptical about the significance of this fit, since the amount of data points is so limited. However, we argue that α_0, inherently a bulk property, is not affected by the top layer. If this is the case, then the almost factor 2 difference between the total damping parameter α in Pt/Co/Pt and Pt/Co/Ta can be directly related to damping effects originating from the top interface. We conclude that

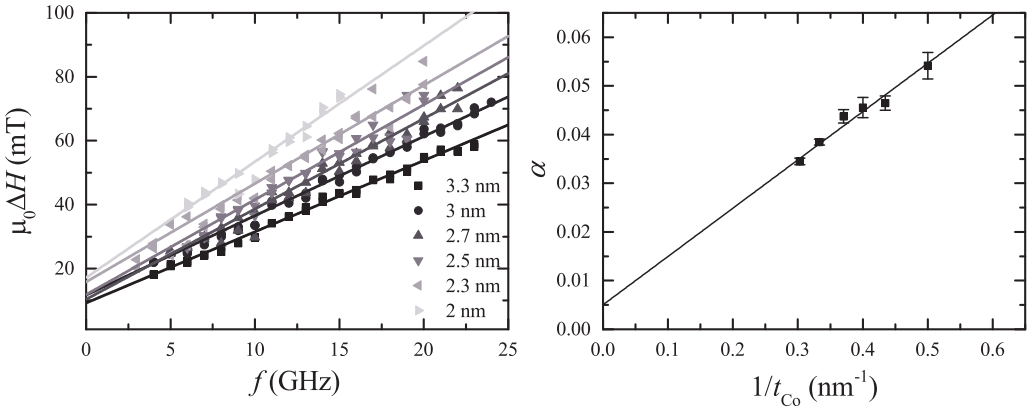

Figure 5.3: a) The linewidth $\mu_0\Delta H$ is plotted as a function of f for various t_{Co}. From the slope we extract α. (b) The damping α as a function of the reciprocal thickness, showing linear dependence. The solid line is a linear fit, from which we find that $\alpha_0 = 0.005$ and $g_{\mathrm{eff}}^{\uparrow\downarrow} = 43 \pm 4\,\mathrm{nm}^{-2}$.

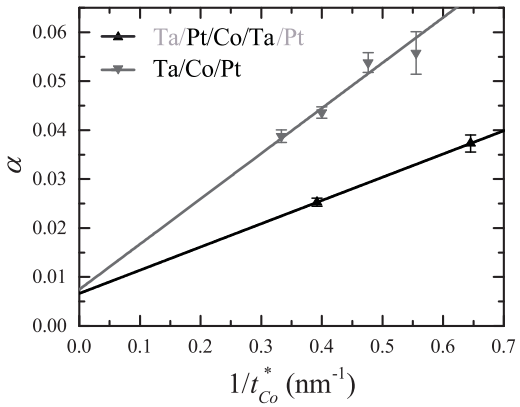

Figure 5.4: The damping parameter α as a function of the reciprocal thickness. The offset shows similar bulk damping values, while the slope indicates a much higher spin mixing conductance in Ta/Co/Pt stacks.

the top Ta interface is practically impenetrable for spin currents.

For Ta/Co/Pt we find that $\alpha_0 = (0.007 \pm 0.006)$ and $g_{\uparrow\downarrow} = (40 \pm 4)$ nm^{-2}, similar to the Pt/Co/Pt stack. Spin mixing could be enhanced at the top Pt layer due to the different growth of Co on a Ta seed layer. However, if this is not the case, we must conclude that the bottom Ta interface is also contributing to the spin mixing conductance.

In conclusion we can state that the $1/t$ dependence of the damping parameter indicates that spin currents are indeed emitted from the Co layer. For Pt/Co/Ta, the spin mixing is halved compared to Pt/Co/Pt, indicating that the top Ta layer is not likely to contribute to spin pumping. Furthermore, in Ta/Co/Pt the values obtained for spin mixing conductance has values much closer to the values obtained for Pt/Co/Pt than would intuitively be expected. This trend was also observed for the surface anisotropy K_S. However, why these spin-orbit coupling related phenomena are almost equal in magnitude for these two stacks could not be explained with the measurements.

5.3 Additional remarks

In conclusion, we can say that the FMR setup developed during this thesis allows for accurate measurements of the magnetic properties of ultra-thin ferromagnetic layers with thicknesses down to 1.5 nm. The Co/Pt interface is shown to induce large anisotropy at the interface, and also in the bulk when Pt is used as seed layer. The Co/Pt interface also significantly enhances damping, which can be explained with the spin-pumping mechanism. Results agreed well with literature and also with other methods of extracting the anisotropy (anomalous hall effect experiments).

Note however that in our analysis we have ignored extrinsic contributions to the linewidth other than spin pumping. In the in-plane geometry used in our setup, scattering of the FMR mode into finite wavelength spin waves (two-magnon scattering) is known to significantly influence the FMR linewidth. The contribution of this process can be studied by performing angle-dependent measurements of the FMR signal. Unfortunately, again due to geometrical restrictions in our setup, we are not able to rotate the field in an out-of-plane direction. For Co/Pt multilayers it is found that two-magnon scattering can contribute up to approximately 20% of the total linewidth[53]. While this percentage is indeed significant, it does not make two-magnon scattering the dominant contribution to the total linewidth. Further research in the perpendicular geometry could shed light on the magnitude of this contribution.

To further improve the FMR setup and measure smaller signals (thinner layers, lower M_S), several complications need to be dealt with. The largest problem originates from non-linear background effects in our setup. For certain frequencies there is strong non-linear behavior of the background signal, which is difficult to subtract. This results in distorted linewidths for the fitted signals, especially for samples with large linewidths

due to for example high damping. The non-linear background also appears in roughly the same shape when the probe tips are not contacted to the substrate, but hanging in air. This leads us to believe that these signals arise from physical displacement of the coaxial cable near its connection to the probe tips. For field-swept FMR, performing a reference measurement without sample could resolve a large part of this problem, at the expense of having a longer measurement time.

Minor other distortions in the measurement signal originate from calibration errors in the setup. This causes additional signal loss or increased noise. For example, the Short-Open-Load calibration procedure does not hold into account that the probe tips are placed onto a substrate with a different dielectric constant than the calibration substrate. Also, after loading the sample onto the waveguide, the presence of the sample itself can introduce additional reflection peaks in the measured S-parameters as well. To account for this flawed de-embedding process, a background measurement can be performed of a waveguide loaded with a non-magnetic substrate. By either dividing the real FMR data by this background signal or performing other more complex correction calculations[64], one can reduce the variation in the observed linewidths significantly. However, this mainly affects measurements near resonance frequencies of the waveguide itself, which are not abundantly present due to our waveguide design.

Finally, a last method of dealing with unwanted background signals, is proposed by Sievers *et al.* [65]. An extra reference path is added for the electrical signal, identical to the measurement path, but without sample. This interferometric approach significantly reduces the background signal and can increase sensitivity up to two orders of magnitude in optimal conditions.

With these final notes we conclude part 1 of this thesis. The developed FMR setup and the gained insights on the Co/Pt interface can now be used as a solid foundation for measuring propagating spin waves. More specifically, the asymmetry of counter-propagating spin waves due to interface DMI will be subject of in part 2 of this thesis.

Part II

All-electrical non-reciprocal spin wave spectroscopy

In part 2, the setup and results from part 1 will be used to investigate the non-reciprocal properties of propagating spin waves in thin ferromagnetic strips. The non-reciprocal spin wave behavior is directly related to the strength and sign of the interfacial Dzyaloshinskii-Moriya Interaction (i-DMI) in this system. Many new technological applications can benefit from this interaction, since it stabilizes chiral magnetic textures that can improve device functionality (higher domain wall velocities[11, 12], skyrmion stabilization[13]) and open up paths towards data transport and manipulation (spin wave logic[66]).

We will first discuss the theoretical behavior of propagating spin waves in the presence of i-DMI. The experimental setup is also described and an analytical model is introduced which helps to explain the contribution of various physical mechanisms in the observed signals. We will then address the measurements regarding the excitation and asymmetric propagation of surface spin waves in the presence of i-DMI. We will conclude this thesis by proposing several modifications to the used setup which could benefit future research.

Chapter 6

Theory of asymmetric spin wave propagation

Up until now we have only considered uniform precession of the magnetization, corresponding to a spin wave with infinite wavelength or, equivalently, a wave number $k = 0$. We will now consider the case where the excited spin waves have non-zero wave numbers. We will focus on magnetostatic spin waves, which means that the exchange energy in these spin waves can be ignored. This approximation holds for spin waves where the product $k\lambda_{ex} \ll 1$, where λ_{ex} is the exchange length of the magnetic material, which for the Co films used in this thesis approximately equals $\lambda_{ex} \approx 10$ nm[67]. The behavior of magnetostatic spin waves strongly depends on the used geometry. For some geometries it is found that after excitation, the spin waves traveling in opposite directions behave strongly asymmetric[25, 26, 30, 56, 68].

To investigate the asymmetric propagation of spin waves, we consider a sample lying in the xy-plane. As depicted by the side view of figure 6.1, the externally applied magnetic field and equilibrium magnetization are in the plane of the sample ($\pm y$-direction), perpendicular to the wave vector k ($\pm x$-direction). In this geometry, we excite Magne-

Figure 6.1: Side view of surface waves in a thin film, traveling perpendicular to the applied field $\boldsymbol{H}_{ext}$. Blue and red regions represent the spin wave amplitude along the thickness of the film for waves traveling in the positive and negative x-direction, respectively.

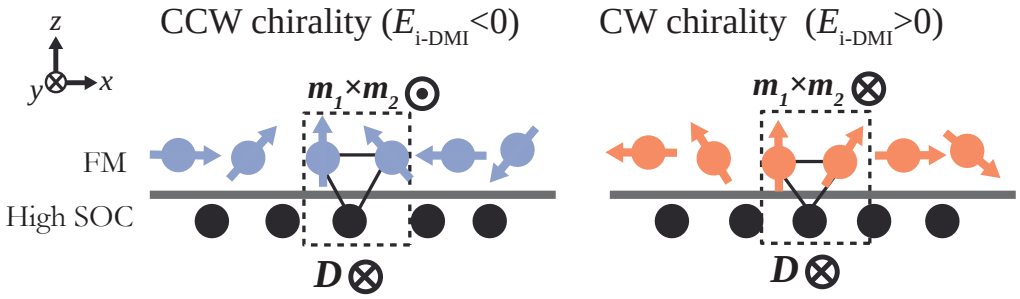

Figure 6.2: The i-DMI energy $E_{\text{i-DMI}}$ of a spin wave is determined by the sign of $\boldsymbol{D}$ and the cross product of neighbouring spins $\boldsymbol{m}_1 \times \boldsymbol{m}_2$. The direction of $\boldsymbol{D}$ is fixed by the relative position of the spins and high spin orbit coupling (SOC) atom, parallel to the normal of the triangle in the figure. Spin waves with counterclockwise (CCW) and clockwise (CW) chirality, indicated by blue and red spins, respectively, therefore have opposite $E_{\text{i-DMI}}$.

toStatic Surface Waves (MSSW), which can exhibit strong asymmetry for oppositely traveling spin waves. Its name originates from the fact that the amplitude of these spin waves, depending on the sign of k, is larger near either the top or the bottom surface of the film. The localization has some interesting consequences, which will be addressed later in this chapter. The MSSW mode is particularly useful for investigating i-DMI, because its symmetry allows the frequency of propagating waves to be affected by i-DMI. The various properties of MSSW modes that cause asymmetric propagation are discussed in the following sections.

6.1 Interfacial DMI in MSSW modes

In the following section we will describe how i-DMI affects surface spin waves, and why this effect is different for waves traveling in opposite directions. In figure 6.2, a schematic view is given of a spin wave in a ferromagnetic layer in contact with a high spin-orbit coupling material. As discussed in section 2.1, the i-DMI energy $E_{\text{i-DMI}}$ is determined by the i-DMI vector $\boldsymbol{D}$, the amount of rotation of neighboring spins and their direction of rotation. As depicted by the triangle in the figure, the vector $\boldsymbol{D}$ is oriented perpendicular to the relative position of the spins (x-direction) and the direction of symmetry breaking (z-direction). Its sign is a material property and is chosen to be negative in the figure. Since the direction of the canting is important as well, we distinguish between spin waves with a counter-clockwise (CCW) and a clockwise (CW) chirality. In the figure, the cross-product of neighboring spins is explicitly shown, which is anti-parallel to $\boldsymbol{D}$ for CCW waves and parallel for CW waves. Therefore, CCW waves have lower en-

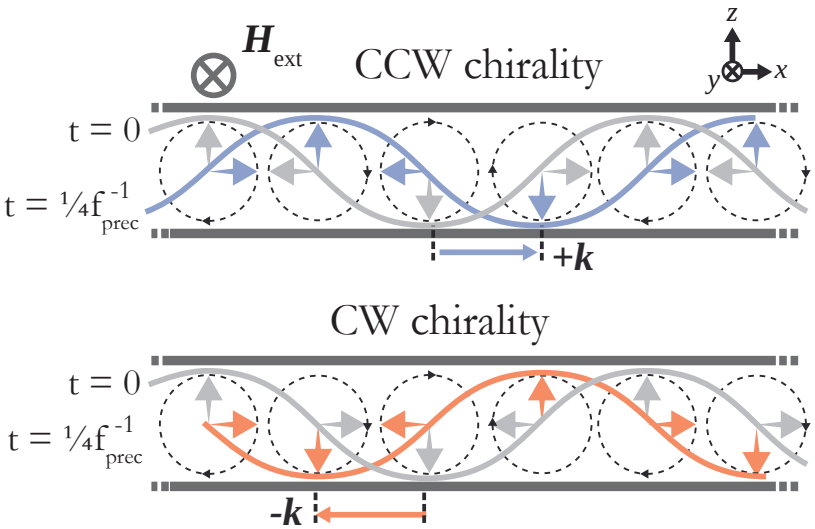

Figure 6.3: Spins at $t = 0$ (grey arrows) start to precess around an external field. The situation after one quarter revolution is represented by colored arrows. Due to the fixed precession direction, clockwise (CW) and counterclockwise (CCW) spins have shifted in opposite directions.

ergy, while CW spin waves are increased in energy. Since the frequency of the spin wave is directly related to the energy, measuring the frequency difference of CW and CCW spin waves gives information about the strength of $\boldsymbol{D}$.

Now that we know that the frequency for CW and CCW spin waves is different, we only need to show how this expresses itself in the propagation direction of both waves. Therefore, we will consider the time evolution of a CCW and a CW chiral spin wave, as depicted in figure 6.3. At $t = 0$ the magnetization, represented by the grey arrows, starts to precess in a fixed direction determined by the external field direction. After one quarter revolution, this results in the situation represented by the colored arrows. We see that for CCW waves, the envelope of the perturbations has shifted to the right ($+k$ waves), while for CW waves it has shifted to the left ($-k$ waves). Reversing the field, and thus the precession direction, also reverses the sign of k.

Due to the properties mentioned above, MSSW modes can be used to extract i-DMI by measuring the resonance frequency difference $f(+k) - f(-k)$ for counter-propagating waves. The magnitude of $\boldsymbol{D}$ can be quantified by introducing an i-DMI field $\boldsymbol{H}_{\text{i-DMI}}$ in the LLG-equation from which the dispersion relation for MSSW modes can be derived. Using equation 2.9 and noting that the system is independent on the y-coordinate, we derive an i-DMI field

$$\mu_0 \boldsymbol{H}_{\text{i-DMI}} = -\frac{D_S}{t_{\text{FM}} M_S} \left(\hat{\boldsymbol{y}} \times \frac{\partial \boldsymbol{m}}{\partial x} \right). \tag{6.1}$$

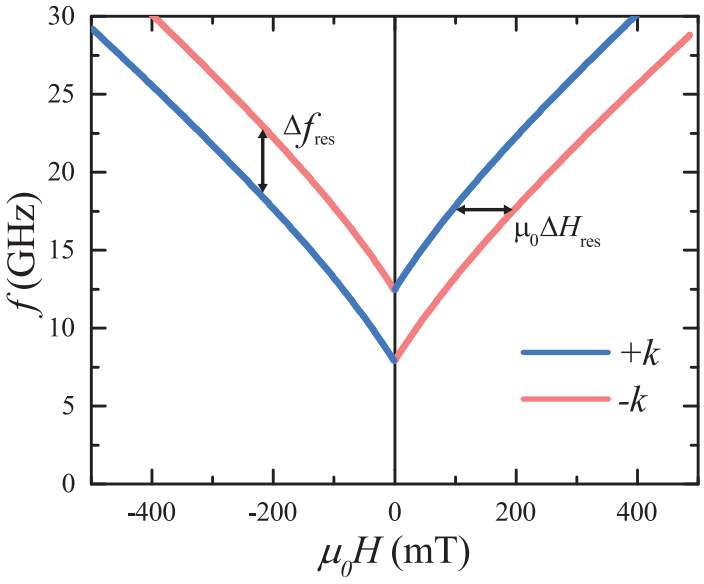

Figure 6.4: The dispersion relation for $+k$ and $-k$ spin waves in the presence of i-DMI (effect is exaggerated for clarity).

We can insert the field in the derivation of the polder tensor and, analogous to section 3.1, derive the resonance frequency for surface waves[24]

$$f = \frac{\gamma\mu_0}{2\pi}\left[\sqrt{H(H+M_{\text{eff}}) + \frac{M_S M_{\text{eff}}}{4}\left(1-\exp(-2|k|t_{\text{FM}})\right)} + p\frac{2kD_S}{\mu_0 M_S t_{\text{FM}}}\right], \tag{6.2}$$

where again $M_{\text{eff}} = M_S - H_K$ and $p = \pm 1$ is the polarity of the applied field. The first term in the square root is the resonance condition for FMR modes (obtained by setting $k = 0$). The second term in the square root is the product of the in-plane and out-of-plane contribution to the dynamic dipolar field of the propagating waves. As expected, by introducing a i-DMI field a term arises that is odd in both k and p. By taking the difference of the precession frequencies of oppositely propagating spin waves, we have a measure for the i-DMI,

$$\Delta f \equiv f(+k) - f(-k) = 2\frac{\gamma k D_S}{\pi t_{\text{FM}} M_S}. \tag{6.3}$$

The parameters M_S and k in this equation are all relatively easy to measure, giving an accurate way to determine D_S. An example of the influence of D_S on the resonance frequency for $\pm k$ waves is depicted in figure 6.4. The difference in resonance frequency Δf_{res} is a measure for the strength of D_S. Similarly, if the applied frequency is kept constant, and the field is swept, equation 6.2 can be simply inverted to obtain H_{res} as

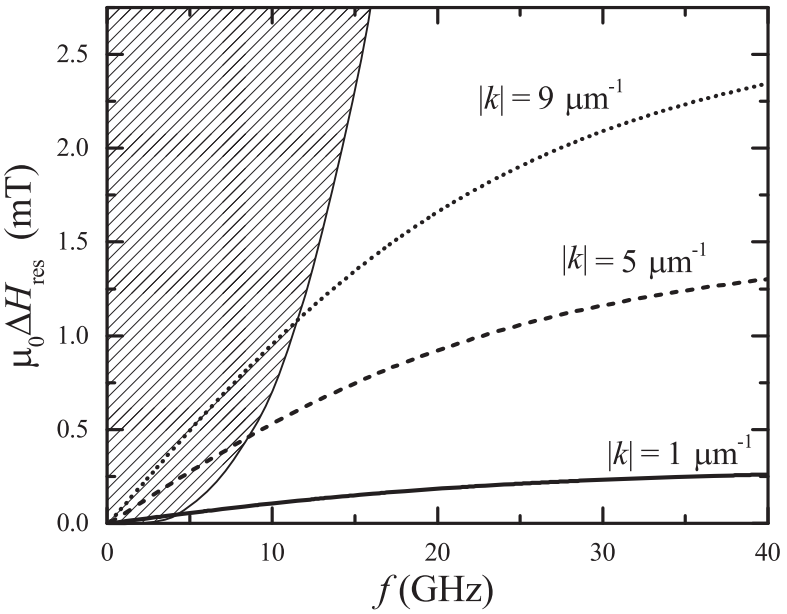

Figure 6.5: The difference in resonance field $\mu_0\Delta H_{\text{res}}$ for oppositely traveling waves, as a function of the frequency for typical magnetic parameters of a Co film. The used thickness equals $t_{\text{FM}} = 20$ nm and $D_s = 2$ pJ/m[26]. The marked area represents unphysical behavior, since for these combinations of frequencies/wave number a negative resonance field is found.

a function of f. By measuring ΔH_{res}, one can also extract D_S. The latter method will be used in this thesis. An example of the expected resonance shift as a function of the applied frequency for typical magnetic parameters for Co is depicted in figure 6.5. A typical shift of several mT or less if found for a literature value $D_s = 2$ pJ/m[26] and a wave number $k = 9$ μm^{-1} or less. The shift is increasing for increasing applied frequency. Also, for frequencies below a certain treshold (marked area) no shift can be found, since for these combinations of frequencies/wavenumber a negative resonance field is found.

6.2 Other contributions to asymmetric propagation

While the resonance frequency is indeed influenced by i-DMI, it is not the only interaction that causes asymmetric propagation. Another effect that can induce a frequency shift originates from the localization of spin waves. We will first give an intuitive explanation for the localization of surface spin waves. Then, the effect of the localization on propagation of spin waves will be discussed.

To see why surface spin waves are localized, we consider the dynamic dipole field

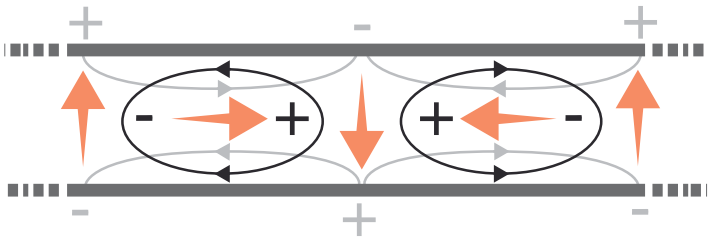

Figure 6.6: A clockwise spin wave (red arrows) locally generates magnetic poles (+ and -). Field lines generated by the in-plane and out-of-plane components of the spin wave are given by black and grey lines respectively. Figure adapted from Gladii *et al.* [28].

of the MSSW depicted in figure 6.6[28]. The x and z components of the magnetization cause local magnetic poles ($+$ and $-$) in the thin film. For CW spin waves like in the figure, the field lines of the x and z component (black and gray, respectively) add constructively near the bottom interface, while they cancel near the top interface. This causes an exponentially decaying spin wave profile along the thickness of the magnetic film with decay length $1/k$, where k is the wave number of the spin wave. This can result in an additional frequency shift if interface anisotropy is present, which can be explained as follows.

Consider the case when only the bottom interface of the magnetic film exhibits interface anisotropy. Localization on the bottom interface causes a net increase in the anisotropy field perceived by the spin wave compared to when the spin wave is localized on the top interface. From the dispersion relation (equation 6.2, the increase in anisotropy increases the frequency. Since localization and i-DMI are both directly related to the chirality of the spin wave, both mechanisms possess the same symmetry (odd in both $\boldsymbol{k}$ and $\boldsymbol{H}$). Moreover, like i-DMI, the anisotropy induced frequency shift increases with increasing k due to stronger localization on the surface. Calculations show that for thinner layers (5 nm or less) the anisotropy induced shift is significantly reduced compared to the i-DMI shift for magnetic parameter values similar to Co/Pt trilayers, since the amplitude is not as much decayed at the opposite interface[28].

Other interface related effects like spin-pumping also contribute to asymmetric propagation, but this will mainly affect the intensity and linewidth of the observed signals and therefore do not cause any ambiguity in the observed peak shifts. In the next section we will discuss how we can excite and independently measure $+k$ and $-k$ spin waves.

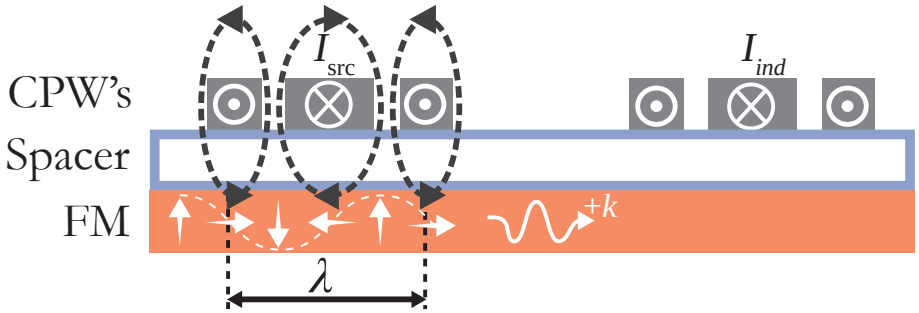

Figure 6.7: Spin waves are excited in a ferromagnetic (FM) layer by sending a source current I_{src} through a coplanar waveguide. Spin waves propagate outward, where a current I_{ind} is inductively generated in a second CPW. The dimensions of the CPW determine the wave number $k = 2\pi/\lambda$ of the spin wave.

6.3 A transduction model for non-reciprocal spin wave propagation

To investigate the influence of i-DMI on propagating spin waves, we first need to excite spin waves with a finite wavelength. In propagating spin wave spectroscopy experiments, excitation is done similar to the co-planar waveguide (CPW) method used in the FMR experiments in part 1 of this thesis. As shown in figure 6.7, the difference is that now the spacing between the ground lines determine the wavelength of the excited spin waves and two separate CPW's are used instead of one. By sending a high-frequency current I_{src} through for example the left CPW, spins locally align with the Oersted field of the CPW. This forces the excitation of spin waves with a well-defined wave number $\pm k$. After excitation, the spins propagate outwards. The $+k$ spin waves inductively generates a current I_{ind} in the second CPW. Similarly, when the right CPW is used as a source, $-k$ waves are detected by the left CPW. To prevent current flowing directly between the CPW's, an insulating spacer layer is separating the CPW and ferromagnetic layer.

A model has been developed by Vlaminck and Bailleul [69], which calculates the change in self-inductance and mutual inductance of two CPW's on a ferromagnetic strip due to spin wave excitation. In their model, they obtain a relation between the current running through the source antenna, the precession of the magnetization given by the permeability tensor $\overline{\overline{\chi}}$ and the voltage induced in both CPW's by using a quantity called the surface permeability, as was first done by Emtage [70]. This model elegantly demonstrates the various physical mechanisms contributing to the lineshape observed in our experiments. First, the model will be described and a physical interpretation of

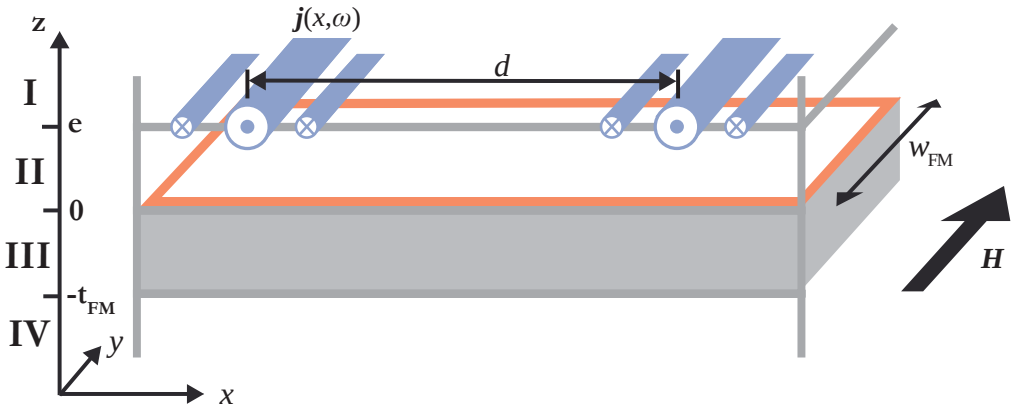

Figure 6.8: Geometry used in the derivation of L_{11} and L_{21}, consisting four separate regions. The current density of the antenna is located at the interface of region I and II.

the equations will be given. We will conclude this chapter on a more practical note and discuss what the consequences of this model are for the design of the CPW structures used to excite and detect spin waves.

Physical description of the model

A side-view of the geometry used for this model is shown in figure 6.8. Four separate regions (I-IV) can be distinguished. The bottom region IV represents the non-ferromagnetic substrate, region III the ferromagnetic strip with thickness t_{FM} and width w_{FM}, region II the insulating layer between the ferromagnetic material and the antenna with thickness e and finally region I which represents the free space above the antenna. To simplify the calculation, the model assumes that all current $j(x,\omega)$ running through the CPW is localized at the interface between region I and II, corresponding to the plane $z = e$. What we are interested in is an expression for the self-induction L_{11} and mutual induction L_{21} of the CPW's. Instead of providing the entire derivation, we will start by giving the final result of the model and discuss the physical meaning of the different terms. Following the derivation of Vlaminck and Bailleul [69], the self-inductance can be expressed as

$$L_{11} = \frac{P_{\mathrm{tot}}}{i\omega I^2} = \frac{w_{\mathrm{FM}} \int p(x,\omega)dx}{i\omega I^2} = \frac{w_{\mathrm{FM}}}{2\pi} \int_{-\infty}^{+\infty} \left(\frac{1}{k} \left| \frac{\tilde{j}(k,\omega)}{I} \right|^2 \Lambda(k,\omega) \right) dk. \tag{6.4}$$

As indicated by the first equality, the inductance is calculated in terms of the total power P_{tot}. Since the considered geometry assumes an infinitesimally thin conductor, P_{tot} is

defined as the total power contained in the $z = e$ plane above the magnetic strip. The system is independent of the y-coordinate, so the total power can be expressed as a product of the width of the strip w_{FM} and the power per unit volume $p(x, \omega)$ integrated along the x-coordinate. Without going into the technical details, Parseval's theorem has been used to transform the calculation of $p(x, \omega)$ along the x-coordinate to reciprocal space, which explains the integration variable k on the right hand side of the equation. In the integral on the right hand side, we can distinguish between two contributions to the self-inductance.

Firstly, the factor $\widetilde{j}(k, \omega)$ represents the Fourier transform of the current density in the CPW. It accounts for the fact that a different shape of the CPW excites different spin waves, altering the inductive response. In appendix B, an expression is derived to explicitly calculate $\widetilde{j}(k, \omega)$. Secondly, the factor $\Lambda(k, \omega)$ has units of linear inductance and can be interpreted as the inductive response of the CPW per unit of length (units typically pHμm^{-1}). It accounts for which components of the Fourier transform $\widetilde{j}(k, \omega)$ actually excite spin waves in the magnetic film, which depends on the applied field and frequency. The factor Λ can be calculated using

$$\Lambda(k, \omega) = \frac{\mu_0}{\frac{1}{\mu_S(k, e^+, \omega)} - \frac{1}{\mu_S(k, e^-, \omega)}}. \tag{6.5}$$

The first term in the denominator represents the magnetic response of the system just above the current carrying interface, $z = e^+$ and is quantified by the so-called surface permeability μ_S. The second term involves the magnetic response just underneath the current carrying boundary at $z = e^-$ and includes the precessional behavior of the magnetic film near resonance. For details on how to calculate μ_S, we refer to the original paper by Vlaminck and Bailleul [69]. For the mutual inductance a similar expression is obtained and equals

$$L_{21} = \frac{w_{\text{FM}}}{2\pi} \int_{-\infty}^{+\infty} \left(\frac{1}{k} \left| \frac{\tilde{j}(k, \omega)}{I} \right|^2 \Lambda(k, \omega) \exp(-ikd) \right) dk. \tag{6.6}$$

The exponential factor results from the distance d between the excitation signal and the reception signal, corresponding to the distance d between the CPW's.

All information about asymmetric propagation is contained in the surface permeability $\mu_S(k, e^-, \omega)$. It is a function of the components of the permeability tensor, which is given by

$$\overline{\overline{\mu}} = \overline{\overline{I}} + \overline{\overline{\chi}} \tag{6.7}$$

where $\overline{\overline{I}}$ is the unit matrix. In figure 6.9 the inductive response is given as a function of k for typical parameter values of a Pt/Co stack with $t_{\text{Co}} = 20$ nm. We see that for the given magnetic parameters, $f = 15$ GHz and $\mu_0 H_{\text{ext}} = 155$ mT, the inductive response peaks at $k = 7$ μm^{-1} due to the excitation of spin waves with this wavenumber. The

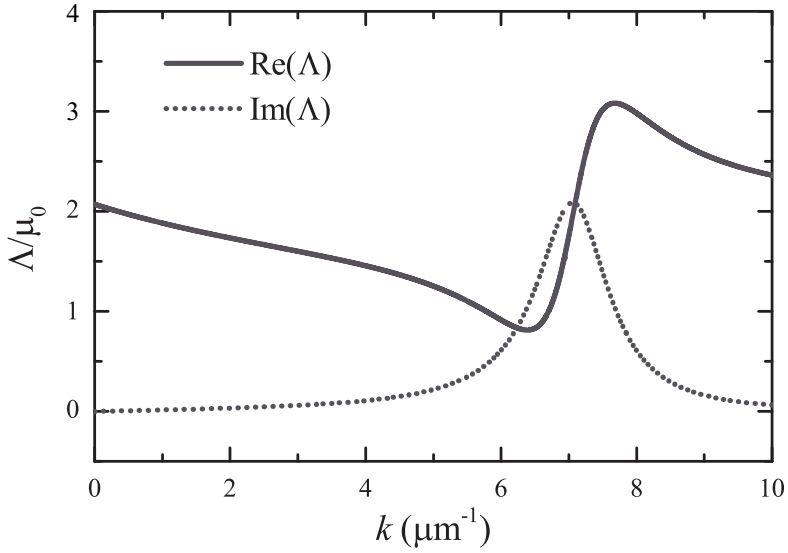

Figure 6.9: Inductive response Λ as a function of the wavenumber k. For the input parameters $M_S = 1.4 \cdot 10^6$ A/m, $H_K = 0.7 \cdot 10^6$ A/m, $g = 2.16$, $\alpha = 0.01$, $t_{\text{FM}} = 20$ nm and $e = 160$ nm were used. The applied frequency $f = 15$ GHz and field $\mu_0 H = 155$ mT.

peak position can also be derived from the dispersion relation for surface waves given in section 6.1. The non-zero baseline of the real part of Λ can be attributed to the direct electromagnetic coupling between the CPW's.

Consequences for CPW design

The presence of the factor $\widetilde{j}(x, \omega)$ in the expression for L_{11} and L_{21} has some important consequences for our antenna design. In figure 6.10a we use the equations derived in appendix B to calculate $\widetilde{j}(x, \omega)$ for a CPW structure with a 900 nm distance between the ground lines. As we can see from the graph, the main component of the Fourier transform is located at a wave number $k_M = 7$ μm^{-1}. However, the width of the Fourier transform Δk_M is very large, meaning that a wide range of spin waves with different wave numbers will be excited. To simplify the analysis of the effect of i-DMI on spin waves, an almost monochromatic excitation of spin waves is preferred. This can be achieved by repeating the CPW structure N times to form a meander shaped antenna, like shown in figure 6.10b. The outline of the magnetic strip is indicated by the red lines. Perfect monochromatic excitation would occur for $N \to \infty$. However, the finite attenuation length of spin waves limits the maximum number of meander repetitions, since the distance between the excitation and the detection antenna would simply become too large to contribute to the induced signal. Therefore, in this research

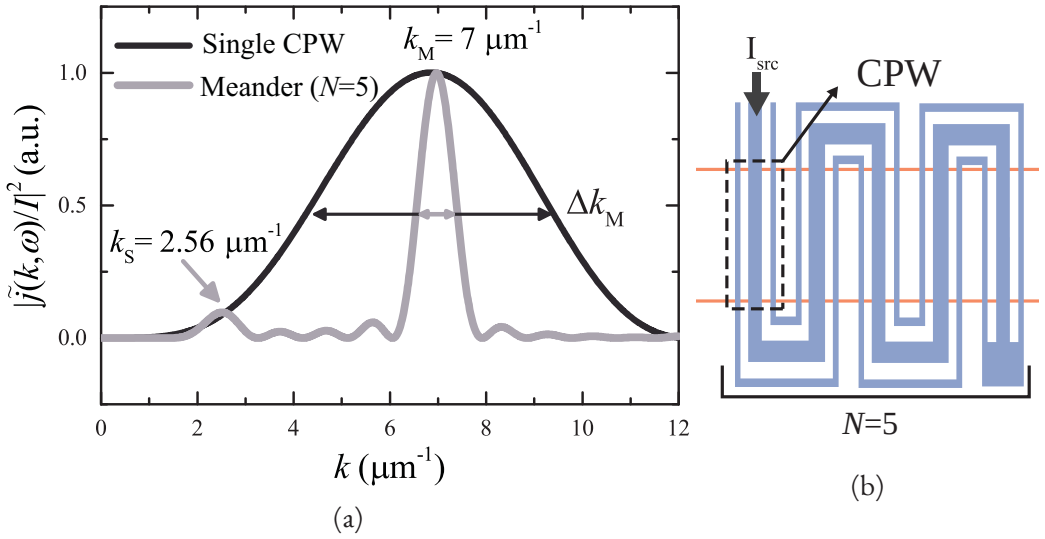

Figure 6.10: (a) The fourier transform of an antenna with $N = 1$ and 5 repetitions of the CPW structure. (b) Top view of an antenna with $N = 5$ repetitions of the CPW structure. Red lines indicate the placement of the magnetic strip.

we have chosen to create antennas with $N = 5$. The Fourier transform of the current density of such a meander shaped antenna with $N = 5$ is given by the grey curve in figure 6.10a. The peak width Δk_M is significantly reduced. We also see that a secondary peak is appearing at $k_S = 2.56$ μm^{-1}. In principle, both waves can be used to extract information about i-DMI.

In conclusion, using equations 6.4-6.6 combined with the calculated Fourier transform of the current density in the antenna, we now have all the ingredients to determine the electric response of the antennas due to spin wave excitation. The main limitation of the model is the assumption of infinitely thin current densities. In reality, the antennas are 100 nm thick, which is of the same order of magnitude as the spacer layer thickness and the magnetic layer thickness. However, as we will see in the results section, the model gives good qualitative understanding of the observed signals. In the following chapter we will describe the experimental tools used to fabricate the antenna structures and the setup used to measure propagating spin waves.

Chapter 7

Experimental tools for propagating spin wave spectroscopy

One of the major differences between the FMR and PSWS experiments in this thesis lie in the way the Coplanar Waveguide (CPW) is designed. For PSWS, traveling spin waves with a finite wavelength have to be excited instead of uniform precession. This is only possible if the perturbation field of the CPW possesses the same spatial periodicity as the desired spin waves. In the previous chapter we have derived that i-DMI induces a shift in resonance frequency or field, which is more pronounced for higher wave numbers k. Therefore, smaller wavelengths and thus smaller structures are favored. In the all-electrical approach, this requires high resolution nano-structuring tools like electron beam lithography. In the following sections we will discuss how the samples and setup are designed to fulfill the requirements in order to measure i-DMI in spin waves. We will again focus on stacks including a Co/Pt interface for high spin-orbit coupling.

7.1 Electron beam lithography

One of the major challenges in all-electrical spin wave spectroscopy is patterning the small structures required for measuring i-DMI related phenomena. Electron beam lithography (EBL) can be used to pattern structures down to the nanometer regime. EBL locally exposes electron sensitive resist, which can then be processed to form a deposition mask directly on the substrate. Details on the processing steps used in this thesis are given later in this section.

While the resolution of optical lithography techniques is mainly limited by diffraction, the resolution of EBL is much more complicated to predict due to aberrations in electron optical components and the many electron-matter interactions in the substrate and resist itself. This means that the parameters used during the patterning process have to be carefully chosen to give optimal results for the specific substrates and resists used

for the experiments. To get an idea of what parameters influence the electron beam resolution before it reaches the sample, a short introduction will be given to the operating principles of EBL. Then the most important electron-matter interactions influencing the resolution will be briefly discussed. At the end of this section we will discuss the process which allows for patterning the complex structures necessary for this research with a lateral resolution of tens of nanometers.

EBPG Operating principles

In this research, a Raith Electron Beam Pattern Generator (EBPG) 5150 was used. This state-of-the-art nano-structuring system uses a high current density thermal field emission gun to generate free electrons. These electrons are accelerated towards the sample in the electron beam column. Here the electron beam is also focused, corrected for aberrations and deflected with extremely high accuracy. A simplified diagram of an electron beam column and its components is sketched in figure 7.1. The whole system is kept under high vacuum in the range 10^{-6}-10^{-8} mbar. A vibration isolation table minimizes errors induced by the environment. We will shortly discuss some of thes elements in the electron beam column

The thermal field emission gun, also called a Schottky emitter, consists of a sharp tungsten needle heated to temperatures above 1000 °C. A large electric field is applied to stimulate electron emission and accelerates the electrons towards the sample. The high temperature improves stability, since it reduces adsorption of atoms on the needle tip. Schottky emitters have the additional advantage of having a very small source size[71], which improves the beam resolution.

In the electron beam column, the beam is modified by various electron optical elements. Electron beams can be focused with electrostatic and magnetic fields provided by electron lenses. However, these lenses introduce relatively strong aberrations compared to their optical counterpart. This can be partly solved by using apertures to center the beam as much as possible, at the cost of a lower beam currents. Stigmators can also correct for aberrations caused by a difference of focus points for different beam axes (astigmatism).

The electron beam eventually reaches the deflectors. These deflect the beam to different spots on the sample. For the EBPG5150, the deflector and beam blanker instructions come from a 50 MHz pattern generator, providing high writing speed even for complex patterns. The range of the deflectors is limited to write fields of $\sim$ 500 μm^2. For larger patterns, the stage has to be physically moved. A laser interferometer is used to improve the accuracy of the stage positioning, providing write field stitching with nanometer accuracy. Additionally, the height of the sample is also accurately determined with a laser which improves the overall focus on the sample.

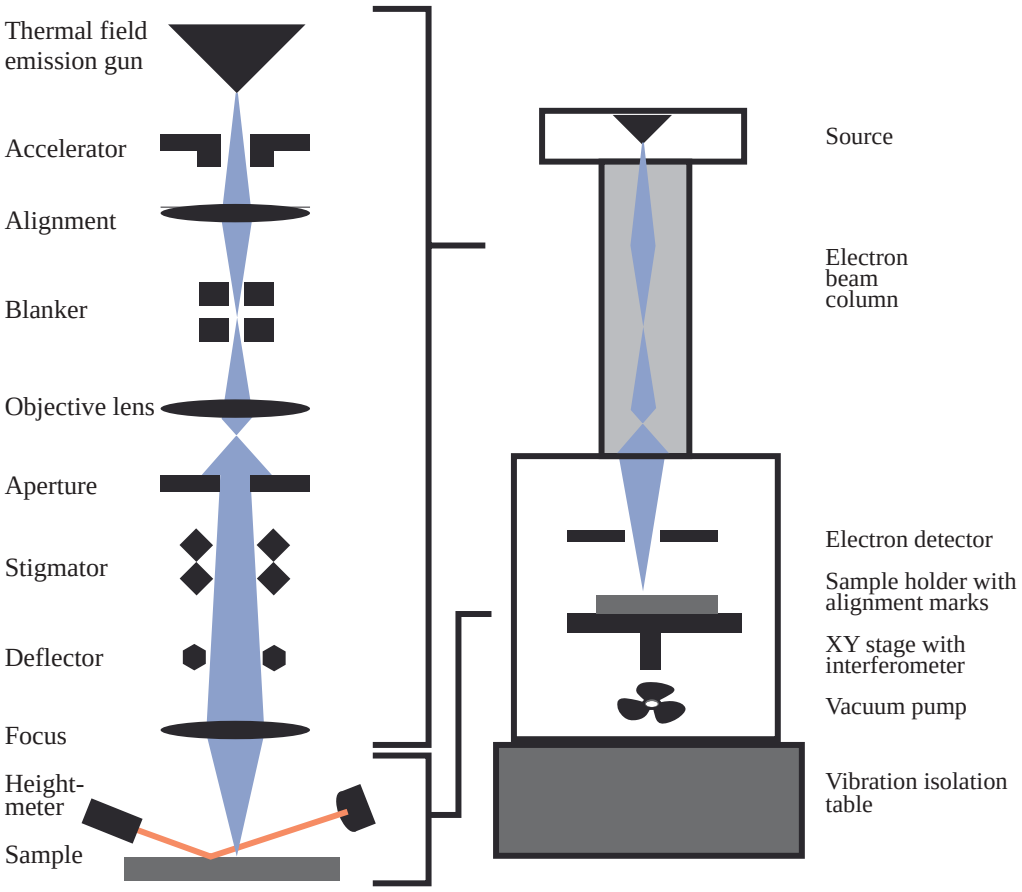

Figure 7.1: The various components in the electron beam column shape and focus the electron beam on the substrate. On the left, a close-up is given of the components in the EBL system depicted at the right.

Beam resolution and writing speed

The final resolution of the electron beam depends on several parameters. In a perfect electron beam column, the source size divided by the the demagnification M^{-1} gives the beam diameter. Inclusion of spherical and chromatic abberations increases the beam diameter, depending on the energy spread of emitted electrons by the electron source and the half angle (radial spread) of the electron beam. According to the specification sheet, the Raith EBPG 5150 has a theoretical smallest feature size of less than 8 nm.

However, beam diameter does not solely determine the resolution of the exposed structures. Scattering events in the exposed resist and the substrate increase the exposed area. Firstly, forward scattering in the resist with thickness t_R (in nm) increases the effective beam diameter d_f to[72]

$$d_\mathrm{f} = 0.9 \left(\frac{t_R}{V_b} \right)^{1.5}, \tag{7.1}$$

where V_b is the accelerating voltage of the electron beam in kV. For the EBPG 5150, $V_b = 100$ kV. In this thesis typical resist thicknesses are in the range 200-300 nm, giving $d_\mathrm{f} \approx 3.5$ nm. Secondly, backscattering in the substrate can return electrons back in the resist, even microns away from the electron beam. The amount of backscattering depends on the substrate. In particular atoms with a high atomic number can increase backscattering. Higher beam voltages cause deeper electron impingement into the substrate, therefore decreasing the backscattering effect. Various models exist to calculate the amount of backscattering, such that the EBL can correct for this so-called proximity effect.

All in all, with optimized EBL parameters a smallest feature size of tens of nm should be possible with the complex structures used in this research. If the writing speed is an issue, larger beam diameters can be used by increasing the aperture size. This both increases the beam current and the radial spread of the electron beam, increasing the beam spot size. This can significantly reduce the writing time of large patterns. Of course, this decreases the resolution of the exposed structures significantly, so it should mainly be used for larger structures.

High-resolution lift-off

For high-resolution patterning, both type used of resist as well as the processing methods are critical. A commonly used and simple method is to use a polymethyl methacrylate (PMMA) bi-layer lift-off process, which is also used for this thesis. A thin layer of PMMA with high molecular weight is spincoated on top of a thicker layer of PMMA with low molecular weight. When exposed to an electron beam, bonds are broken in both layers (figure 7.2a). For PMMA with high molecular weight (longer polymer

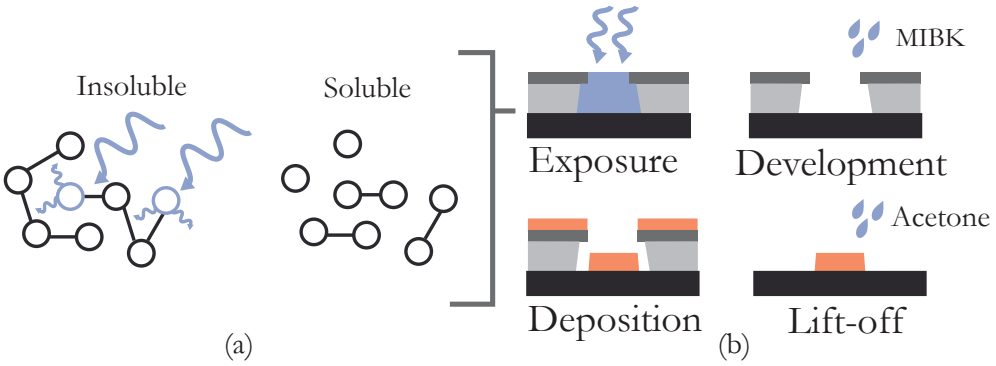

Figure 7.2: (a) To make patterns, high-energy electrons (large arrows) are absorbed, while emitted secondary electrons (small arrows) break the bonds between the molecules. (b) After exposing the resist it is developed with MIBK, the material is deposited and the unwanted material is lifted-off with acetone.

chain), more bonds need to be broken compared to the smaller chains to be able to process the material. In other words, longer polymer chains are more resistant to electron exposure. As shown in figure 7.2b, the lower resistance of the bottom layer means that more resist is exposed compared to the top layer. When the layers are exposed to methyl isobutyl ketone (MIBK) in the so-called 'development' step, the bottom layer has been dissolved more, providing us with a large undercut. As shown in the figure, this prevents material deposition on the side-walls of the PMMA. Finally, in the 'lift-off' step the layers are exposed to acetone, which dissolves the rest of the PMMA, such that only the exposed patterns are left on the substrate.

A major advantage of using PMMA instead of other high-resolution resists like hydrogen silsesquioxane (HSQ), is its ease of use. PMMA reacts relatively little with water, air and daylight and can be developed several days after the exposure with only minor loss in pattern quality. The general procedure for the PMMA bi-layer lift off process as used in this research is as follows:

1. Clean substrate
   (a) Acetone rinse in ultrasonic bath for 120 seconds
   (b) Isopropanol rinse in ultrasonic bath for 60 seconds
   (c) Blowdry sample with N_2
2. Apply resist
   (a) Spincoat PMMA 495K A6[1] at 3000 rpm for 60 seconds. This results in a thickness $t_{\text{PMMA}} \approx 260$ nm.

[1]We use the notation PMMA [molecular weight][solvent][volume percent] (solvent A=Anisol)

(b) Pre-bake at 150°C for 60 seconds to evaporate solvent.

(c) Spincoat PMMA 950K A2 at 3000 rpm for 1 minute. This results in a thickness $t_{\mathrm{PMMA}} \approx 60$ nm.

(d) Pre-bake at 150°C for 60 seconds to evaporate solvent.

3. Expose the pattern with the EBPG5150.

4. Develop the sample in a 3:1 solution of IPA:MIBK for 60 seconds, immediately followed by 30 sec rinse in IPA to stop development.

5. Post bake to evaporate left-over liquids for 5 minutes at 100°C.

6. Deposit material with sputter deposition or electron beam evaporation.

7. Lift-off with acetone in an ultrasonic bath for 120 seconds, followed by 60 seconds rinse in isopropanol.

8. Inspection with scanning electron microscope.

The parameters used for exposure have been carefully chosen based on various dose tests. Various electron beam currents, step sizes and doses have been tested to optimize the quality of the patterned structures required for PSWS.

7.2 Two-Port VNA spin wave spectroscopy

For the propagating spin wave experiments, we used a setup similar to the FMR experiments in part 1. However, as shown in figure 7.3, now both ports of the VNA are used instead of only one. Each port is connected to a separate antenna placed on a ferromagnetic strip. The spatial periodicity of the antenna determines the wavelength of the excited spin waves, which will subsequently travel through the strip towards the other antenna. In the figure, port 1 is used as excitation port and port 2 inductively detects the spin waves, meaning $+k$ spin waves are detected. By switching the source and detection port, a $-k$ spin wave can be measured. We refer to chapter 4.1 for details about the individual components of the setup.

The setup is used in the field-sweep configuration, meaning that the applied frequency is kept constant and the external field is swept. As discussed in part 1, this method is less prone to calibration errors and does not require a reference measurement, improving the signal-to-noise ratio and measurement speed. Instead of converting the S-parameters to a susceptibility χ, we will express the observed signals in terms of a change in inductance ΔL so that it can be compared to the transduction model by

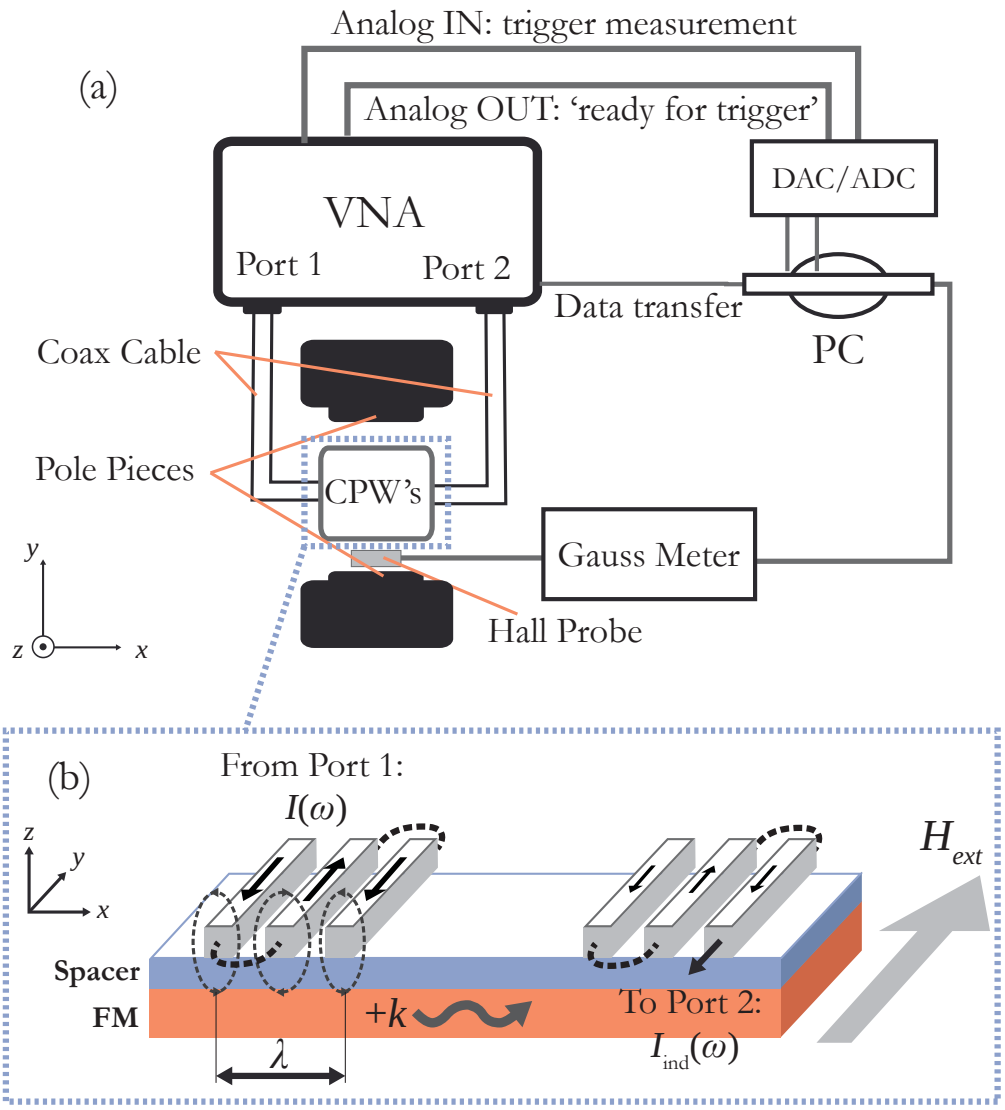

Figure 7.3: (a) Top view of the setup used for the non-reciprocal spin wave measurements in this thesis. See figure 4.1 in part 1 for more details about the setup. (b) The two ports are connected to their own CPW placed on a ferromagnetic strip. The spatial periodicity of the CPW's determines the wavelength λ of the excited spin waves. Here, port 1 acts as a source which excites spin waves with the antenna's Oersted field, such that the signal induced at port 2 corresponds to a spin wave traveling in the $+k$ direction.

Vlaminck and Bailleul [69]. First, we use the relation $\overline{\overline{L}} = \overline{\overline{Z}}/i\omega$, where the impedance matrix $\overline{\overline{Z}}$ can be calculated with the formula[73]

$$\overline{\overline{Z}}/Z_0 = \frac{\overline{\overline{I}} + \overline{\overline{S}}}{\overline{\overline{I}} - \overline{\overline{S}}}, \tag{7.2}$$

where Z_0 is the characteristic impedance of the network (50 Ω) and $\overline{\overline{I}}$ the identity matrix. The self-inductances L_{11} and L_{22} give information about the excited spin waves at antenna 1 and 2 respectively, while L_{21} and L_{12} give information about the spin waves excited at one port and detected at the other. The inductance is multiplied by a phase factor $\exp(-i\phi)$ to account for the propagation of the high frequency signal though the CPW structure itself. Finally, constant offset terms are added to account for non-magnetic contributions to the S-parameters.

Since the signals and shifts in the resonance field due to i-DMI are typically very small, we first estimate the feasibility of this experiment. First, we assume that the amplitude of the change in inductance ΔL_{12} is similar to other PSWS experiments found in literature, which is several pH or less[69]. This corresponds to a change in S-parameter of 10^{-5}-10^{-3}, which is well above the noise-floor $\delta S \approx 0.5 \times 10^{-6}$ of the VNA used in this research.

Secondly, we can estimate the DMI shifts $\Delta H_{\text{res}} = |H_{\text{res}}(+k) - H_{\text{res}}(-k)|$ for thin Co layers by inverting equation 6.2 to obtain H_{res} as a function of f and k. Taking the magnetic parameters for Pt/Co stacks obtained from part 1 and a literature value $D_S = 2$ pJ/m for a film thickness $t_{\text{FM}} = 20$ nm, we estimate that the shift in resonance field $\mu_0 \Delta H_{\text{res}}$ is in the order of several mT or less. The Gauss meter used in this setup has a resolution $\delta B = 0.1$ mT, which is well below the expected shift.

To further substantiate this estimation, we use the transduction model introduced in the previous chapter to calculate the response of an antenna with a main fourier peak at $k_M = 6$ μm^{-1} and a secondary Fourier peak at $k_S = 2.2$ μm^{-1}. We use a theoretical i-DMI value $D_S = -2$ pJ/m at the Pt/Co interface[26]. The remaining magnetic parameters are assumed to be similar to the FMR measurements from part 1. The resulting change in the imaginary part of the mutual inductance $\text{Im}(\Delta L)$ as a function of the applied field is shown at the bottom of figure 7.4. The blue and the red curve represent $+k$ and $-k$ spin waves, respectively. Both for negative and positive applied fields we can clearly distinguish between two resonance peaks. The peak at an applied field $\mu_0 H \approx \pm 30$ mT corresponds to the k_M wave, while the peak at $\mu_0 H \approx \pm 82$ mT corresponds to the k_S wave. Close-ups of the two peaks at negative and positive applied field are shown at the top of the figure. As expected, we see that the resonance field of $+k$ and $-k$ waves are shifted with respect to each other as a result of i-DMI. The size of the shift, $\Delta H_{\text{res}}(\pm k) = H_{\text{res}}(+k) - H_{\text{res}}(-k)$, is given for each peak. For negative i-DMI, as used here, the $+k$ spin wave has a higher H_{res} for positive fields. If we compare the shifts for the various resonance peaks, we see that a larger

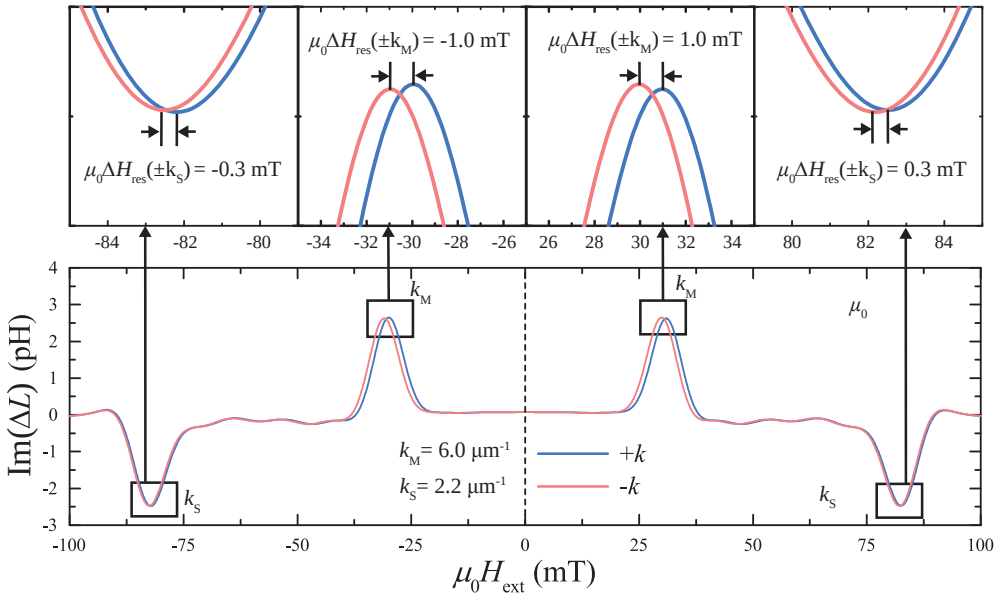

Figure 7.4: At the bottom, the calculated response of an antenna with $k_M = 6.0$ µm^{-1} and $k_S = 2.2$ µm^{-1} is shown for a magnetic strip thickness $t_{FM} = 20$ nm. The applied frequency equals $f = 12.5$ GHz and an antenna distance $d = 4.77$ µm. Typical magnetic parameters for a Co film have been used, with $D_S = -2$ pJ/m[26]. Close-ups of the resonance peaks, including their peak shifts ΔH_{res}, are shown at the top of the figure.

shift $\mu_0 \Delta H_{\text{res}}(\pm k_M) = 1.0$ mT is found for the k_M peak compared to 0.3 mT for the k_S peak. This agrees with our predictions, since the shift is linearly proportional to the magnitude of the wave number of the spin wave. Furthermore, when the direction of the applied field is reversed, the peak shift also changes sign. This is also expected behavior, since the i-DMI induced shift is proportional to the polarity of the field p.

Finally, for the fabrication of the antennas with a wavenumber $k > 5$ µm^{-1}, which should give a measurable i-DMI induced shift, a minimal feature size of approximately 150 nm is required (see following section on sample design). Using the proposed fabrication methods in the previous section, this is relatively easy to achieve. So all in all, both the fabrication and measurement of the DMI shift is theoretically possible using the given experimental tools. In the next section we will indicate how the samples are designed and what stacks are used to try and detect i-DMI.

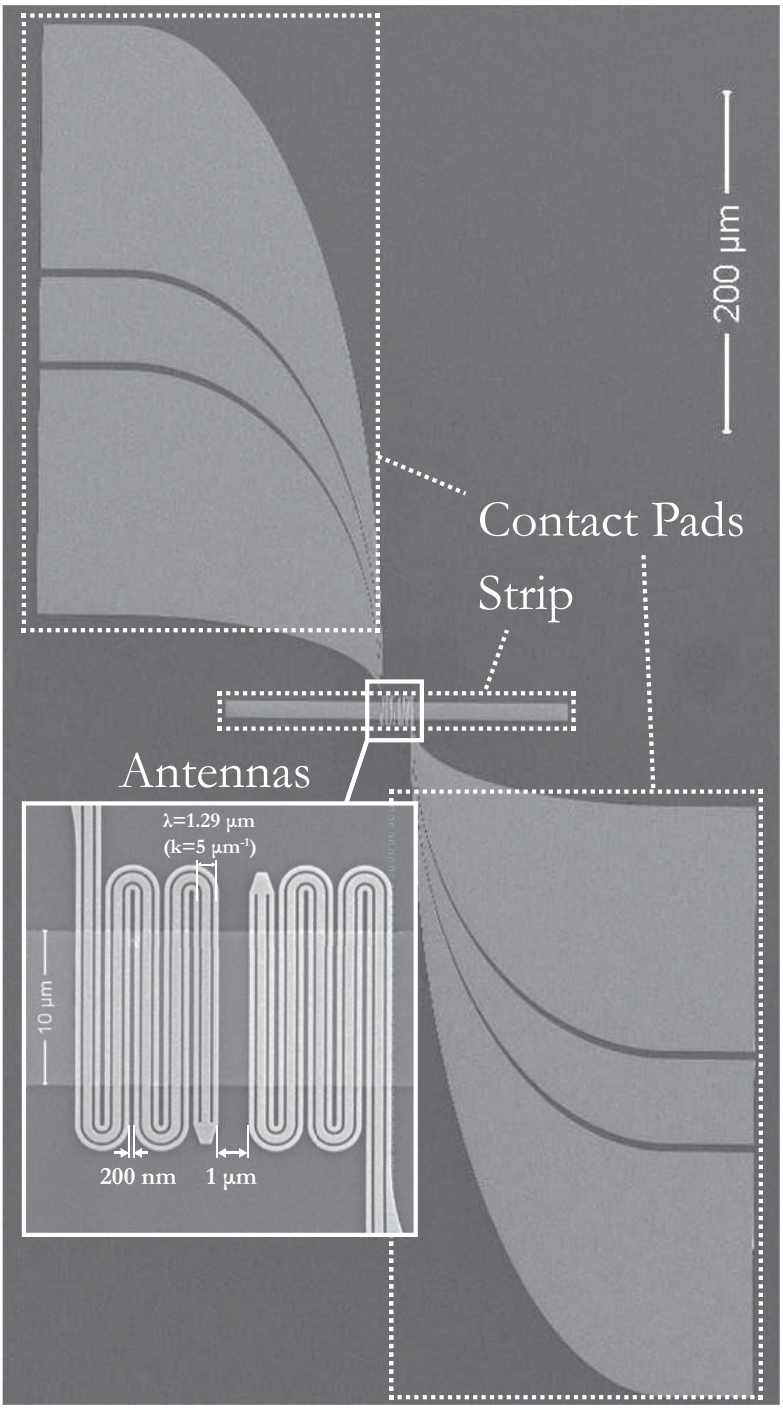

Figure 7.5: The samples used for propagating waves consist of a magnetic strip with two meander shaped CPW's ('antennas') on top, separated by a distance of 1 µm. The antennas in this figure have a periodicity corresponding to $k = 5$ µm^{-1}. The antennas are connected to the contact pads, on which probe tips can be landed.

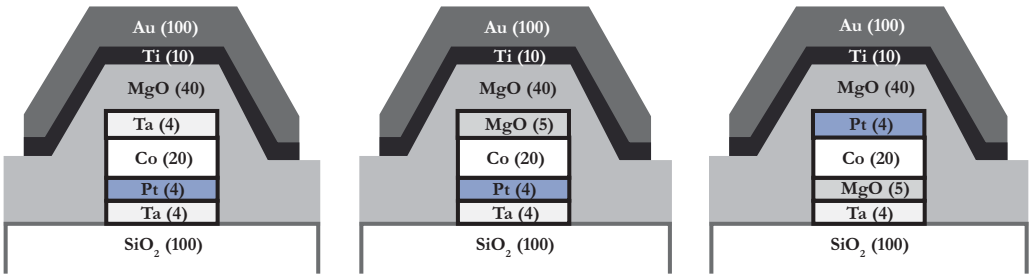

Figure 7.6: A sideview of the stacks used in this research consist of a magnetic strip, an insulating layer of MgO, and a Ti/Au antenna structure.

7.3 Sample design

For PSWS experiments, samples are created using EBL, sputter deposition and electron beam evaporation. The samples are created in three steps, resulting in the structures given in figure 7.5:

1. Using electron beam lithography, a 10 μm wide magnetic strip is patterned, which acts as a waveguide for the spin waves. The magnetic material is deposited using sputter deposition.

2. A 40 nm thick insulating MgO layer is sputtered over the whole sample. This prevents shunting currents from one antenna to the other via the metallic strip.

3. Again using EBL, two meander shaped CPW's are patterned over the strip. Two contact pads on which the probe tips can be landed are also patterned and connected to the antennas. Electron beam evaporation is used to deposit the antennas and contact pads. They consist of a 10 nm Ti adhesion layer and a 100 nm thick Au layer.

The antenna is designed such that its periodicity determines the wavelength of the excited spin wave. As an example, the antenna in the figure has a main periodicity $\lambda = 1.29$ μm. This corresponds to a main Fourier peak at a wave number $k_M = 5$ μm^{-1} and a secondary Fourier peak at $k_S = 1.8$ μm^{-1}. The end-to-end antenna distance is taken to be 1 μm. To improve broad-band signal response, round corners have been used for the meander. The smallest features of this antenna are approximately 200 nm in size, which can be easily achieved using the high-resolution lift-off process used in this thesis. Theoretically, using this design the fabrication limit would be somewhere between $k = 15$-20 μm^{-1}. However, since not all EBL and deposition parameters have been optimized during this thesis, antennas with wave numbers higher than $k = 7$ μm^{-1} could not be consistently fabricated.

For this research, various stacks have been used for the magnetic strip. Since we are interested in stacks with high DMI, we have chosen to grow strips consisting of Ta(4)/Pt(4)/Co(20)/MgO(5) and Ta(4)/Pt(4)/Co(20)/Ta(4) stacks. The numbers in parentheses are layer thicknesses given in nanometers. These stacks are reported to show relatively high i-DMI[29]. Since the signal strength of transmission measurements is estimated to be an order of magnitude smaller than typical FMR measurements from the previous chapter, a relatively thick magnetic layer $t_{\mathrm{FM}} = 20$ nm is used. The downside of this is the decreased influence of i-DMI, which scales with t_{Co}^{-1}. The stacks will be referred to as the Pt/Co/MgO and the Pt/Co/Ta stack respectively. To investigate the sign of the DMI, an inverted stack, Ta(4)/MgO(5)/Co(20)/Pt(4), is also studied. This inverted stack is believed to have a similar DMI strength, but opposite in sign[29], which results in an opposite peak shift for $+k$ and $-k$ spin waves. This will be referred to as the MgO/Co/Pt stack. The total sample stacks are also depicted in figure 7.6.

Finally, full sheet samples with the same stacks as the magnetic strips have been deposited as well. These samples were used for FMR measurements to get an indication of the magnetic properties of the patterned strips. The results of these measurements were used as input parameters for the analytical model developed by Vlaminck and Bailleul [69], as described in section 6.3. This model will help us understand the experimental results in the next chapter.

Chapter 8

Results and discussion

In this chapter we will present the results for asymmetric spin wave propagation. First, we will investigate the properties of the excited spin waves to verify the quality of our antennas. The measurements are then qualitatively compared to the transduction model to gain insights in the influence of the various magnetic parameters in ferromagnetic strips. Then we will discuss the asymmetric spin wave propagation in various Co/Pt stacks and also compare them with the transduction model. Finally, we will conclude this chapter with a discussion on the observed discrepancies between the model and the results and propose directions for further research.

8.1 Excitation spectrum

To verify whether the sample design correctly excites the desired spin waves, the excitation spectrum given by the self-inductance L_{11} on the Pt/Co/Ta strip is measured. The sample is designed such that the main peak of the Fourier transform of the current density in the antenna is located at $k_M = 5$ µm^{-1} and the secondary Fourier peak at $k_S = 1.8$ µm^{-1} (see also appendix B). In figure 8.1a the change in inductance is shown as a function of the applied magnetic field for various frequencies. We find that for all applied frequencies there are indeed two resonance peaks present, indicating the excitation of two spin waves with different wavelengths. The main resonance peak at lower field corresponds to the short wavelength spin waves (k_M) and the secondary peak at higher field to long wavelength spin waves (k_S). The latter is indicated by the small arrows in the figure. As can be seen from the figure, increasing the applied frequency f both increases the resonance fields and the linewidths of the observed peaks, indicating the signal indeed originates from resonance in the ferromagnetic layer. For frequencies $f \gtrsim 15$ GHz, the k_S appears as a shoulder on the main resonance peak. This complicates the signal analysis at these frequencies. Another complication arises due to the curvature of the signal away from resonance, which is most clearly seen for $f = 12$

GHz in the region from 150-200 mT. It originates from non-linear background effects in the setup, as described at the end of section 4.1. Due to the background effects, fitting the measured ΔL_{11} to the transduction model can give highly distorted results.

Instead of fitting the complete graph to the transduction model, we can locally fit the absorption $\mathrm{Im}(\Delta L_{11})$ near resonance to a Lorentzian function. Both the main resonance field and the secondary resonance field are determined from the fitted peak positions for various applied frequencies f. These two datasets can be simultaneously fitted to the Kittel equation for surface waves (equation 6.2) with k and M_{eff} as free parameters. The gyromagnetic ratio is fixed by setting $g = 2.16$, which is obtained from FMR measurements of a full sheet sample with the same stack. The results are given in figure 8.1b. The main resonance peak corresponds to a wave number $k_M = 5.5 \pm 0.2\ \mu\text{m}^{-1}$ and the secondary peak to a wave number $k_S = 1.4 \pm 0.1\ \mu\text{m}^{-1}$. As we can see from the graph, the main peak slightly deviates from the fit for higher frequencies. Here, the resonance field is overestimated, which can be explained by the fact that the overlapping secondary peak distorts the position of the main resonance peak to higher fields. However, we can conclude that, despite the rather primitive interpretation of the signal, it is likely that the correct spin waves are excited. Investigating samples with even smaller linewidths could give more data points for the k_S peak for a more accurate fit.

While a similar excitation spectrum was found for MgO/Co/Pt, the reverse stack, Pt/Co/MgO, consistently showed only one broad resonance peak. This is shown in figure 8.2 for various applied frequencies. To explain the different behavior of the stack Pt/Co/MgO, the transduction model is used. We find that a damping constant $\alpha = 0.02$ is required to best reproduce the experimental linewidths for MgO/Co/Pt and Pt/Co/Ta, compared to $\alpha = 0.06$ for Pt/Co/MgO. So even though we can still explain the measured signal, the result implies that we can expect extremely large linewidths for propagations measurements on Pt/Co/MgO. As mentioned earlier, a large signal linewidth can drastically complicate the interpretation of the signal when both resonance curves overlap. Moreover, peaks shifts due to i-DMI are much easier to distinguish for sharp peaks than for broader peaks. While no direct evidence could be found for the origin of the large linewidth, several suggestions can be made:

1. High damping: To verify whether the damping in Pt/Co/MgO is increased, the same stack was studied on a full sheet sample with the FMR setup from the previous part. The results are given in table 8.1. The obtained damping constant is indeed significantly larger than both other stacks, which are close to the value for bulk Co. This means that the presence of MgO at the top interface enhances damping significantly. However, all samples seem to have a damping parameter more than a factor 2 too small to explain the size of the observed linewidth.

2. Inhomogeneous broadening: The inhomogeneous broadening in full sheet samples $\Delta B < 1$ mT is not enough to explain the large linewidth. However, care

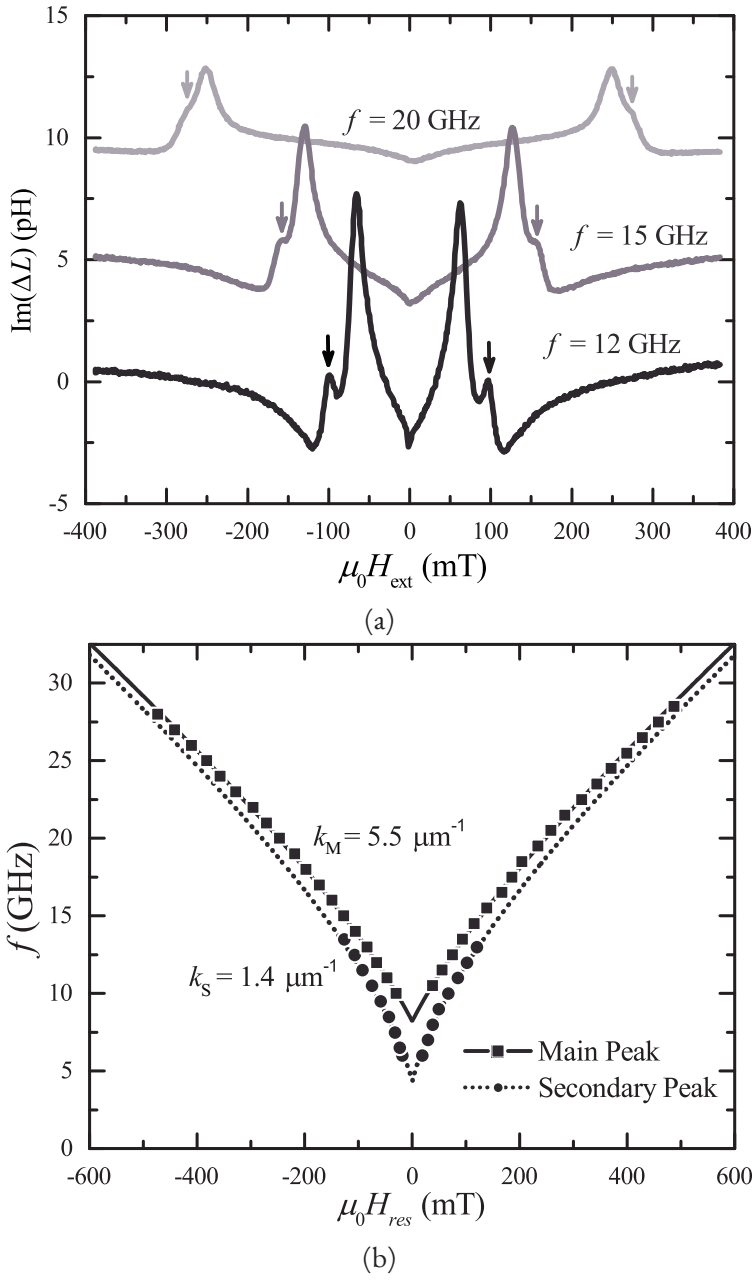

Figure 8.1: (a) The imaginary part of the change in induction ΔL_{11}. The graphs have a cumulative offset of 5 pH for clarity. The arrows indicate the secondary resonance peak. (b) The main and secondary resonance frequency is plotted as a function of the resonance field. The solid and dashed lines are fits to the Kittel equation 6.2.

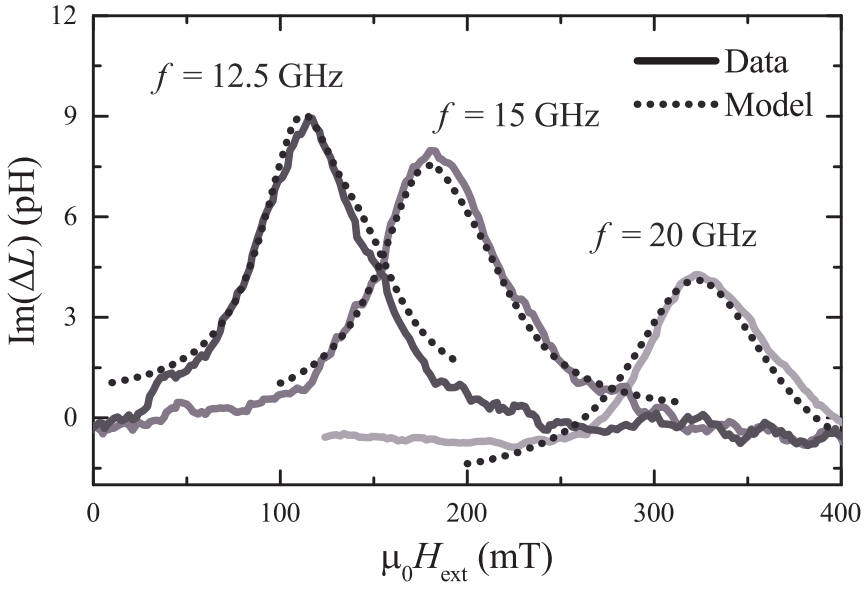

Figure 8.2: The reflected signal for a $k_M = 5\ \mu\text{m}^{-1}$ antenna on Pt/Co/MgO for various applied frequencies. Solid lines indicate predictions by the transduction model for $M_S = 1.4 \cdot 10^6$ A/m, $g = 2.16$, $H_K = 0.72 \cdot 10^6$ A/m, $\alpha = 0.06$ and $e = 200$ nm.

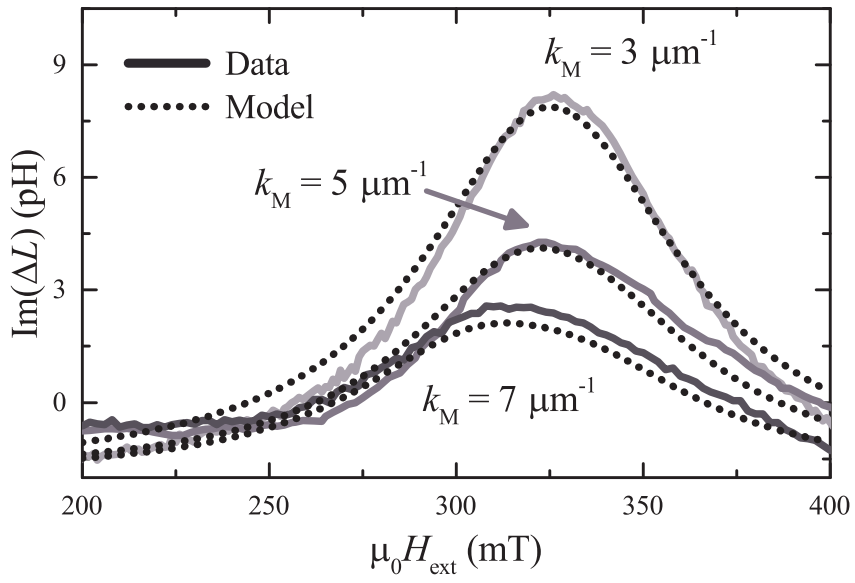

Figure 8.3: The reflected signal for various k_M antennas on Pt/Co/MgO for $f = 20$ GHz. Solid lines indicate predictions by the transduction model for $M_S = 1.4 \cdot 10^6$ A/m, $g = 2.16$, $H_K = (0.69\text{-}0.72) \cdot 10^6$ A/m and $\alpha = 0.06$.

Table 8.1: Magnetic properties obtained by FMR measurements of the stacks studied in this chapter. The anisotropy field $H_K = M_S - M_{\text{eff}}$ is determined with the assumption that $M_S = 1.4 \cdot 10^6$ A/m.

Stack	M_{eff} ($\times 10^6$ A/m)	H_{K} ($\times 10^6$ A/m)	g	α	$\mu_0 \Delta H$ (mT)
Pt/Co/Ta	1.1	0.3	2.16	0.01	0.5
Pt/Co/MgO	0.85	0.55	2.16	0.025	0.5
MgO/Co/Pt	1.3	0.1	2.15	0.008	0.5

must be taken since the length scales of the propagating spin wave measurements differ significantly from FMR measurements. For finite wavelength spin waves, there are more scattering states compared to the FMR mode, increasing the contribution of magnon scattering[74]. Also, pinning near the edges of the patterned strips can induce additional inhomogeneous effects, but these are expected to be small[75]. Varying the width of the strip could shed light on the contribution of this effect.

3. Fabrication: A third cause for broad linewidths could be the quality of the magnetic strip. The interfaces or growth texture can be altered by the various fabrication steps of the sample compared to the full sheet samples studied by FMR. Optimizing the development time to minimize PMMA residue on the substrate or cleaning the pattern after development with oxygen plasma could increase substrate quality before deposition.

4. Broad Fourier spectrum: Finally, an increased linewidth could also be induced by the fact that the Fourier spectrum of our antenna is not optimal. If we have a bad (i.e. broad) Fourier spectrum, the total linewidth is increased as well since a wider range of wavelengths is excited. However, SEM imaging shows no structural damage in the antennas or increased edge roughness, so this is unlikely to be the case. Moreover, antenna quality is likely to become better for larger structures. However, figure 8.3 shows that for various antennas with different k_M, similar magnetic parameters can be used to describe the peak position and intensity. This shows us that the behavior is probably not caused by structural defects in the antenna.

We can conclude that the fabricated antennas excite the correct spin waves. However, broad linewidths indicate that the strips behave sub-optimal.

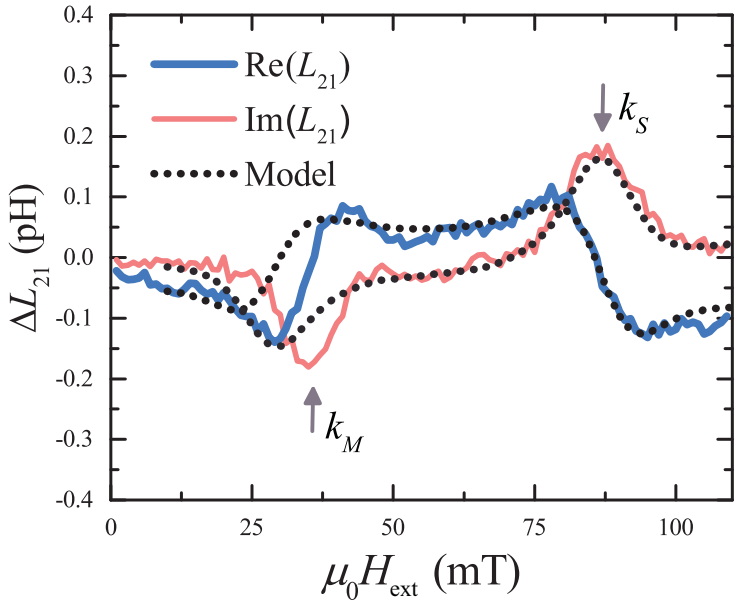

Figure 8.4: Example of measurement for L_{21} for MgO/Co/Pt at 13 GHz and $k_M = 7$ µm^{-1}. Arrows indicate the resonance fields of the main and secondary peak, k_M and k_S, respectively. Input parameters for the transduction model are given in table 8.2.

8.2 Non-reciprocal spin wave propagation

In this section we are interested in a shift in resonance field for $+k$ spin waves obtained from L_{12} and $-k$ spin waves obtained from L_{21}. As discussed in section 7.2, we expect to see a small i-DMI induced shift for the k_S peak and a larger shift for the k_M peak when we compare the resonance field of $+k$ and $-k$ spin waves. The peak shift is also expected to change sign upon reversal of the applied magnetic field (see also section 7.2). Before extracting a peak shift, we will first use the transduction model to explain the observed transmission signal. Then, we will discuss the asymmetric propagation and propose additional physical mechanisms driving the asymmetry. Finally, we will propose methods that can provide further understanding of the asymmetric propagation of MSSW. Unfortunately, the Pt/Co/Ta antennas were damaged from previous measurements, so they are not studied for propagation measurements. Therefore, we start by investigating the MgO/Co/Pt samples, since their relatively small linewidth allows us to distinguish between k_S and k_M peaks at frequencies below 15 GHz.

Table 8.2: Magnetic and geometrical properties used as input parameters for the transduction model for the investigated stacks. For both stacks, $M_S = 1.4 \cdot 10^6$ A/m, $g = 2.16$, $t_{\text{FM}} = 20$ nm, $w_{\text{FM}} = 10$ µm. For MgO/Co/Pt, D_S was not used to explain the lineshape.

Stack	H_k ($\times 10^6$ A/m)	α	D_S (pJ/m)	e (nm)
Pt/Co/MgO	0.62	0.07	-	270
MgO/Co/Pt	0.26	0.022	-10	270

MgO/Co/Pt

An example measurement of the change in induction ΔL_{21} for an MgO/Co/Pt sample is shown in figure 8.4. Like in the excitation spectrum, we can distinguish between two separate resonance peaks, indicated by the symmetric and antisymmetric Lorentzian-like functions in the imaginary and real part of the signal, respectively. As a reminder, note that the resonance peak for high wavenumbers k_M occurs at lower fields and the k_S spin waves at higher fields. The two absorption peaks in the imaginary part of L_{21} show that the two spin waves have opposite phase due to the different wavelength of both spin waves. This is correctly predicted by the transduction model for an effective antenna distance $d = 6.30$ µm, corresponding to 82% of the center to center distance between the antennas. However, the relative position of the resonance fields is smaller when compared to the transduction model. Also, the linewidth for the k_M peak seems to be overestimated as well, while the k_S spin wave is in good agreement with the experiment. This could mean that the damping[76] or inhomogeneous broadening[74] is k-dependent as well, which is not taken into account in the model.

To investigate asymmetric propagation, the response of a $+k$ and $-k$ spin wave is shown in the bottom graph of figure 8.5, corresponding to the mutual inductances L_{12} and L_{21}, respectively. We see a total of four resonance peaks, two for positive applied field and two for negative applied fields. These again result from spin waves with a wave number k_S and k_M, as indicated in the figure. For the peak corresponding to the k_M spin wave, we see that there is a clear asymmetry in amplitude present for counter-propagating waves. We also see that the asymmetry in amplitude reverses for positive and negative applied fields. We also see that both signals show distinctly different features, like the extra peak at $\mu_0 H = \pm 50$ mT. These could not be reproduced by the transduction model, so the data could not be fitted directly. However, like in the excitation measurements, we can locally fit the k_M and k_S peaks with a Lorentzian function to extract a peak shift. The results are shown in the close-up at the top of figure 8.5. The shift is negative for positive applied fields, meaning that $-k$ spin waves have a larger H_{res}). The shift changes sign when the field direction is reversed. Both the peak shift and asymmetry in amplitude observed in the MgO/Co/Pt sample will be discussed in

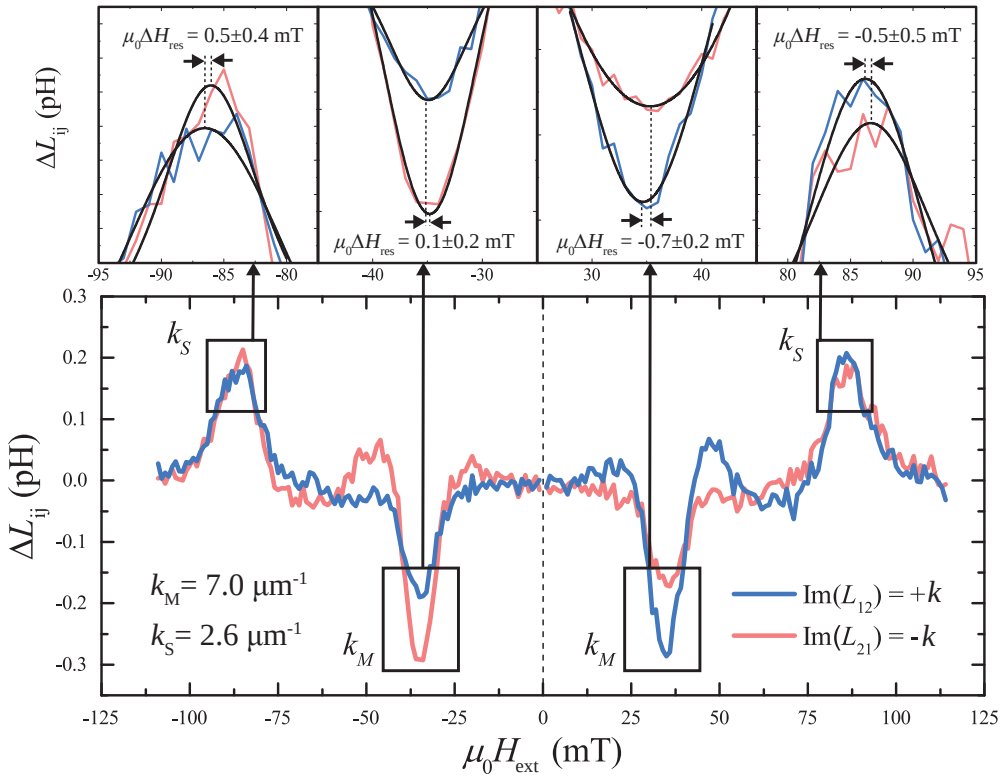

Figure 8.5: Example of measurement for L_{12} and L_{21} corresponding to a $+k$ and $-k$ spin wave respectively. Again, MgO/Co/Pt is used with $k_M = 7$ µm^{-1}. The applied frequency $f = 13$ GHz. Close-ups of the resonance peaks, including local fits (black lines) are shown at the top of the figure. The resulting peak shifts are also given.

more detail below.

Asymmetric spin wave dispersion

First, the peak shifts for both the k_M and the k_S peak are extracted by locally fitting the imaginary part of the signal with a lorentzian function, as shown at the top of figure 8.5. When we average the absolute peak shift values for positive and negative applied field, we get $\mu_0|\Delta H_{\text{res}}| = 0.4 \pm 0.2$ mT and 0.5 ± 0.4 mT for the k_M and k_S wave, respectively. Contrary to what is expected, the peak shift for k_S spin waves seems to be higher than the k_M spin waves. The same trend is observed in measurements of the same sample at higher frequencies. In figure 8.6, the change in inductance of the same sample is shown for $f = 15$ GHz and $f = 20$ GHz. Since the asymmetry reverses for opposite field, we have averaged the data for $+k$ spin waves at positive field and $-k$ spin waves at negative field for the blue line. This data corresponds to a counterclockwise

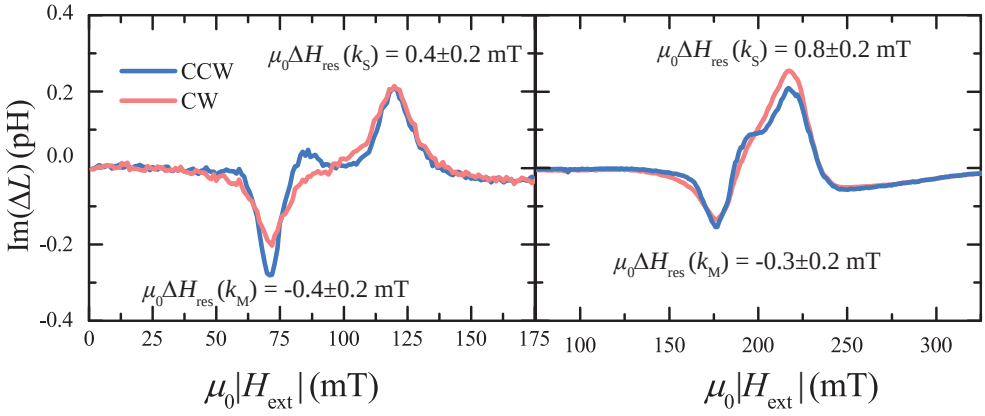

Figure 8.6: The change in inductance for counter propagating waves at $f = 15$ GHz (left) and $f = 20$ GHz (right). The counterclockwise chiral wave is calculated by averaging the $+k$ wave at positive field and the $-k$ wave at negative field. The clockwise chiral wave is the average of the $-k$ and $+k$ spin wave at negative and positive field, respectively. Peak shifts corresponding to the k_S and k_M waves are also given.

chiral spin wave (see also section 6.1). The red line is the averaged data for $-k$ and $+k$ spin waves at positive and negative field, respectively. Again, a small shift could be extracted for the k_M spin wave and a larger shift for the k_S spin wave. While the k_M peak shift shows consistent values for different applied frequencies, the magnitude of the k_S peak shift strongly varies and even changes sign compared to the case where $f = 13$ GHz. Therefore, conclusions from this fitting data should be taken with care. If we nonetheless assume that the k_M peak shift results from i-DMI, we can use equation 6.2 to find a positive i-DMI constant $D_{\mathrm{S,Co/Pt}} = +0.6 \pm 0.3$ pJ/m. Here, we have assumed that all i-DMI originates from the Co/Pt interface. However, the inconsistent results for the k_S peak, combined with the fact that the fitting uncertainties for the peak shifts are relatively large, creates ambiguity in the conclusions drawn from the fitted peak shift.

Nonetheless, when we compare our results to literature, we find that the sign of the observed i-DMI is consistent. While not much is known about the i-DMI in the stack MgO/Co/Pt specifically, the sign of the i-DMI in Pt/CoFe/MgO[77], Pt/Co/AlOx[26] and ab initio simulations of Pt/Co[58] was found to be negative. However, since we used the opposite stack, MgO/Co/Pt, the sign of D_S is reversed. Therefore, our results regarding the sign of the i-DMI are in agreement with literature. However, its magnitude is approximately three times smaller than reported values for this stack[29]. To explain this small value for D_S, one could argue that the peak shift induced by i-DMI is reduced by the shift caused by the localization of spin waves near an interface with strong anisotropy field, as described in section 6.2. For example, consider a spin

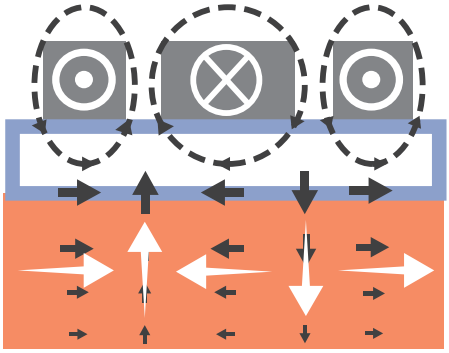

Figure 8.7: The Oersted field below an antenna, given by the black arrows, couples to the magnetization, shown in white. In the figure, the spin wave has counterclockwise chirality.

wave with a wave vector $+k$. For positive applied field, these spin waves are localized at the top Co/Pt interface (see also figure 6.1). If we assume that the Co/Pt interface has a higher interface anisotropy than the MgO/Co interface, the $+k$ spin wave feels a stronger effective anisotropy field. Whereas positive i-DMI decreases the resonance field for $+k$ waves, an increase in anisotropy field increases the resonance field. Therefore, the i-DMI induced peak shift of $+k$ spin waves is reduced due to its localization on the top interface. For $-k$ spin waves, both i-DMI and the localization induced shift is reversed, but still work in opposite directions.

Asymmetric spin wave amplitudes

Secondly, besides the small peak shift, a large change in amplitude is present for oppositely traveling k_M waves. Interestingly, this amplitude asymmetry is not present at the k_S peak. Qualitatively, several causes for k-dependent asymmetry in the amplitude can be distinguished.

1. Asymmetric spin wave excitation: Even without i-DMI, spin waves with opposite chirality can have a different excitation amplitude. As shown in figure 8.7, the horizontal and vertical component of the perturbation field caused by the antenna both couple to the dipolar field of the excited spin waves. If both components are in phase with the dipolar field, like in the figure, larger amplitude spin waves are generated compared to opposite chirality spin waves[30, 78, 79]. From the figure it can see that in the considered geometry the excitation field inherently favors counterclockwise chirality. This is in agreement with the experiments, where a higher amplitude is found for counterclockwise chiralities.

2. Asymmetric damping: Spin wave localization on an interface can cause additional damping in the presence of, for example, spin pumping. Since the spin

wave amplitude drops exponentially along the thickness of the layer with decay length $1/k$, high wavenumbers are more localized, providing more spin pumping[76]. This agrees with our observations where the k_M wave is more affected than the k_S wave. To roughly estimate the size of this effect, we use a variation of the mean field approach used to estimate the effective anisotropy field in MSSW modes[29, 35]. First, we assume that the spin pumping mechanism is localized in one monolayer of Co at the interface with thickness t_{ML}. We then calculate the effective spin pumping contribution $\alpha^{\mathrm{eff}}_{\mathrm{pump}}$ by weighting the local spin pumping contribution by the spin wave amplitude $m(k, z)$,

$$\alpha^{\mathrm{eff}}_{\mathrm{pump}}(k) = \frac{\int_0^{t_{\mathrm{Co}}} \alpha_{\mathrm{pump}}(z) m(k, z) dz}{\int_0^{t_{\mathrm{Co}}} m(k, z) dz}, \tag{8.1}$$

where $\alpha_{\mathrm{pump}} = g^{\uparrow\downarrow}_{\mathrm{eff}} \gamma \hbar / 2\pi M_S t_{\mathrm{ML}}$ for $0 < z < t_{\mathrm{ML}}$ and $\alpha_{\mathrm{pump}} = 0$ otherwise. The spin wave amplitude is calculated using $m = \exp(-kz)$. For convenience, height $z = 0$ corresponds to the Co/Pt interface at the bottom of the magnetic film, while $z = t_{\mathrm{Co}}$ represents the top of the film. Using the results from the FMR measurements in part 1 we can calculate the difference in damping $\Delta\alpha^{\mathrm{eff}}_{\mathrm{pump}} = |\alpha^{\mathrm{eff}}_{\mathrm{pump}}(+k) - \alpha^{\mathrm{eff}}_{\mathrm{pump}}(-k)|$. Using $g^{\uparrow\downarrow}_{\mathrm{eff}} = 20\,\mathrm{nm}^{-2}$, $\gamma = 1.9{\cdot}10^{11}$ rad/sT and $t_{\mathrm{ML}} = 0.25$ nm, we obtain $\Delta\alpha^{\mathrm{eff}}_{\mathrm{pump}} = 0.0003$ for $k = \pm 7\ \mu\mathrm{m}^{-1}$. However, this is roughly a factor 10 too small to explain the amplitude difference observed in figure 8.5.

Moreover, the sign of the high amplitude spin wave indicates that high damping does not occur for localization at the Co/Pt interface, but rather the MgO/Co interface. Therefore, spin pumping is not likely the physical mechanism behind asymmetric damping.

3. Localization dependent coupling: Stronger coupling between the antenna and spin waves localized on the top interface can occur, since they are closer to the antenna. This agrees with observations, since the spin waves localized at the top interface (blue for positive field, red for negative) have higher amplitudes. This effect can be tested by measuring the inverted stack, Pt/Co/MgO. If the same waves show higher amplitude after inverting the stack, it means that not the interfaces, but the localization itself is likely to cause the asymmetry. However, as we will see later in this chapter the Pt/Co/MgO samples used in this thesis could not give a conclusive result on this argument.

4. Interfacial DMI: The i-DMI is also known to cause an asymmetry in the attenuation length for counter propagating waves. This can be explained by the change in group velocity v_g for $\pm k$ dipolar waves, given by the expression[24]

$$v_g^{\pm} = v_0 \pm \frac{\gamma p 2 D_S}{t_{\mathrm{Co}} M_s}, \tag{8.2}$$

where v_0 is the group velocity without i-DMI. An increase in group velocity for equal damping time scales means that the spin wave has a higher amplitude at the detection antenna. Using an upper limit value for $D_S = 2$ pJ/m[26] results in a 1% change of the attenuation length, which is not enough to explain the observed amplitude difference.

Based on the previous points, we can rule out spin pumping at the Co/Pt interface and the i-DMI induced group velocity shift as the dominant mechanisms. However, asymmetric coupling to the Oersted field of the antenna can induce the observed difference in amplitude of counter-propagating waves. Varying the interface materials, the thickness of the ferromagnetic film or inverting the layer stack can give information about the physical mechanism dominating here.

Pt/Co/MgO

The Pt/Co/MgO stack is expected to exhibit opposite i-DMI and thus an opposite peak shift. Unfortunately, similar to its excitation spectrum, even at low frequencies the k_M and k_S resonance peaks are overlapping. A typical example for $k_M = 3$ µm^{-1} and $f = 15$ GHz is shown in figure 8.8. The intensity of the signal is more than a factor two smaller than for the opposite stack, which can be attributed to the shorter attenuation length due to larger damping of Pt/Co/MgO (see table 8.1). A peak shift is visible and seems to be opposite to the shift found in the MgO/Co/Pt stack. Now, the CCW spin wave (again calculated by averaging the $+k$ signal for positive applied fields and the $-k$ signal for negative fields) has a higher resonance field. This indicates a negative i-DMI. As an initial guess for the i-DMI strength, the peaks are again fitted with a Lorentzian function, as shown by the inset of the figure. The fit results in a peak shift of $\mu_0 \Delta H_{\text{res}}(k_M = 3\text{µm}^{-1}) = 5 \pm 1$ mT. Assuming the shift is orignates from the k_M spin wave, the result corresponds to an i-DMI strength $D_S = -10$ pJ/m, which is approximately 3 times higher than observed values in literature for Pt/Co/MgO[29] and 6-8 higher than Pt/Co/AlOx[26, 80].

Since the signal now consists of a combination of the k_S and k_M peak, we use the transduction model to explain the effect of i-DMI on the mutual inductance. The calculated response for $f = 15$ GHz and an i-DMI constant of $D_S = -10$ mJ/m^2 is shown in figure 8.8b. Other input parameters are shown in table 8.2. The fact that we need a relatively high damping and anisotropy compared to the FMR measurements (8.1) might indicate that the growth of Co is altered in the fabricated strips, as mentioned in section 8.1. Nonetheless, the observed lineshape is in qualitative agreement with the experiment. The shift is reproduced, and the relative intensities of the signal are in agreement with the experiment. However, since various k-dependent processes are involved, we cannot attribute the shift solely to i-DMI. Further analysis at different frequencies reveals odd behavior of the peak shifts that cannot be explained by i-DMI

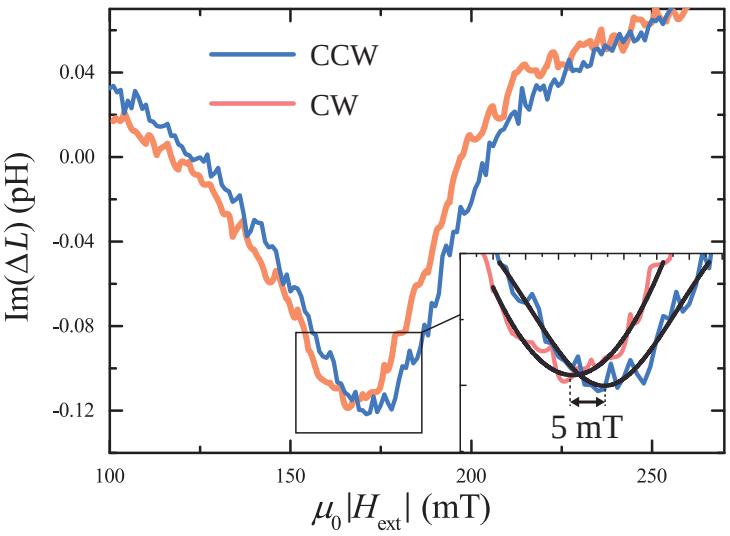

(a)

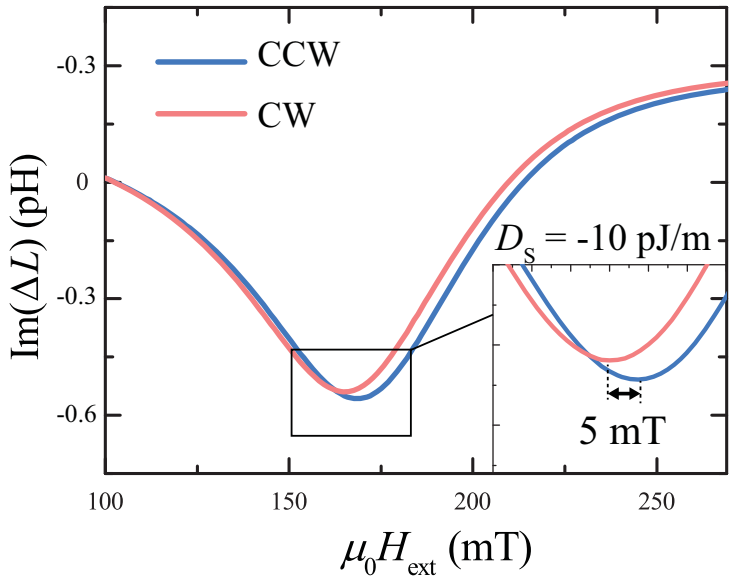

(b)

Figure 8.8: (a) Measured response in a Pt/Co/MgO stack for $\pm k$ spin waves at $f = 15$ GHz for an antenna with $k_M = 3\ \mu\text{m}^{-1}$. Inset shows Lorentzian peak fit. (b) The predicted lineshape by the transduction model for $D_S = -10$ pJ/m and an antenna distance $d = 12.4\ \mu$m. Other parameters are shown in table 8.2.

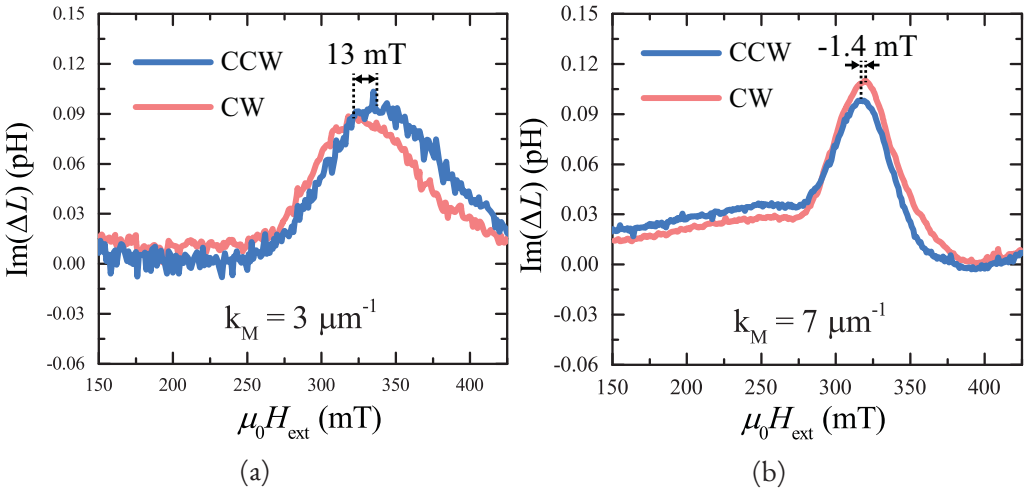

Figure 8.9: Measured response of Pt/Co/MgO stack for CW and CCW spin waves at $f = 20$ GHz for an antenna with (a) $k_M = 3$ µm^{-1} and (b) $k_M = 7$ µm^{-1}. Peak values are obtained with local Lorenzian fit (not shown in figure).

alone. Firstly, as shown in figure 8.9a, the peak shift for $k_M = 3$ µm^{-1} strongly increases with increasing applied frequency, up to 13 ± 3 mT for $f = 20$ GHz. While a small increase is expected as a function of f according to figure 6.5, a shift of 13 mT cannot be explained by i-DMI alone. This peculiar behavior is further complicated by the fact that for measurements at higher wave numbers the peak shift is significantly decreased, and even changes sign. An example of this discrepancy is shown in figure 8.9. An antenna with $k_M = 7$ µm^{-1} with $f = 20$ GHz is used for this measurement. Here we see that the CCW spin wave (blue line) has the lowest resonance field, similar to the MgO/Co/Pt stack. Unfortunately, due to the limited amount of samples we were not able to verify whether the odd k-dependence and frequency dependence of the peak shift can be reproduced. With the physical mechanisms mentioned in this chapter, we cannot explain both the frequency dependence and the k-dependence of the observed signals. Collecting a larger data set on different sample stacks could shed light on the dominant physical mechanism driving the peak shift.

Finally, we will discuss several options to measure the i-DMI values more accurately. Firstly, we can decrease the thickness of the magnetic layer, which increases the contribution of the i-DMI and causes a larger peak shift. However, decreasing the thickness also causes a broader linewidth in the presence of spin pumping and two-magnon scattering. Also, the difference in resonance fields for both spin waves $\mu_0 H_{\text{res}}(k_M) - \mu_0 H_{\text{res}}(k_S)$ becomes much smaller for thinner layers (~ 60 mT for $t_{\text{Co}} = 20$ nm versus 30 mT for $t_{\text{Co}} = 10$ nm for an antenna with $k_M = 7$ µm^{-1}). Both effects cause the resonance peaks to overlap, distorting the resonance fields and complicating the analysis.

Secondly, measuring higher k values can also increase the peak shift. Creating smaller

antennas requires further optimization of the EBL parameters and has the additional disadvantage of having to take more averages due to a decreased signal-to-noise ratio. Nonetheless, it increases the resonance peak distance for k_S and k_M spin waves, since their Fourier peaks are further apart for smaller antennas. This can greatly simplify the analysis of the signals.

In conclusion, we can state that we are able to fabricate and measure propagating spin waves using all-electrical spin wave spectroscopy. We have observed a k-dependent asymmetry in Pt/Co/MgO and MgO/Co/Pt trilayers. The intensity of high k spin waves is found to be strongly affected by the propagation direction. This can possibly be explained by the asymmetric excitation of spin waves with opposite chirality. Besides an asymmetry in amplitude, a peak shift was also observed for counter-propagating waves. However, the frequency and k-dependence of the shift could not be explained using only i-DMI. Also, the large overlap of the resonance peaks of different excited spin waves complicated the analysis of the observed signal. Therefore, no conclusive result about the magnitude of the i-DMI can be given. Only for specific cases, the transduction model is able to reproduce the observed peak shift with i-DMI. More systematic investigation on different stacks for the peak shift as a function of k can improve our understanding of the physical mechanisms at work.

Chapter 9

Conclusion and outlook

In part 1 of this thesis, a new one-port VNA-FMR setup was developed that allows for both frequency and field-swept FMR. After careful testing, the setup was then used to study interface anisotropy and spin pumping at Co/Pt interfaces. The experimental data agreed well with literature and other methods of extracting anisotropy like anomalous hall effect magnetometry. The results of the FMR experiments were used to understand the asymmetric spin wave propagation of Co/Pt multilayers.

For part 2 of this thesis, the setup was altered to allow for two port VNA measurements to investigate the asymmetric propagation of magnetostatic surface spin waves with opposite chirality. A nano-structured periodic coplanar waveguide was used to excite and detect spin waves with a well-defined wavelength. One long wavelength and one short wavelength spin wave could be distinguished in our samples, which can be explained using the analytical model developed by Vlaminck and Bailleul [69]. Good agreement was found between the model and observed lineshapes. However, the input parameters for the model required a strongly increased damping and anisotropy field compared to full sheet FMR measurements of the same magnetic stacks. This might indicate that our fabrication method of the magnetic strips alters the properties of these stacks. We were also able to measure asymmetry between spin waves with opposite chirality. Moreover, it turns out that the asymmetry is more pronounced for higher wavenumbers, as is also expected for i-DMI and other localization induced asymmetries. However, the predicted change in amplitude and the dependence of the peak shift on the spin wave wave number k did not match our experiments.

One of the complications when interpreting the observed signal is the large linewidth of the resonance curves. We believe the large linewidth most likely originates from either increased spin wave scattering or from contamination of the substrate due to the fabrication method. The latter can be investigated by cleaning the substrate after EBL exposure. However, for MgO/Co/Pt stack samples, having a relatively low damping and high k_M, we were able to distinguish between the two excited waves at low applied frequencies $f \leq 15$ GHz. These samples unambiguously showed us that

low wavenumber waves exhibit a smaller asymmetry in spin wave intensity than high wavenumber spin waves, as is expected for localization dependent processes and i-DMI. For the reverse stack, Pt/Co/MgO, a large peak shift was visible for oppositely propagating waves. However, the experimental data could not give conclusive results about the magnitude or sign of the i-DMI in these stacks due to the aforementioned linewidth related issues.

The second complication that arises is that even when we can distinguish between two spin waves, the underlying mechanism behind the asymmetry is difficult to describe unambiguously, mostly because there are multiple phenomena contributing to the asymmetry. Like i-DMI, localization of spin waves on a surface is also k-dependent and also linked to the chirality of the spin wave. For example, increased anisotropy for spin waves localized near the Co/Pt interface would induce a similar asymmetry in the observed peak shift. However, in future research the thickness t_{FM} of the magnetic layer could be varied, such that interface effects can be distinguished from interface localization effects. Interface effects like i-DMI become more pronounced for thinner layers, while for thinner layers there is less asymmetry due to interface localization.

Once the problems related to the large linewidth and discrepancies between theory and experiment can be explained, the setup opens novel paths towards investigating and possibly modulating i-DMI and spin waves in general. Several variations of the spin wave measurements performed in this thesis are listed in the following sections, which can shed light on several technologically interesting physical mechanisms using all-electrical spin wave spectroscopy.

9.1 Voltage induced modulation of i-DMI

So far, i-DMI has been a purely intrinsic property of the material stack and little experimental evidence has been found for a method that modulates i-DMI by any external means. However, such a method is highly desirable, since it could enable local stabilization and manipulation of magnetic chiral textures like skyrmions. In recent years, the influence of electric fields on the magnetic properties of thin films has become an intensively studied topic[81]. For example, due to the absence of Joule heating, electric fields offer an energy efficient alternative to the use of Oersted fields or currents to manipulate the magnetization. In 2009, Maruyama *et al.* [82] has shown that interface anisotropy can be changed up to 40% by applying an electric field parallel to the normal of ultrathin Fe layers. Similar behavior might be expected for other interface related phenomena. For example by adding an extra voltage gate between antennas, as depicted in figure 9.1a, the change in D_S can be investigated as a function of the applied voltage.

Yang *et al.* [83] has performed ab-initio calculations showing that in MgO/Co/Pt stacks of three Co monolayers thick, the calculated thickness averaged DMI constant D is roughly linearly proportional to the magnitude of the applied electric field (fig-

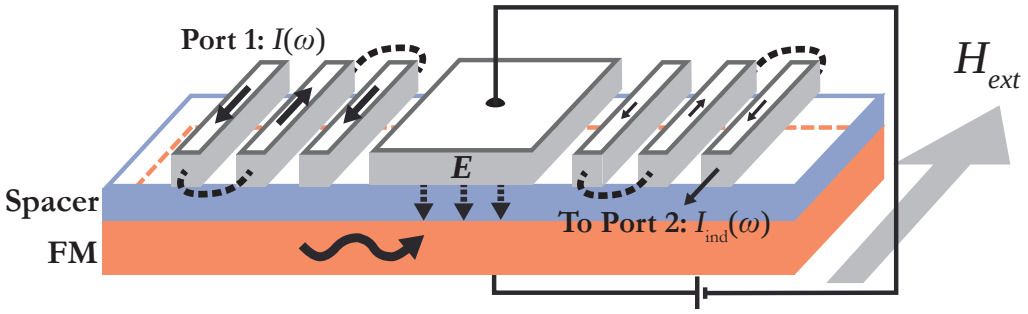

(a)

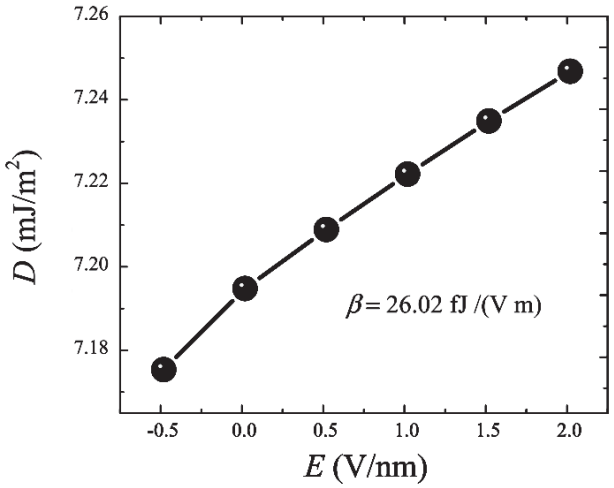

(b)

Figure 9.1: (a) Variation of the spin wave sample design allowing for measurements of the electric field induced modulation on propagating spin waves. An extra voltage gate between the antennas tunes the electric field at the ferromagnetic/spacer interface, which can locally induce a change in the (interface induced) magnetic parameters. (b) Calculated change in DMI-constant D as a function of an applied field of an MgO/Co(t_{Co})/Pt stack (t_{Co} equals three monolayers). The approximate slope $\beta = \frac{\partial D}{\partial E}$ is given in the figure. Figure adapted from Yang *et al.* [83].

ure 9.1b). The DMI constant is found to increase by approximately $\Delta D = 26$ nJ/m^2 for an applied electric field of 1 mV/nm. Nawaoka *et al.* [84] have done preliminary experimental work on electric field modulated i-DMI in Au/Fe/MgO stacks using an all electrical frequency swept two-port VNA setup. The relative change in i-DMI constant was $\Delta D \approx 40$ nJ/m^2 at an estimated electric field of 5.5 mV/nm, which is approximately the same order of magnitude as predicted by Yang *et al.* [83]. Observed peak shifts were in the range of tens of kHz, which is at least one order of magnitude smaller than the resolution of most VNA's (typically hundreds of kHz to several MHz). Therefore, signals should be accurately analyzed, for example by fitting the data to allow for the required levels of accuracy. Also, the antenna design in the experiments of Nawaoka *et al.* [84] excited a broad spectrum of wavelengths. Using the structuring tools presented in this thesis, much higher and more well defined wave vectors can be obtained, which can increase the observed peak shift by an order of magnitude.

9.2 Non-inductive spin wave detection

The antennas used in this thesis allow for both spin wave detection and excitation. This means that left and right traveling waves can be easily measured by changing the source port of the VNA. However, the relatively thick spacer layer that is required to prevent shunting limits the induced voltage. Additionally, since the detected signal is caused by induction, the amplitude of the induced current is also decreased for (I) thinner layers (required for high i-DMI), (II) stacks with low values for M_S (like YIG) or (III) samples with high wavenumber k_M (required for high peak shifts). This limits the freedom in our sample design. Other electrical detection methods based on the anomalous hall effect[87] or on the inverse spin hall effect[88] of the magnetization vector have proven to be a suitable alternative for CPW-based VNA-FMR measurements and could (partly) resolve the above-mentioned issues.

For example, detection of propagating waves can be enhanced in the presence of spin pumping and the inverse spin hall effect, which generates both an AC-current and a DC-current transverse to the precession direction. This effect is depicted in figure 9.2a [85]. The grey arrows represent the pumped spins across the ferromagnetic-normal metal interface. The oscillating spin current in the yz-plane generates an oscillating current due to the inverse spin hall effect pointing in the x-direction. The accumulation of the smaller vertical pumped spin component generates a constant current in the y-direction due to the inverse spin hall effect. This effect has been utilized by Chumak *et al.* [86] to study spin wave propagation of backward volume waves. They used a setup is depicted in figure 9.2b. A short microwave pulse excited spin waves in a YIG waveguide, while a thin Pt strip patterned on top of that waveguide acts as the detector. The YIG/Pt interface provides high spin pumping, such that the induced DC voltage in the Pt strip could be measured.

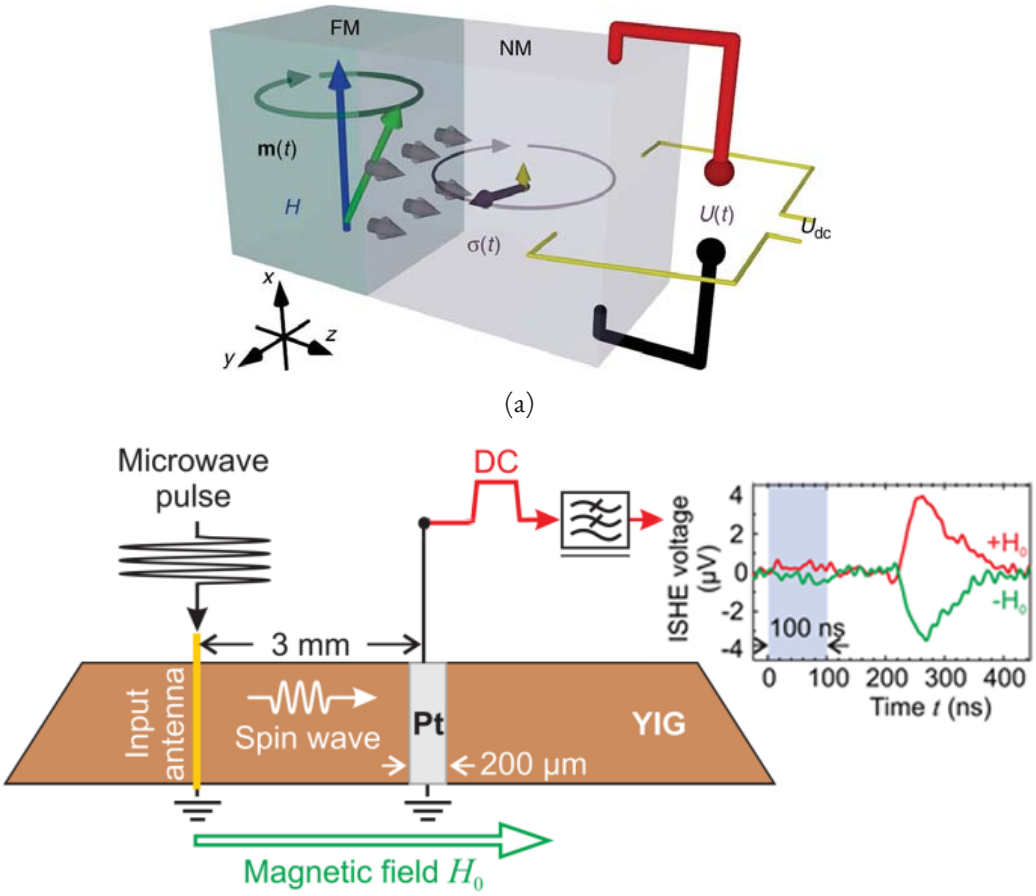

Figure 9.2: (a) A precession magnetization $\boldsymbol{m}(t)$ induces an oscillating (AC) spin current with polarization $\sigma(t)$ (in black) and a small constant (DC) spin current (in yellow) in the adjacent metal layer. Via the inverse spin hall effect (ISHE), these spin currents are converted into charge currents resulting in voltages $U(t)$ and U_{DC}. Figure obtained from Wei *et al.* [85]. (b) Spin waves are excited in a YIG film by a 100 ns microwave pulse (blue region in graph) and propagate outwards. As the spin wave arrives at the Pt strip, spin pumping and the ISHE induce a DC voltage. After applying a low-pass filter, the voltage can be measured with an oscilloscope for different field polarities (blue and green line). Figure adapted from Chumak *et al.* [86].

By slightly altering the geometry of the detector, this setup could be utilized for magnetostatic surface spin waves. The voltage difference along the propagation direction is then a measure for the DC component of the ISHE. Since spin pumping is not strongly dependent on the wavenumber of spin waves[76] or the magnetic layer thickness, the signal quality for high k_M antennas and thin films is preserved. Lastly, this detection method has the advantage of allowing modulation techniques, improving the measurement accuracy in the system.

Bibliography

[1] T. Moriya, "Anisotropic superexchange interaction and weak ferromagnetism," *Physical Review*, vol. 120, no. 1, pp. 91–98, 1960.

[2] I. Dzyaloshinskii, E. Lifshitz, and L. Pitaevskii, "General Theory of Van Der Waals'Forces," *Physics-Uspekhi*, vol. 4, no. 2, pp. 153–176, 1961.

[3] U. Rößler, A. Bogdanov, and C Pfleiderer, "Spontaneous skyrmion ground states in magnetic metals," *Nature*, vol. 442, no. 7104, pp. 797–801, 2006.

[4] S Mühlbauer, B Binz, F Jonietz, C Pfleiderer, A Rosch, A Neubauer, R Georgii, and P Böni, "Skyrmion lattice in a chiral magnet," *Science*, vol. 323, no. 5916, pp. 915–919, 2009.

[5] A. Thiaville, S. Rohart, É. Jué, V. Cros, and A. Fert, "Dynamics of dzyaloshinskii domain walls in ultrathin magnetic films," *EPL (Europhysics Letters)*, vol. 100, no. 5, p. 57 002, 2012.

[6] X. Yu, Y Onose, N Kanazawa, J. Park, J. Han, Y Matsui, N Nagaosa, and Y Tokura, "Real-space observation of a two-dimensional skyrmion crystal," *Nature*, vol. 465, no. 7300, pp. 901–904, 2010.

[7] X. Yu, N Kanazawa, Y Onose, K Kimoto, W. Zhang, S Ishiwata, Y Matsui, and Y Tokura, "Near room-temperature formation of a skyrmion crystal in thin-films of the helimagnet fege," *Nature materials*, vol. 10, no. 2, pp. 106–109, 2011.

[8] I Kézsmárki, S Bordács, P Milde, E Neuber, L. M. Eng, J. S. White, H. M. Rønnow, C. D. Dewhurst, M Mochizuki, K Yanai, H Nakamura, D Ehlers, V Tsurkan, and A Loidl, "Néel-type skyrmion lattice with confined orientation in the polar magnetic semiconductor GaV4S8.," *Nature materials*, vol. 14, no. 11, pp. 1116–22, 2015. arXiv: 1502.08049.

[9] Y. Zhang, W. Zhao, J.-O. Klein, W. Kang, D. Querlioz, Y. Zhang, D. Ravelosona, and C. Chappert, "Spintronics for low-power computing," *Design, Automation & Test in Europe Conference & Exhibition*, pp. 1–5, 2014.

[10] M. Hayashi, L. Thomas, R. Moriya, C. Rettner, and S. S. P. Parkin, "Current-Controlled Magnetic Domain-Wall Nanowire Shift Register," *Science*, vol. 320, no. 5873, pp. 209–211, 2008.

[11] K. S. Ryu, L. Thomas, S.-H. Yang, and S. S. P. Parkin, "Chiral spin torque at magnetic domain walls.," *Nature nanotechnology*, vol. 8, no. 7, pp. 527–33, 2013.

[12] K.-S. Ryu, S.-H. Yang, L. Thomas, and S. S. P. Parkin, "Chiral spin torque arising from proximity-induced magnetization.," *Nature communications*, vol. 5, no. May, p. 3910, 2014.

[13] A. Fert, V. Cros, and J. Sampaio, "Skyrmions on the track," *Nature nanotechnology*, vol. 8, no. 3, pp. 152–156, 2013.

[14] R. Lavrijsen, D. M. F. Hartmann, A. Van Den Brink, Y. Yin, B. Barcones, R. A. Duine, M. A. Verheijen, H. J. M. Swagten, and B. Koopmans, "Asymmetric magnetic bubble expansion under in-plane field in Pt/Co/Pt: Effect of interface engineering," *Physical Review B - Condensed Matter and Materials Physics*, vol. 91, no. 10, pp. 1–8, 2015. arXiv: arXiv:1503.08999v1.

[15] J. Cho, N.-H. Kim, S. Lee, J.-S. Kim, R. Lavrijsen, A. Solignac, Y. Yin, D.-S. Han, N. J. van Hoof, H. J. Swagten, *et al.*, "Thickness dependence of the interfacial dzyaloshinskii-moriya interaction in inversion symmetry broken systems," *Nature communications*, vol. 6, 2015.

[16] J. M. Owens, J. H. Collins, and R. L. Carter, "System applications of magnetostatic wave devices," *Circuits, Systems, and Signal Processing*, vol. 4, no. 1-2, pp. 317–334, 1985.

[17] A. D. Karenowska, A. V. Chumak, A. A. Serga, and B. Hillebrands, "Magnon spintronics," *Handbook of Spintronics*, vol. 11, no. June, pp. 1505–1549, 2015.

[18] V. Vlaminck and M. Bailleul, "Current-Induced Spin-Wave Doppler Shift," *Science*, vol. 322, no. 5900, pp. 410–413, 2008.

[19] Y. Tserkovnyak, A. Brataas, and G. E. W. Bauer, "Spin pumping and magnetization dynamics in metallic multilayers," *Phys. Rev. B*, p. 10, 2002. arXiv: 0208091 [cond-mat].

[20] I. Zutić and H. Dery, "Spintronics: Taming spin currents.," *Nature materials*, vol. 10, no. 9, pp. 647–648, 2011.

[21] O. Mosendz, J. E. Pearson, F. Y. Fradin, G. E. W. Bauer, S. D. Bader, and A. Hoffmann, "Quantifying spin hall angles from spin pumping: Experiments and theory," *Physical Review Letters*, vol. 104, no. 4, pp. 1–4, 2010. arXiv: 0911.2725.

[22] W Schilz, "Spin-wave propagation in epitaxial YIG films," *Philips Res. Repts*, vol. 28, no. c, pp. 50–65, 1973.

[23] M. Bailleul, D. Olligs, C. Fermon, and S. O. Demokritov, "Spin waves propagation and confinement in conducting films at the micrometer scale," *Europhysics Letters (EPL)*, vol. 56, no. 5, pp. 741–747, 2001.

[24] J. H. Moon, S. M. Seo, K. J. Lee, K. W. Kim, J. Ryu, H. W. Lee, R. D. McMichael, and M. D. Stiles, "Spin-wave propagation in the presence of interfacial Dzyaloshinskii-Moriya interaction," *Physical Review B - Condensed Matter and Materials Physics*, vol. 88, no. 18, pp. 1–7, 2013. arXiv: 1308.3341.

[25] A. K. Chaurasiya, C. Banerjee, S. Pan, S. Sahoo, S. Choudhury, J. Sinha, and A. Barman, "Direct observation of interfacial Dzyaloshinskii-Moriya interaction from asymmetric spin-wave propagation in W/CoFeB/SiO2 heterostructures down to sub-nanometer CoFeB thickness," *Scientific Reports*, vol. 6, no. June, p. 32 592, 2016.

[26] M. Belmeguenai, J. P. Adam, Y. Roussigné, S. Eimer, T. Devolder, J. V. Kim, S. M. Cherif, A. Stashkevich, and A. Thiaville, "Interfacial Dzyaloshinskii-Moriya interaction in perpendicularly magnetized Pt/Co/AlOx ultrathin films measured by Brillouin light spectroscopy," *Physical Review B - Condensed Matter and Materials Physics*, vol. 91, no. 18, pp. 1–4, 2015. arXiv: 1503.0372.

[27] J. M. Lee, C. Jang, B.-C. Min, S.-W. Lee, K.-J. Lee, and J. Chang, "All-electrical measurement of interfacial dzyaloshinskii-moriya interaction using collective spin-wave dynamics," *Nano letters*, 2015.

[28] O. Gladii, M. Haidar, Y. Henry, M. Kostylev, and M. Bailleul, "Frequency nonreciprocity of surface spin wave in permalloy thin films," *Physical Review B - Condensed Matter and Materials Physics*, vol. 93, no. 5, pp. 1–5, 2016. arXiv: arXiv:1511.09351v1.

[29] J. M. Lee, C. Jang, B. C. Min, S. W. Lee, K. J. Lee, and J. Chang, "All-Electrical Measurement of Interfacial Dzyaloshinskii-Moriya Interaction Using Collective Spin-Wave Dynamics," *Nano Letters*, vol. 16, no. 1, pp. 62–67, 2016.

[30] J. H. Kwon, J. Yoon, P. Deorani, J. M. Lee, J. Sinha, K.-J. Lee, M. Hayashi, and H. Yang, "Giant nonreciprocal emission of spin waves in Ta/Py bilayers," *Science Advances*, vol. 2, no. 7, e1501892–e1501892, 2016.

[31] D. D. Stancil and A. Prabhakar, *Spin Waves*, i. 2009, pp. 1–13.

[32] C. Road, "Orbital magnetic moments," vol. 49, no. 18, pp. 888–896, 1994.

[33] I. E. Dzyaloshinskii, E. Lifshitz, and L. P. Pitaevskii, "General theory of van der waals'forces," *Physics-Uspekhi*, vol. 4, no. 2, pp. 153–176, 1961.

[34] T. Moriya, "Anisotropic superexchange interaction and weak ferromagnetism," *Physical Review*, vol. 120, no. 1, p. 91, 1960.

[35] H. T. Nembach, J. M. Shaw, M. Weiler, E. Jué, and T. J. Silva, "Linear relation between Heisenberg exchange and interfacial Dzyaloshinskii–Moriya interaction in metal films," *Nature Physics*, vol. 11, no. 10, pp. 825–829, 2015. arXiv: 1410.6243.

[36] A. N. Bogdanov, U. K. Roessler, M. Wolf, and K. H. Muller, "Magnetic structures and reorientation transitions in noncentrosymmetric uniaxial antiferromagnets," *Phys. Rev. B*, vol. 66, no. 2, p. 214 410, 2002. arXiv: 0206291.

[37] A. C. Sparavigna, "Distortional Lifshitz Vectors and Helicity in Nematic Free Energy Density," vol. 2, no. July, 2013.

[38] B. Hillebrands and K. Ounadjela, *Spin Dynamics in confined magnetic structures I*. 2002, vol. 34, p. 340.

[39] B. Heinrich, D. Fraitova, and V. Kamberski, "The Influence of s-d Exchange on Relaxation of Magnons in Metals," *Physica Status Solidi (B)*, vol. 23, no. 2, pp. 501–507, 1967.

[40] G. Woltersdorf, "Spin-Pumping and Two-Magnon Scattering in Magnetic Multilayers," PhD thesis, 2004.

[41] M. Sparks, R. Loudon, and C. Kittel, "Ferromagnetic relaxation. I. Theory of the relaxation of the uniform precession and the degenerate spectrum in insulators at low temperatures," *Physical Review*, vol. 122, no. 3, pp. 791–803, 1961.

[42] Y. Tserkovnyak, A. Brataas, and G. E. W. Bauer, "Enhanced gilbert damping in thin ferromagnetic films.," *Physical review letters*, vol. 88, no. 11, p. 117 601, 2002. arXiv: 0110247 [cond-mat].

[43] G. Winkler, A. Kobs, A. Chuvilin, D. Lott, A. Schreyer, and H. P. Oepen, "On the variation of magnetic anisotropy in Co/Pt(111) on silicon oxide," *Journal of Applied Physics*, vol. 117, no. 10, 2015.

[44] S. S. Kalarickal, P. Krivosik, M. Wu, C. E. Patton, M. L. Schneider, P. Kabos, T. J. Silva, and J. P. Nibarger, "Ferromagnetic resonance linewidth in metallic thin films: Comparison of measurement methods," *Journal of Applied Physics*, vol. 99, no. 9, 2006.

[45] C. Bilzer, T. Devolder, P. Crozat, and C. Chappert, "Open-circuit one-port network analyzer ferromagnetic resonance," *IEEE Transactions on Magnetics*, vol. 44, no. 11 PART 2, pp. 3265–3268, 2008.

[46] T. C. Edwards and M. B. Steer, *Foundations of interconnect and microstrip design: Third edition*. 2013, pp. 1–512.

[47] C. Bilzer, T. Devolder, P. Crozat, C. Chappert, S. Cardoso, and P. P. Freitas, "Vector network analyzer ferromagnetic resonance of thin films on coplanar waveguides: Comparison of different evaluation methods," *Journal of Applied Physics*, vol. 101, no. 7, 2007.

[48] J. M. L. Beaujour, W. Chen, A. D. Kent, and J. Z. Sun, "Ferromagnetic resonance study of polycrystalline cobalt ultrathin films," *Journal of Applied Physics*, vol. 99, no. 8, pp. 48–50, 2006. arXiv: 0509036 [cond-mat].

[49] C Tannous and J Gieraltowski, "The Stoner–Wohlfarth model of ferromagnetism," *European Journal of Physics*, vol. 29, no. 3, pp. 475–487, 2008. arXiv: 0607117 [physics].

[50] S. Emori and G. S. D. Beach, "Optimization of out-of-plane magnetized Co / Pt multilayers with resistive buffer layers," vol. 033919, pp. 1–5, 2011.

[51] C. J. Lin, G. L. Gorman, C. H. Lee, R. F. C. Farrow, E. E. Marinero, H. V. Do, H. Notarys, and C. J. Chien, "Magnetic and structural properties of Co/Pt multilayers," *Journal of Magnetism and Magnetic Materials*, vol. 93, no. C, pp. 194–206, 1991.

[52] U. Wiedwald, M. Spasova, M. Farle, M. Hilgendorff, and M. Giersig, "Ferromagnetic resonance of monodisperse Co particles," *Journal of Vacuum Science & Technology A: Vacuum, Surfaces, and Films*, vol. 19, no. 4, p. 1773, 2001.

[53] S. Yuan, L. Sun, H. Sang, J. Du, and S. Zhou, "Interfacial effects on magnetic relaxation in Co/Pt multilayers," *Physical Review B*, vol. 68, pp. 1–6, 2003.

[54] J Pelzl, R Meckenstock, D Spoddig, F Schreiber, J Pflaum, and Z Frait, "Spin–orbit-coupling effects on g-value and damping factor of the ferromagnetic resonance in Co and Fe films," *Journal of Physics: Condensed Matter*, vol. 15, no. 5, S451–S463, 2003.

[55] M. T. Johnson, P. J. H. Bloemen, F. J.a. D. Broeder, and J. J. D. Vries, "Magnetic anisotropy in metallic multilayers," *Reports on Progress in Physics*, vol. 59, no. 11, pp. 1409–1458, 1999.

[56] N.-h. Kim, J. Jung, J. Cho, D.-s. Han, Y. Yin, H. J. M. Swagten, and C.-y. You, "The interfacial Dzyalonshinskii-Moriya interaction , the surface anisotropy energy , and the spin pumping at the spin-orbit coupled Ir / Co interface," *Applied Physics Letters*, vol. 142406, 2016. arXiv: 1601.02210.

[57] M Bersweiler, K Dumesnil, D Lacour, and M Hehn, "Impact of buffer layer and Pt thickness on the interface structure and magnetic properties in (Co/Pt) multilayers," *Journal of Physics: Condensed Matter*, vol. 28, no. 33, p. 336 005, 2016.

[58] H. Yang, A. Thiaville, S. Rohart, A. Fert, and M. Chshiev, "Anatomy of Dzyaloshinskii-Moriya Interaction at Co / Pt Interfaces," *Physical Review Letters*, vol. 115, no. 26, p. 267 210, 2015. arXiv: 1501.05511.

[59] M. Tokaç, S. A. Bunyaev, G. N. Kakazei, D. S. Schmool, D. Atkinson, and A. T. Hindmarch, "Interfacial Structure Dependent Spin Mixing Conductance in Cobalt Thin Films," *Physical Review Letters*, vol. 115, no. 5, 2015.

[60] J. S. Yang and C. R. Chang, "The Statistical Roughness and Magnetic Surface Anisotropy," *IEEE Transactions on Magnetics*, vol. 31, no. 3, pp. 1825–1828, 1995.

[61] M. T. Johnson, P. J. H. Bloemen, F. J.a. D. Broeder, and J. J. D. Vries, "Magnetic anisotropy in metallic multilayers," *Reports on Progress in Physics*, vol. 59, no. 11, pp. 1409–1458, 1999.

[62] W. Zhang, W. Han, X. Jiang, S.-H. Yang, and S. S. P. Parkin, "Role of transparency of platinum–ferromagnet interfaces in determining the intrinsic magnitude of the spin Hall effect," *Nature Physics*, vol. 11, no. 6, pp. 496–502, 2015.

[63] J. C. Rojas-Sánchez, N. Reyren, P. Laczkowski, W. Savero, J. P. Attané, C. Deranlot, M. Jamet, J. M. George, L. Vila, and H. Jaffrès, "Spin pumping and inverse spin hall effect in platinum: The essential role of spin-memory loss at metallic interfaces," *Physical Review Letters*, vol. 112, no. 10, pp. 1–5, 2014. arXiv: arXiv:1312.2717v1.

[64] B. Buford, P. Dhagat, and A. Jander, "A technique for error estimation of linewidth and damping parameters extracted from ferromagnetic resonance measurements," *Journal of Applied Physics*, vol. 117, no. 17, pp. 17–21, 2015.

[65] S. Sievers, J. Kurda, N. Liebing, F. Hohls, and H. W. Schumacher, "Microwave Interferometry for High Sensitivity VNA-FMR Measurements," *IEEE Transactions on Magnetics*, vol. 9464, no. c, pp. 1–1, 2016.

[66] R. Cheng, M. W. Daniels, J.-g. Zhu, and D. Xiao, "Antiferromagnetic Spin Wave Field-Effect Transistor," *arXiv preprint arXiv:1509.05295*, no. April, pp. 1–6, 2016. arXiv: arXiv:1509.05295v2.

[67] R. D. Gomez, M. C. Shih, R. M. H. New, R. F. W. Pease, and R. L. White, "Switching characteristics of submicron cobalt islands," *Journal of Applied Physics*, vol. 80, no. 1, pp. 342–346, 1996.

[68] K. Di, V. L. Zhang, H. S. Lim, S. C. Ng, and M. H. Kuok, "Direct Observation of the Dzyaloshinskii-Moriya Interaction in a Pt / Co / Ni Film," *Phys. Rev. Lett*, vol. 114, p. 047 201, 2015. arXiv: 1409.8570.

[69] V. Vlaminck and M. Bailleul, "Spin-wave transduction at the submicrometer scale: Experiment and modeling," *Physical Review B - Condensed Matter and Materials Physics*, vol. 81, no. 1, pp. 1–13, 2010.

[70] P. R. Emtage, "Interaction of magnetostatic waves with a current," *Journal of Applied Physics*, vol. 49, no. 8, pp. 4475–4484, 1978.

[71] M. Gesley, "Thermal-field-emission electron optics for nanolithography," *Journal of Applied Physics*, vol. 65, no. 3, pp. 914–926, 1989.

[72] M. a. McCord and M. J. Rooks, "SPIE Handbook of Micromachining and Microfabrication Volume 1," *SPIE Handbook of Microlithography, Micromachining and Microfabrication*, vol. 1, 2000.

[73] David M. Pozar, *Microwave Engineering Fourth Edition*. 2012, p. 756.

[74] S. M. Rezende, A. Azevedo, M. A. Lucena, and F. M. de Aguiar, "Anomalous spin-wave damping in exchange-biased films," *Physical Review B*, vol. 63, no. 21, p. 214 418, 2001.

[75] T. Brächer, P. Pirro, O. Boulle, and G. Gaudin, "Creation of uni-directional spin-wave emitters by utilizing interfacial Dzyaloshinskii-Moriya interaction," *arXiv*, p. 1611.07841, 2016. arXiv: 1611.07841.

[76] C. W. Sandweg, Y. Kajiwara, A. V. Chumak, A. A. Serga, V. I. Vasyuchka, M. B. Jungfleisch, E. Saitoh, and B. Hillebrands, "Spin pumping by parametrically excited exchange magnons," *Physical Review Letters*, vol. 106, no. 21, pp. 1–4, 2011. arXiv: 1103.2229.

[77] S. Emori, U. Bauer, S.-M. Ahn, E. Martinez, and G. S. D. Beach, "Current-driven dynamics of chiral ferromagnetic domain walls.," *Nature materials*, vol. 12, no. 7, pp. 611–6, 2013. arXiv: 1302.2257.

[78] K. Sekiguchi, K. Yamada, S. M. Seo, K. J. Lee, D. Chiba, K. Kobayashi, and T. Ono, "Nonreciprocal emission of spin-wave packet in FeNi film," *Applied Physics Letters*, vol. 97, no. 2, pp. 1–4, 2010.

[79] S. Rao, J. Yoon, J. Rhensius, C. S. Bhatia, and H. Yang, "Spin wave non-reciprocity and beating in permalloy by the time-resolved magneto-optical Kerr effect," *Journal of Physics D: Applied Physics*, vol. 47, no. 38, p. 385 002, 2014. arXiv: 1410.0441.

[80] J. Cho, N.-H. Kim, S. Lee, J.-S. Kim, R. Lavrijsen, A. Solignac, Y. Yin, D.-S. Han, N. J. J. van Hoof, H. J. M. Swagten, B. Koopmans, and C.-Y. You, "Thickness dependence of the interfacial Dzyaloshinskii–Moriya interaction in inversion symmetry broken systems," *Nature Communications*, vol. 6, no. May, p. 7635, 2015.

[81] F. Matsukura, Y. Tokura, and H. Ohno, "Control of magnetism by electric fields," *Nature Nanotechnology*, vol. 10, no. 3, pp. 209–220, 2015.

[82] T Maruyama, Y Shiota, T Nozaki, K Ohta, N Toda, M Mizuguchi, a. a. Tulapurkar, T Shinjo, M Shiraishi, S Mizukami, Y Ando, and Y Suzuki, "Large voltage-induced magnetic anisotropy change in a few atomic layers of iron.," *Nature nanotechnology*, vol. 4, no. 3, pp. 158–161, 2009.

[83] H. Yang, O. Boulle, V. Cros, A. Fert, and M. Chshiev, "Controlling Dzyaloshinskii-Moriya Interaction via Chirality Dependent Layer Stacking, Insulator Capping and Electric Field," *Arxiv Preprint*, p. 1603.01847, 2016. arXiv: 1603.01847.

[84] K. Nawaoka, S. Miwa, Y. Shiota, N. Mizuochi, and Y. Suzuki, "Voltage induction of interfacial Dzyaloshinskii-Moriya interaction in Au/Fe/MgO artificial multilayer," *Applied Physics Express*, vol. 8, no. 6, 2015.

[85] D. Wei, M. Obstbaum, M. Ribow, C. H. Back, and G. Woltersdorf, "Spin Hall voltages from a.c. and d.c. spin currents," *Nat Commun*, vol. 5, p. 3768, 2014. arXiv: 1307.2961.

[86] A. V. Chumak, A. A. Serga, M. B. Jungfleisch, R. Neb, D. A. Bozhko, V. S. Tiberkevich, and B. Hillebrands, "Direct detection of magnon spin transport by the inverse spin Hall effect," *Applied Physics Letters*, vol. 100, no. 8, pp. 1–4, 2012. arXiv: 1112.4969.

[87] N. Kikuchi, M. Furuta, S. Okamoto, O. Kitakami, and T. Shimatsu, "Quantized spin waves in single Co/Pt dots detected by anomalous Hall effect based ferromagnetic resonance," *Applied Physics Letters*, vol. 105, no. 24, pp. 1–5, 2014.

[88] K. Ando, J. Ieda, K. Sasage, S. Takahashi, S. Maekawa, and E. Saitoh, "Electric detection of spin wave resonance using inverse spin-Hall effect," *Applied Physics Letters*, vol. 94, no. 26, 2009.

[89] J Alvarez, E Lundgren, X Torrelles, H Isern, K. F. Peters, P Steadman, and S Ferrer, "Magnetization of Pt in the Co/Pt(110) system investigated with surface x-ray magnetic diffraction: Evidence for in-plane magnetic anisotropy," *Phys. Rev. B*, vol. 60, no. 14, pp. 10 193–10 198, 1999.

Appendices

Appendix A

Determining the saturation magnetization

To be able to correctly determine the interface contribution of anisotropy and spin pumping, it is important to investigate the presence of a magnetic dead layer. Not taking this into account results in extraordinarily high values for the surface anisotropy K_S and spin mixing conductance $g_{\text{eff}}^{\uparrow\downarrow}$. The magnetic dead layer can be determined by measuring the total magnetic moment of a sample as a function of the deposited layer thickness $t_{\text{dep.}}$. If a magnetic dead layer with thickness t_{dead} is present, the total magnetic moment $\mathcal{M}$ of the sample is given by

$$\mathcal{M} = M_S V = M_S \times A(t_{\text{dep.}} - t_{\text{dead}}), \tag{A.1}$$

where V is the volume of the magnetic film and A is the surface area of the magnetic sample. The magnetic moment $\mathcal{M}$ can be accurately determined using a Superconducting QUantum Interference (Device) Vibrating Sample Magnometer (SQUID-VSM). As depicted in figure A.1a, $\mathcal{M}$ is determined by saturating a magnetic sample in the positive and negative z-direction. After linear background subtraction, the difference in magnetic moment at saturation is equal to $2\mathcal{M}$. The sample area is determined by a microscope and image processing software, which can find the sample edges and obtain surface area of the sample relative to a predefined area (figure A.1b).

The procedure to extract t_{dead} is as follows. First, M_S is determined by dividing $\mathcal{M}$ by the uncorrected volume $V^* = At_{\text{dep.}}$. The product $M_S \times t_{\text{dep.}}$ $(= \mathcal{M}/A)$ is then plotted as a function of $t_{\text{dep.}}$, as shown in figure A.2. Using equation A.1, we find that from the slope we can extract the real value for M_S and from the offset on the x-axis we obtain t_{dead}. Results are summarized in table A.1.

For Pt/Co/Pt, no significant dead layer is observed. In fact, a small negative offset of -0.2 ± 0.2 nm is found. This could be related to the an induced magnetization of Pt atoms near the Co/Pt interface, as previously reported in literature[89]. However, due

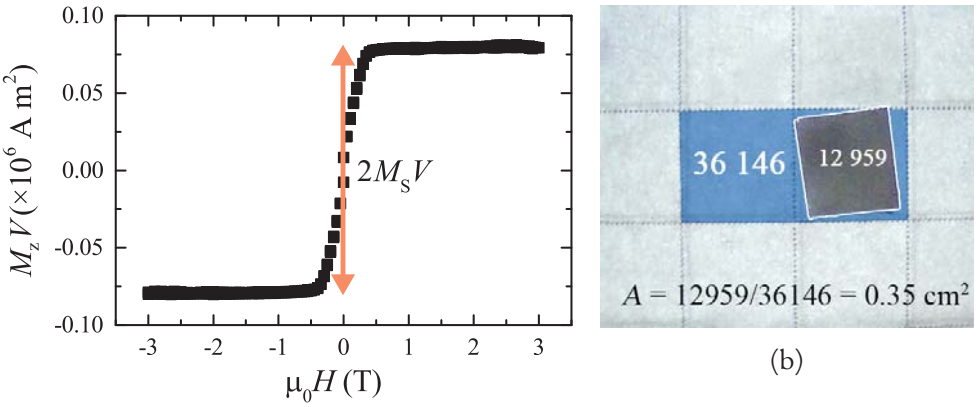

Figure A.1: (a) Positive and negative saturation of the magnetic sample gives $M_S V$. (b) The sample area is determined by finding the sample edges (white outline) and comparing the pixel count in the blue area (1 cm^2) and the sample.

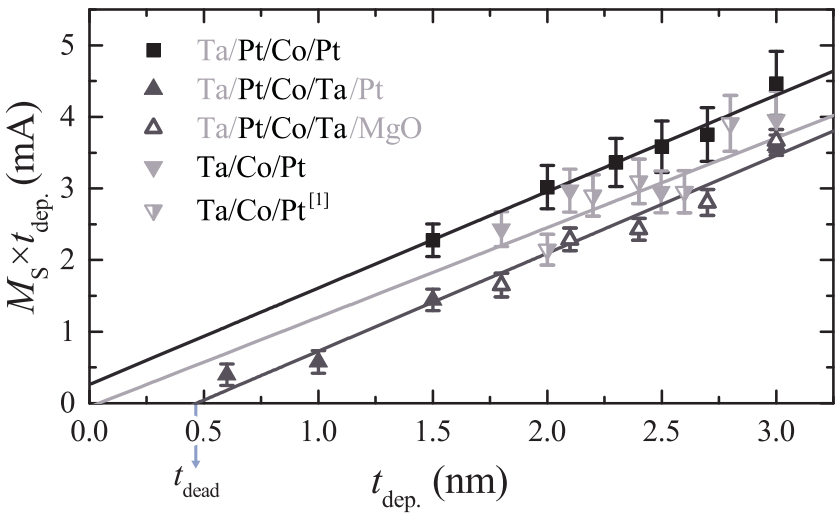

Figure A.2: Saturation magnetization M_S multiplied by the deposition thickness t_{Co} for various stacks. For Pt/Co/Ta, two different capping layers were used, which were simultaneously fitted for increased accuracy.

to its large uncertainty, we do not take this into account for the anisotropy measurements. From the slope we find that the saturation magnetization is close to that of bulk Co, indicating that the lowered bulk anisotropy observed in FMR experiments is indeed not caused by a decrease of demagnetization energy, but an extra volume anisotropy K_V.

For Pt/Co/Ta samples, a significant decrease in $\mathcal{M}$ is observed compared to the Pt/Co/Pt stack. This is the result of a large magnetic dead layer at the Co/Ta interface. To make sure that the capping layer has no influence on the dead layer, two different capping layers were used. Both for a Pt and an MgO capping layer, a similar trend is observed for both data sets. From a linear fit we find that $t_{\text{dead}} = 0.5$ nm.

For the Ta/Co/Pt samples studied in FMR measurements, the fit gives a slightly lower value for the saturation magnetization $M_S = 1.2 \cdot 10^6$ A/m. However, out of the four grown samples, only three data points could be used for this fit. The sample with $t_{\text{dep.}} = 2.1$ nm showed a significantly higher magnetic moment than for $t_{\text{dep.}} = 2.5$ nm and is therefore omitted from the fit. The magnetic dead layer is peculiarly large and negative, which brings into question the accuracy of this fit. Also, the demagnetization field for the measured value of M_S would be smaller than the in-plane anisotropy field obtained from the FMR measurements. While this is possible in the presence on an in-plane volume anisotropy, it is also likely that the fit is simply not accurate enough for the obtained value of M_S to be conclusive.

However, another batch with the same stack was grown at the start of this thesis using another sputter deposition system. Even though the films were grown under slightly different conditions, we do observe a similar trend in the two different Ta/Co/Pt batches. Fitting both sets simultaneously gives $M_S = 1.3$ and $t_{\text{dead}} = 0.05$ nm. Noteworthy is the large spread of the data points around the fitted line. One might speculate that the amorphous growth of Ta causes unpredictable Co growth textures.

Table A.1: Magnetic properties obtained by FMR measurements of the stacks studied in this chapter. [1]Two datasets with different capping layers have been fitted simultaneously. [2]Three data points were used for fitting. [3]Two batches grown in different sputter systems were used for fitting.

Stack	M_S ($\times 10^6$ A/m)	t_{dead} (nm)
Pt/Co/Pt	1.4 ± 0.1	-0.2 ± 0.2
Pt/Co/Ta[1]	1.4 ± 0.1	0.5 ± 0.1
Ta/Co/Pt[2]	1.2 ± 0.1	-0.3 ± 0.2
Ta/Co/Pt[3]	1.3 ± 0.2	0.05 ± 0.4

Appendix B

Fourier transform of the current density

To find the Fourier transform of the current density of the antenna, we first look at the spatial distribution of the current density in figure B.1. A side view of the antenna is shown at the top of the figure. We note that the Fourier transform can be split up in two parts. First, the Fourier transform of a single CPW, consisting of a signal line (width w_s) and two ground lines (width w_g) separated by a distance $d_{\text{s-g}}$ is determined. Applying the Fourier transform of a rectangular function to the signal and ground lines gives

$$\frac{\tilde{j}_{\text{CPW}}}{I} = \frac{\tilde{j}_{\text{CPW}}}{|\tilde{j}_{\text{CPW}}|w_s} = \frac{\sin(kw_S/2)}{kw_S/2} - \frac{\sin(kw_g/2)}{kw_g/2}\cos\big(kd_{\text{s-g}}\big). \tag{B.1}$$

Then, we determine the Fourier transform of the total antenna given by the sum of N of these CPW's, separated by a distance $nd_{\text{s-s}}$ from the center CPW. Here, n is an integer ranging from $-\frac{N-1}{2}$ to $\frac{N-1}{2}$ (assuming N is uneven). This results in

$$\begin{aligned}\tilde{j}_{\text{meander}} &= \sum_{n=-(N-1)/2}^{(N-1)/2} (-1)^n \tilde{j}_{\text{CPW}}(k)\exp(inkd_{\text{s-s}}) \\ &= \tilde{j}_{\text{CPW}}(k) \sum_{n=0}^{(N-1)/2} (-1)^n 2\cos(nkd_{\text{s-s}}),\end{aligned} \tag{B.2}$$

where the factor $(-1)^n$ comes from the fact that for each consecutive repetition of the CPW the direction of the current is inverted. Note that we have assumed that the current densities in the ground and signal line are equal in amplitude, which is only the case if $w_s = 2w_g$.

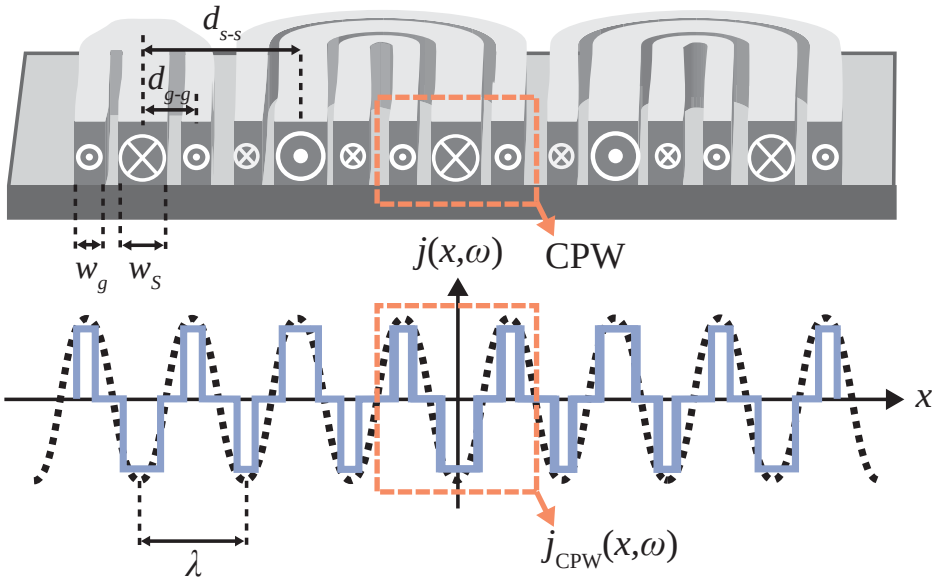

Figure B.1: For monochromatic excitation, the current density in a meander shaped antenna should approximate a sine wave with wavelength λ (dotted black line). The antenna consists of N repetitions of a single CPW structure, where the direction of the current, j_{CPW}, is reversed for each repetition.

As discussed in section 6.3, we note that for meander shaped antenna design, two separate peaks can be distinguished. The main peak with wavenumber k_M corresponds to the desired periodicity, also given by the dotted line in figure B.1. However, a second peak arises as well, with a much smaller wavenumber k_S. In principle, both spin waves can be used to extract data. However, the presence of two resonance curves can complicate the analysis if both peaks overlap. To prevent complications, the excitation should be preferably as monochromatic as possible. This can be achieved by using more repetitions of the meander, which increases the k_M Fourier peak height and decreases the linewidth Δk_M. However, the finite attenuation length of spin waves limits the maximum number of meander repetitions, since the distance between excitation and detection would simply become too large to contribute to the induced signal. Therefore, in this research we have chosen to create antennas with $N = 5$.